Electronic Theses and Dissertations, 2004-2019

2008

Inter-satellite Microwave Radiometer Calibration

Liang Hong
University of Central Florida

University of
Central Florida

STARS
Showcase of Text, Archives, Research & Scholarship

INTER-SATELLITE MICROWAVE RADIOMETER CALIBRATION

by

LIANG HONG
M.S. University of Central Florida, 2004

A dissertation submitted in partial fulfillment of the requirements
for the degree of Doctor of Philosophy
in the School of Electrical Engineering and Computer Science
in the College of Engineering and Computer Science
at the University of Central Florida
Orlando, Florida

Spring Term
2008

Major Professor: W. Linwood Jones

ABSTRACT

The removal of systematic brightness temperature (T_b) biases is necessary when producing decadal passive microwave data sets for weather and climate research. It is crucial to achieve T_b measurement consistency among all satellites in a constellation as well as to maintain sustained calibration accuracy over the lifetime of each satellite sensor. In-orbit inter-satellite radiometric calibration techniques provide a long term, group-wise solution; however, since radiometers operate at different frequencies and viewing angles, T_b normalizations are made before making intermediate comparisons of their near-simultaneous measurements. In this dissertation, a new approach is investigated to perform these normalizations from one satellite's measurements to another. It uses Taylor's series expansion around a source frequency to predict T_b of a desired frequency. The relationship between T_b's and frequencies are derived from simulations using an oceanic Radiative Transfer Model (RTM) over a wide variety of environmental conditions. The original RTM is built on oceanic radiative transfer theory. Refinements are made to the model by modifying and tuning algorithms for calculating sea surface emission, atmospheric emission and attenuations. Validations were performed with collocated WindSat measurements.

This radiometric calibration approach is applied to establish an absolute brightness temperature reference using near-simultaneous pair-wise comparisons between a non-sun synchronous radiometer and two sun-synchronous polar-orbiting radiometers: the Tropical Rain Measurement Mission (TRMM) Microwave Imager (TMI), WindSat (on Coriolis) and Advanced Microwave Scanning Radiometer (AMSR) on Advanced Earth Observing System –II (ADEOS-II), respectively. Collocated measurements between WindSat and TMI as well as between

AMSR and TMI, within selected 10 weeks in 2003 for each pair, are collected, filtered and applied in the cross calibration. AMSR is calibrated to WindSat using TMI as a transfer standard. Accuracy prediction and error source analysis are discussed along with calibration results. This inter-satellite radiometric calibration approach provides technical support for NASA's Global Precipitation Mission which relies on a constellation of cooperative satellites with a variety of microwave radiometers to make global rainfall measurements.

To my parents, Zhexi Hong and Qin Zhou, who have supported my education with endless encouragement and patience.

ACKNOWLEDGMENTS

TABLE OF CONTENTS

LIST OF FIGURES

LIST OF TABLES

LIST OF ACRONYMS/ABBREVIATIONS

ADEOS	Advanced Earth Observing Satellite
AMSR	Advanced Microwave Scanning Radiometer
CLW	Cloud Liquid Water
DMSP	Defense Meteorological Satellite Program
EIA	Earth Incidence Angle
GDAS	Global Data Assimilation System
GPM	Global Precipitation Measurement
HCB	Height of Cloud Base
HCT	Height of Cloud Top
IFOV	Instantaneous Field Of View
L2A	AMSR science data product level 2A
NASA	National Aeronautics and Space Administration
NCEP	National Centers for Environmental Prediction
NOAA	National Oceanic and Atmospheric Administration
NRL	Naval Research Laboratory
PRT	Platinum Resistance Thermometer
RTM	Radiative Transfer Model
SSM/I	Special Sensor Microwave/Imager
SST	Sea Surface Temperature
TMI	TRMM Microwave Imager
TRMM	Tropical Rainfall Measuring Mission

TTP	Top of Tropopause
WS	Wind Speed
WV	Water Vapor

CHAPTER 1 :   INTRODUCTION

According to the internet encyclopedia, Wikipedia, remote sensing is associated with *"the acquisition of information of an object or phenomenon, by the use of real-time sensing device(s) that is not in physical or intimate contact with the object (such as by way of aircraft, spacecraft, satellite, buoy, or ship)."*

Electromagnetic remote sensing is defined as the process of ascertaining certain properties of an object or physical medium from a distance by collecting and the interpretation of its spectral emission or reflection properties over a variety of wavelengths from radio frequency to beyond visible light. Satellite passive microwave remote sensing is a special application of microwave communications technologies for the purpose of collecting geophysical information about the Earth's atmosphere and surface using instruments (radiometers) onboard earth orbiting satellites. With a constellation of satellites, engineers and scientists are able to monitor Earth's environment on both short- and long-term temporal scales.

1.1   Research Motivation

Ever since the beginning of the second industrial revolution in the mid-1800's, environmentalists have become increasingly concerned over the impact of human activities on the climate of the earth. This reached the "public enlightenment stage" in the mid-1900's, when the industrial nations of the world endorsed the formation of international environmental organizations under the sanction of the United Nations and other scientific societies to address the reduction of air and water pollution caused by industrial and societal emissions and waste

products. Public concerns were heightened when earth satellite observations became available in the 1970's and 80's, which, for the first time, showed the wide-spread effects of global pollution. Within the United States, citizen concerns prompted congress to form a combined federal governmental agency task force involving environmental monitoring (NASA), climate modeling and prediction (NOAA), regulation and enforcement (EPA) and others.

In the 1980's this interagency working group for Global Climate Change empowered NASA to develop the Earth Observing System (EOS) program to provide long-term monitoring of the environment using satellite remote sensing technologies to provide carefully controlled long-term multi-decadal data sets of environmental geophysical parameters of the atmosphere, ocean, terrain, biosphere and cryosphere.

Thus, the monitoring of the Earth's climate is of utmost importance for the protection of human lives and for numerous socio-economic benefits. Today, predictions of the future states of the climate system are developed using numerical climate models, and satellite remote sensing provides the decadal geophysical parameter time series of measurements from which these simulations are derived. Satellites have the advantage of providing near-global distributions of measurements; however, the challenge remains in achieving sustained geophysical measurement accuracy over the lifetime of many different satellites/instruments in a particular data time series. The importance of providing long-term overlapping temporal observations of environmental parameters, such as air and sea surface temperature, carbon dioxide and greenhouse gasses, water vapor and cloud liquid water, precipitation, biomass, etc., cannot be over emphasized; and meteorological satellites provide the most valuable source of these remote sensing records [1].

Many microwave remote sensing instruments have been launched on different satellites to orbit the earth during the same observation period or as replacements for extended missions.

For long-term observations, which lasts from years to decades, the accuracy of the geophysical parameter measurement time series depends on the stability of the instrument measurement and the remote sensing retrieval algorithms. Thus, since the inferred geophysical parameters depend on both the changes in environmental conditions and the instrument transfer functions, it is important for remote sensing technologists to make the latter stable. Engineers and scientists continually assess solutions to minimize the instrumental error in an attempt to make the measurement more accurately reflect "true" environmental changes.

Variations in an instrument's transfer function could have many origins including calibration approaches and instrument hardware technology. There are many different techniques used in the design and manufacture of instruments depending on their application. In addition, subtle aging characteristics of instruments can cause time variable bias errors in measurements, which must be quantified to separate these instrumental effects from real changes in environmental parameters. Frequently, remote sensing instruments exceed their design lifetimes before being replaced by their successors, which are often designed with different (improved) components and technologies. Furthermore, calibration technique improvements can also contribute to discrepancies among satellite data products. Due to these many sources of measurement errors, there is a critical need to develop an inter-satellite calibration system that operates continually on-orbit. This system should take into consideration observations made by multiple instruments, at different mission phases, to produce reliable and stable calibrated geophysical measurements.

Therefore, the motivation of this dissertation research is to develop an analytic microwave radiometric cross-calibration technique for inter-calibration of dissimilar radiometer instruments. The first projected application is for the inter-radiometric calibration of cooperative

satellites within the multi-satellite Global Precipitation Measurement (GPM) constellation. The goal of GPM is to improve global rainfall estimates by using a constellation of satellites to reduce the sampling errors of rainfall in 3-hour temporal windows. In order to produce a satisfactory merged product, rainfall retrievals from each cooperative satellite must be normalized using a common "core-satellite" in non-sun-synchronous orbit.

Achieving this desired agreement on rainfall retrievals is a multi-part effort; and the first step is to assure radiometric consistency among the various sensors. A major challenge for this radiometric comparison is that satellite radiometer systems have different designs and instrument characteristics. These characteristics include frequency, bandwidth, viewing geometries (azimuth and incidence angles), calibration approaches, and antenna properties (e.g., instantaneous fields of view, polarization purity, beam efficiency, and reflector emissivity).

The essence of this dissertation is to develop a robust technique to normalize instrument characteristic differences in brightness temperature (T_b) measurements before conducting simultaneous comparisons. This technique is based upon the Taylor series approximation that is derived from theoretical ocean brightness temperatures using a calibrated radiative transfer model. Radiometric cross-calibrations were performed between two sun-synchronous polar orbiting satellites, WindSat and AMSR (Advanced Microwave Scanning Radiometer), using the TMI (TRMM Microwave Imager) on the non-sun synchronous TRMM satellite as the transfer standard. Near-simultaneous pair-wise comparisons of measurements over tropical oceans were applied in the cross-calibration of each pair, TMI with WindSat or AMSR.

1.2   <u>Dissertation Ornanization</u>

The remaining chapters of this dissertation are organized as follows:

Chapter 2 provides a brief introduction to microwave radiometry and discusses the history of satellite microwave radiometer cross-calibrations. Chapter 3 describes the satellite microwave radiometer data used in this research, specifically; simultaneous, pair-wise, collocated T_b measurements from WindSat, TMI and AMSR. Chapter 4 describes the radiometric calibration algorithm developed under this dissertation, which uses a microwave radiative transfer model (RTM) tuned to WindSat T_b measurements. Chapter 5 describes application of this RTM in: the simulation of T_b measurements of different radiometer channels, the development of T_b model functions, and the generation of the Taylor series expansion normalization for frequency and incidence angle differences for different radiometers. Chapter 6 presents the results of the inter-satellite calibration for WindSat, TMI and AMSR; and finally, chapter 7 summarizes this dissertation and presents conclusions.

.

CHAPTER 2 : MICROWAVE RADIOMETRY AND INTER-SATELLITE CALIBRATIONS

2.1 Microwave Radiometry

All matter is composed of charged particles (electrons and protons), which are in constant random motion and as a result emit non-coherent electromagnetic (EM) radiation. The total EM radiant energy emitted by a blackbody (theoretical perfect emitter) is distributed over wavelength according to Planck's radiation law.

Passive microwave remote sensing is concerned with the absolute power measurement of the natural blackbody emissions over the EM wavelength range between 30 and 0.03 cm. Because these microwave wavelengths are not susceptible to the atmospheric molecular scattering, which affects shorter optical wavelengths, microwave radiation can penetrate through most atmospheric conditions including cloud cover, haze, dust, but not necessarily rainfall. This property allows for the detection of microwave energy under almost all weather and environmental conditions. Applications of passive microwave remote sensing include the scientific fields of meteorology and climate studies, hydrology, and oceanography.

According to the Rayleigh-Jeans approximation to Planck's law, which is applicable in microwave spectral region, the emission power captured by an ideal lossless antenna with single linear polarization is [2]

$$P_{ant} = kTB, \qquad W \tag{2.1}$$

where k is the Boltzmann's constant, T is the equivalent noise temperature and B is the frequency bandwidth of the radiometer receiver.

For earth observations through a lossless antenna, it is convenient to define the apparent radiometric brightness temperature as

$$T_{ap} = \frac{P_{ant}}{kB}, \qquad K \tag{2.2}$$

Brightness temperature, T_b, is used to characterize the EM emission of the scene, and it is the equivalent physical temperature of an idealized blackbody emitter that produced the observed captured emission.

The instrument of passive remote sensing is known as a radiometer (see Appendix-A). For microwaves, the instrument takes the form of an antenna, a sensitive receiver and square-law power detector that is used to quantitatively measure the intensity of naturally emitted microwave energy captured within its antenna instantaneous field of view (IFOV). For most satellite microwave radiometers, the antenna optical beamwidth of the various channels is of order degrees; thus the spatial resolution of these instruments relatively poor (typically, tens of kilometers), thereby restricting these sensors to low-resolution imaging..

2.2   Post-Launch Calibration

Although microwave radiometer instruments under-go extensive pre-launch calibration in thermal vacuum (TV) testing facilities, it is important to verify proper radiometric performance on-orbit; and (unfortunately) proper pre-launch calibration is still not a guarantee of the absolute accuracy of on-orbit brightness temperature measurements. Historically, both pre-launch and on-orbit radiometer calibrations have been required to ensure accurate T_b measurements [3 - 14]. For example, for ground testing, the antenna main reflector and the cold sky reflector are not

included in the TV chamber due to size and other limitations. Further, the brightness temperature of the cold-load blackbody target does not correspond to on-orbit space conditions (2.73 K) because its physical temperature is limited to that of liquid nitrogen (77 K). Any non-linearity within the receiver will result in absolute calibration shifts because of the change of the cold load brightness temperature.

Once on-orbit, another source of absolute calibration uncertainty is the antenna beam efficiency effect. Even though a good characterization of the antenna pattern has been performed prior to launch, it is very difficult to properly estimate the reception of thermal radiation emitted by the various sources in space (including the satellite and the Earth) through antenna side-lobes. Finally, the reflector emissivity, which is usually negligible on the ground, may degrade in space due to aging or impacts from micrometeoroids or other debris. This can disrupt the reflective coating and cause the reflector to become lossy and have radiometric self-emissions, which were not characterized during the TV ground calibration. For all these reasons (and others), careful analysis and correction after launch is required to ensure good long-term radiometric calibrations.

Calibration surprises (problems) have been found in post-launch analyses for almost every conical-scanning microwave radiometer launched to orbit, and these issues have resulted in absolute calibrations adjustments of several Kelvin or more. Examples include, but are not limited to: unexplained high reflector emissivity and an IFOV obstruction at the end of each scan on TMI [3], unstable hot load on AMSR [4 - 6], transient sun illumination on hot load on WindSat [7]. These problems are extremely difficult to predict or prevent before launch, and post-launch calibrations are required to solve these problems while the instruments are in orbit.

Post-launch or in-orbit calibrations can be performed using comparisons to external references in different ways. Methods include comparison with measurements from similar

instruments on simultaneous observations [8, 9]; comparison with measurements from ground-based radiometers [10]; comparison with simulations over sea using geophysical condition parameters and a radiative transfer model [11]; analysis against vicarious cold reference, derived from histograms of the radiometer's coldest measurements, to detect small drifts in absolute calibration [12]; or, an indirect way, by validating retrieved products, such as, sea surface temperature [13], wind vector [14] and etc.

In this dissertation, investigations are focused on techniques of the comparisons between simultaneous measurements from similar radiometers and the transfer of radiometric calibration from a non-sun synchronous core satellite radiometer. On-orbit cross calibrations between satellite radiometers are developed for this long-term, group-wise objective; and there are several ways to achieve this. Typically, comparisons are accomplished by examining T_b measurements from different sensors that are observed within specified time and space collocation criteria. The issues of this approach include limited near-simultaneous collocations due to different satellite orbits, coincident regions that are not uniformly distributed over the orbit, and errors due to geo-location inaccuracy and viewing azimuth angle differences.

Another approach is to use the T_b measurements time series to eliminate inter-sensor differences. The idea is to subtract natural environmental variability and trends from the time series of each sensor, and the remaining deviations are averaged and binned for comparisons based on gridded products. This type of analysis is often applied in evaluating the satellite data in terms of global environmental data acquired by other sensors, output from numerical forecast models, or the historical record. This approach is a solution when direct or intermediate comparisons between difference sensor observations are not applicable. The deficiency of this

approach is the inability to accurately quantify the trend and variation due to changes in environmental parameters.

The objective of inter-satellite calibration is to quantify the incremental T_b biases between radiometers and to establish the calibration uncertainty (rms error). Cross-calibration between radiometer channels is normally performed by comparing the simultaneously observed ocean brightness temperatures; however, a portion of the T_b differences may be attributed to a number of instrument related characteristics, which are not errors in T_b calibration. These include: differences of the earth incidence angles (associated with antenna cone angle, spin-axis to spacecraft alignment, and orbit differences), misalignments of the antenna-beam IFOV's (including mismatch of antenna beamwidths), and scene differences caused by T_b inhomogeneities and anisotropies associated with azimuth angle differences. In order to achieve the desired cross-calibration precision of sub-Kelvin T_b, adjustments are required to account for systematic (instrumental) differences between sensors..

2.3   Satellite Constellation and Cross Calibration

Most of the satellite radiometers fly on either weather satellites or NASA remote sensing satellites in sun-synchronous orbits; however, there are also a limited number that fly on non-sun synchronous low-earth orbits like TRMM. The combination of AMSR, TMI and WindSat contains instruments flying on both kinds of orbits, and the analysis of calibrations between these three radiometers are quite representative and can serve as a prototype for inter-satellite calibrations among a satellite constellation (e.g., GPM). The ability to cross-calibrate microwave sensors and establish uncertainties (random errors) will contribute to improved operational

analyses and forecast; and there will result a significant positive impact to science investigations that address:

1. Analysis of current satellite-based atmospheric and oceanic environmental parameters for evidence of climatically significant variations at global and/or regional tropical scales. This will include inter-relations with other variables such as sea surface and atmospheric temperature, precipitation, surface winds, etc.;

2. Space-time properties of environmental parameter variations and their relationship to variations in the climate system; and

3. Development of new methodologies and requirements for observationally quantifying regional-global variations in relation to future missions.

2.4   Previous Cross Calibration Approaches

Post-launch, radiometric cross-calibration among different microwave satellite radiometers, have been routinely conducted either by comparing equivalent T_b's between channels from different satellites or by comparing radiometer measurements to radiative transfer model simulations or by comparing geophysical retrievals from the microwave measurements with independent remote sensing or in situ measurements. Usually radiometer instruments are not identical (i.e., do not have exactly the same channel characteristics: center frequencies, antenna IFOV's, viewing angles, etc.) nor do their satellites fly in the same orbits; so cross-calibrations can not be preformed by direct comparisons of their collocated measurements. Thus,

for this first kind of comparisons, normalization of T_b's from different channels to a common standard is a necessity.

For example, Colton and Poe [14] made cross calibrations between DMSP SSM/I's in 1999. Calibration accuracies were evaluated by comparing the average scene T_b's for a wide range of regions including Amazon Rain Forest, Arabian Desert, Greenland Ice Cap and calm and open-ocean with negligible cloud cover. Empirical statistical distribution functions for rain-free ocean pixels were constructed for the entire set of SSM/I's and formed the basis for assessing inter-sensor calibration. One advantage of this investigation was that the radiometers were identical designs and flying on similar orbits (only different ascending nodes); therefore T_b normalizations before comparisons were not required. The results of this study indicated that the calibration uncertainty ("noise floor") to which justifiably comparisons can be made between individual SSM/I sensors is approximately 0.3 K (depending on the channel); and this error is a combination of systematic sensor calibration differences and random uncertainty of the comparison methodology.

On the other hand, some cross-calibration techniques require theoretical radiative transfer modeling of the apparent T_b of the radiometer, which implies precise knowledge of the physics of contributions of surface and atmosphere geophysical parameters as well as their true instantaneous values along the antenna line-of-sight.

An example of this is the research of Chan and Bo-Cai Gao's [13], which provided a technique for alleviating temporal variances between measurements from different sensors over the same earth location. Their study involved the three-way comparison of sea surface temperature (*SST*) datasets from: infrared Moderate Resolution Imaging Spectroradiometer (MODIS); National Center for Environmental Prediction (NCEP) numerical weather model, and

microwave Tropical Rainfall Measuring Mission (TRMM) Microwave Imager (TMI). Based upon their results, significant discrepancies (0.5 K to 1 K) were found over extensive areas: the tropical Atlantic, tropical western Pacific, Bay of Bengal, Arabian Sea and the storm tracks.

2.5   Recent Cross Calibration Approaches

In our recent research, several inter-satellite calibration approaches have been investigated to perform comparisons between collocated measurements of radiometer channels, which include multi-channel regression prediction, spectral ratio transform and Taylor series expansion prediction.

2.5.1   Multi-Channel Regression Calibration

A slightly evolved version of the scheme used by Wilheit and Milman [15] provides a new approach for cross comparisons of measurements over oceans [8, 9]. Calibration is performed from one set of T_b's to another without an intermediate step of modeling using "known" geophysical parameters. The logic is that all radiative transfer models are imperfect; and in this approach, the same radiative transfer model is used in both the forward and inverse senses so that imperfections in the model will nearly cancel. The prediction algorithm uses a regression on a selected set of T_b's and nonlinear transforms of T_b's, chosen on a radiative transfer basis.

An ensemble of geophysical parameters was prepared for the input to a RTM to simulate a training set. The ensemble was chosen to exercise the retrieval over the entire expected range of the relevant parameters. Each member of the ensemble was used as input for the radiative

13

transfer model so that radiances with the viewing parameters (e.g., angle, wavelength, polarization, NEDT) of the target instrument can be computed. It is important that the instrumental noise be included in this calculation, and these are used as inputs to a linear regression analysis. Since the radiances do not vary linearly with the desired geophysical parameters, a transformation was performed to both the radiances and the desired parameters with linearizing functions chosen with knowledge of the relevant physics as

$$L = \ln(285 - Tb) \tag{2.3}$$

This function can be justified if the atmosphere is approximated as an isothermal layer at a physical temperature of 285 K. In the process of predicting brightness temperatures from other brightness temperatures, a combination of this form for the dependent variable and the linear form for the independent variables are used, as in the following equation

$$L_{Tb\_obj} = \sum_i (c_{iL} L_{Tb\_source} + c_{iT} T_{b\_source}) + C_0 \tag{2.4}$$

where T_{b_source} is the T_b of calibration source channel and L_{Tb_obj} is the transform of object channel T_b using equation 2.3.

There is generally a considerable quantity of redundancy in the observations; therefore, all the channels are not always needed, and some of the coefficients in equation 2.4 are set equal to zero. The regressions are then applied to predict the geophysical parameters, other brightness temperatures or linearized functions from the calculated radiances. The matrix and offsets from this regression are the retrieval algorithm, and the residuals of the regression serve as an approximate performance simulation for the instrument and algorithm.

As the prediction is derived from multiple channel inputs, any serious error in any source channel will be alleviated to some extend, depending on the regression coefficient for that

channel in the prediction. Since regression coefficients are unique for each cross calibration pair (e.g., WindSat & TMI), additional RTM T_b simulations and regression processes must be performed for each new cross-calibration pair (e.g., TMI & AMSR).

The calibration approach of multi-channel regression prediction is applied to WindSat, TMI and AMSR cross-calibrations in this dissertation. In Chapter 6, results are compared to those from calibrations using Taylor series expansion prediction.

2.5.2   Spectral Ratio Transform

Spectral ratio transform, based on a linear extrapolation, has been previously applied in inter-satellite calibrations to eliminate frequency and incidence angle differences in T_b comparisons [8]. The transfer function was built based on brightness temperatures of three adjacent frequency channels under selected "favorable" geophysical conditions. Prediction of calibration target channel T_{b_Target} is calculated by

$$T_{b\_Target} = T_{b\_Source1} + sr\left(T_{b\_Source2} - T_{b\_Source1}\right)$$

(2.5)

where $T_{b\_Source1}$ and $T_{b\_Source2}$ are measurements from calibration source radiometer channels, sr is defined as spectral ratio, which can be computed from radiative transfer model simulated T_b's using the following equation

$$sr = \frac{\overline{T}_{b\_Target} - \overline{T}_{b\_Source1}}{\overline{T}_{b\_Source2} - \overline{T}_{b\_Source1}}$$

(2.6)

where T_b's are simulated with given frequency and incidence angle.

2.5.3 Taylor Series Expansion Prediction

Taylor series expansion, the essence frequency and incidence angle normalization technique investigated in this dissertation, predicts T_b's at a target frequency from T_b's of an adjacent source frequency using an expansion of the T_b "model function" in a Taylor series centered at the source frequency. The relationships between T_b's and frequencies are derived from simulations using a RTM, and the corresponding incidence angle relationship are derived in a similar manner. Finally the radiometric cross-calibrations are performed by comparing the normalized T_b's with near-simultaneous collocated measurements. Our most recent research focused on the investigation of this Taylor series approach; and the description and discussion on the details, application, and performance are the major part of this dissertation to be presented in the following chapters.

CHAPTER 3 :   COLLOCATIONS BETWEEN SATELLITES

Near simultaneous observations over the same earth location are required to provide meaningful comparisons between different radiometer measurements. In order to find collocations between satellites, their orbits need to be analyzed first. For any pair of sun-synchronous satellites, since their time periods and orbit inclination angles are very similar and their local visit time is different, their paths are almost parallel. As a result, there is hardly any possible simultaneous observation over non-frozen oceans, which could happen between sun-synchronous satellites. An example of ground paths of two sun-synchronous satellites (AMSR and WindSat) is shown in Figure 3.1. The measurement swath of WindSat (1050 km) is represented in white lines and that of AMSR (1600 km) is given in green.
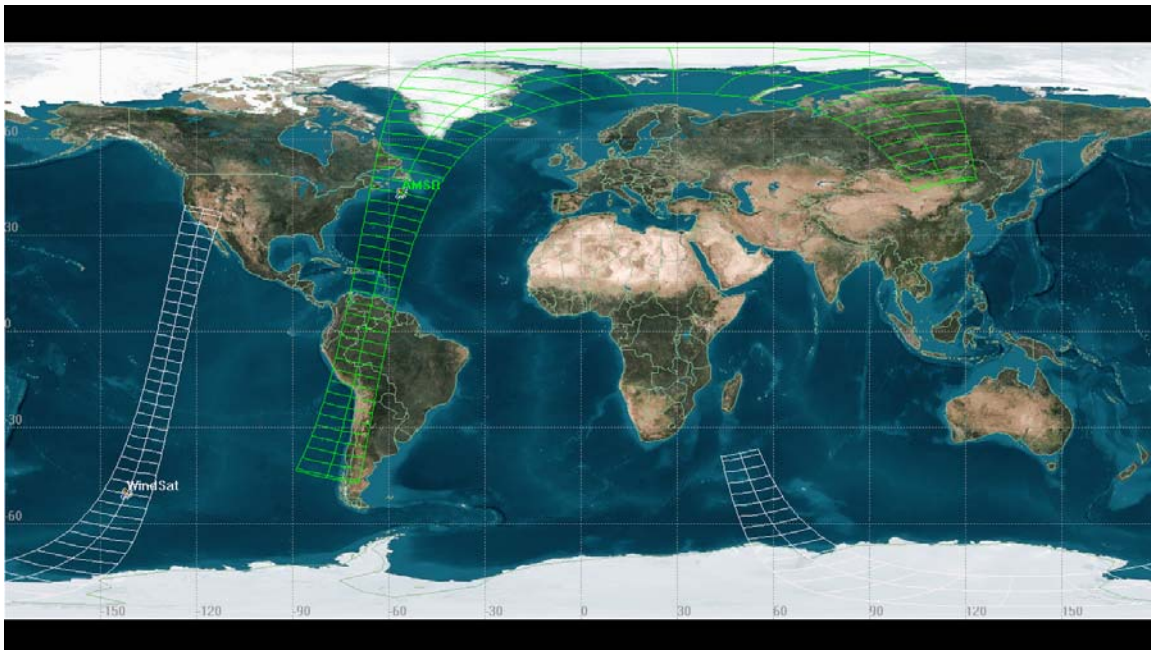
Figure 3.1: Sample of AMSR and WindSat Paths

at 14:42, on 06/01/2003

On the other hand, for non-sun-synchronous satellite orbits, it is easy to find collocations between measurement swaths of a low inclination orbit satellite (e.g. TMI) and those of a sun-synchronous satellite (e.g. WindSat) as shown in Figure 3.2. WindSat ground path is in white, and the TMI ground path is in red with a swath width of 878 km. Given reasonable spatial (25 km) and temporal tolerances (± 15 min), within which the geophysical conditions are approximately homogeneous, it is easy to find collocations between near-polar orbital and non-polar orbital radiometers.
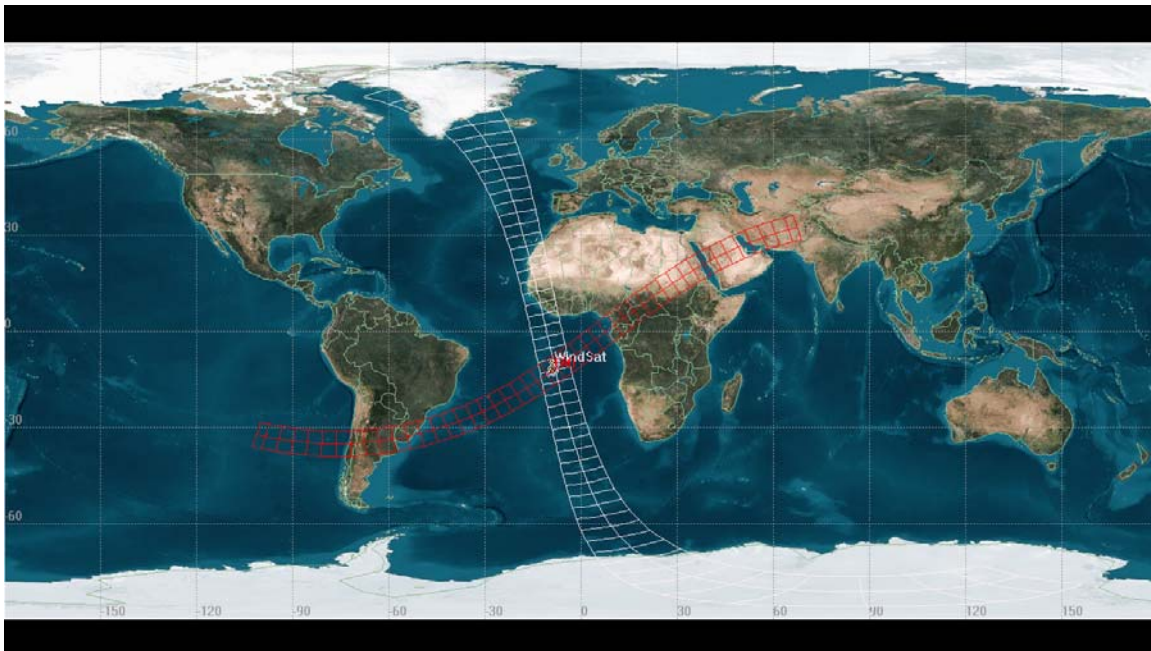
Figure 3.2: Sample of Collocations between WindSat and TMI

at 18:38:30, on 06/01/2003
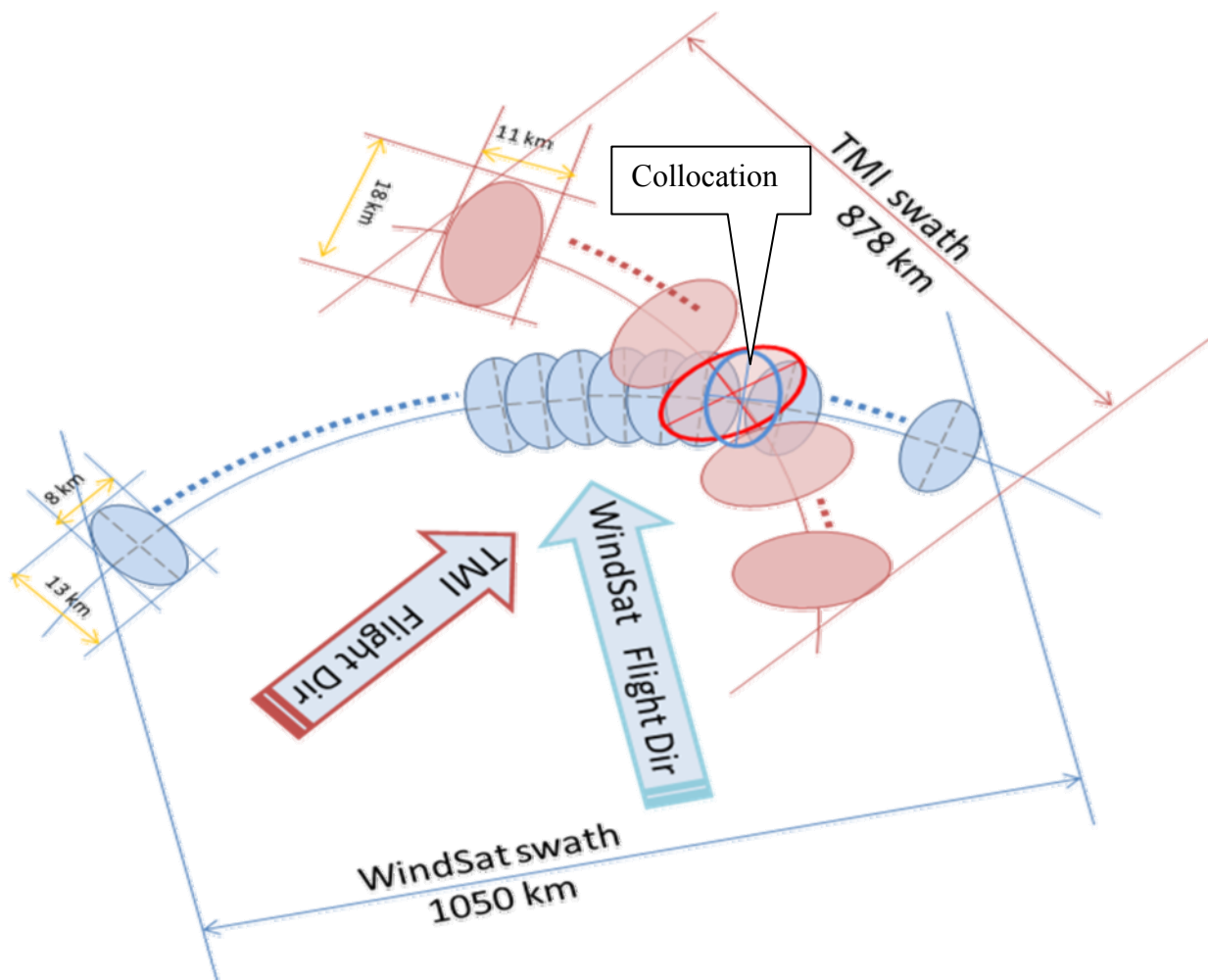
Figure 3.3: Sample of Footprints of WindSat and TMI Collocation

Figure 3.3 illustrates how WindSat and TMI measurements collocate. This example shows footprints of WindSat 37 GHz channel in blue ovals and footprints of TMI 37GHz channel in red ovals. For the WindSat 37 GHz channels, footprints are sampled at the Nyquist rate along the scan direction, while for TMI 37 GHz channels, footprints are contiguous along the scan direction. For both WindSat and TMI along track footprints, the sampling requirement is driven by the need to maintain contiguous sampling at 37 GHz. A collocated pair of measurements is found when WindSat and TMI footprints overlap each other at almost the same

time, e.g. ovals in thick lines. There is a varying difference between azimuth angles of collocated WindSat and TMI measurements from case to case. Because sea surface emissivity is anisotropic with relative surface wind direction, WindSat and TMI azimuth angle differences leads to slight ($\sim\pm$ a few K) brightness temperature differences. Fortunately, this bias in T_b comparison is significantly reduced when thousands of collocations are averaged..

3.1   Collocation Time and Coverage Selection

According to above orbit analysis, collocations will be collected between the pair of WindSat and TMI (and that of AMSR and TMI). In order to investigate different scales of temporal dependence of the cross-calibrations, weekly and monthly-collocated measurements were collected. The T_b products of each sensor, which includes geolocation information, were chosen as for finding collocations and cross-calibrations after that.

Since the ADEOS-II was operational from April to October in 2003, AMSR and TMI collocations were also selected during this time frame. Due to the high volume of data processing, not all data during this period were used to find collocations. A sampling rate of one week per month was selected to provide adequate cases for our investigation.

As discussed in Chapter 2 and Appendix-A, there is a hot-load issue in WindSat calibration during certain periods of the year; therefore, in the SDR data, a modified retrieval algorithm has been used to mitigate the effects of warm load calibrations anomalies. Some degradation of the retrieval products due to these anomalies is still present during the period from mid-April to mid-August each year [16]. To be consistent with data collected between AMSR and TMI, we gathered collocations for WindSat and TMI during that same year (2003).

With possible contamination, because of WindSat hot-load issues, collocations between WindSat and TMI were collected to cover all seasons within and outside of the abnormal period.

3.2   Collocation Algorithm

In order to avoid variable geophysical condition within the near simultaneous collocations, as well as to maintain enough cases, moderate criteria of collocation limits were selected. Temporal tolerance was set to ±15 minutes, and spatial tolerance was ±25 km. Since satellite data files are saved as one revolution per file, the algorithm to find collocations between WindSat and TMI is, for each WindSat rev,

1)   Read in WindSat SDR data, find the start and stop time of current rev

2)   Find all TMI revs that overlap with current WindSat rev, for each of the TMI rev do steps 3) and 4)

3)   Read in one TMI rev data, down sample WindSat and TMI paths into 5° by 5° boxes. For each box that contains both WindSat and TMI path, do step 4)

4)   For each WindSat pixel in this box, find closest located TMI pixel, if the time difference between these two pixels is within temporal tolerance and the distance between them is within the spatial tolerance, attach the TMI measurement information (including T_b's of all channels, time, latitude, longitude and other supplemental information from the TMI data) to this WindSat measurement.

The data of collocations from two satellites are then filtered to remove measurements over unwanted land surfaces. Rain-free tropical ocean scenes were selected for the collocations in

order to remove large T_b uncertainties associated with rain and to minimize the effects of horizontal inhomogeneities.

The collocated measurements can be examined in a variety of ways. At the simplest level, the nearest neighbor collocations between any two satellites can simply be regressed against one-another. The data could also be averaged across particularly uniform areas before comparison. By analyzing histograms and statistical moments for areas with size of 1° by 1° in latitude and longitude, the latter was chosen to reduce standard deviations of T_b's in each channel.

3.3   Collocated Data Sets

Matched-up measurements of AMSR and TMI were collected during the month of June, 2003 and 1 week's data in each of the other months from April, 2003 to October, 2003. The T_b data are from the Jet Propulsion Lab's SeaWinds AMSR L2A overlay product and the TMI 1B11 brightness temperature products respectively. Major geophysical parameters, such as sea surface temperature, wind speed, water vapor and cloud liquid water, are selected from AMSR products. Although this data collection method may not be ideal to find the most accurate environmental conditions, it is proven to be fast and the geophysical parameters are already registered with brightness temperature measurements. In the process of finding the collocation cases, for each of the AMSR measurements, the collocated TMI is selected to be the geometrically closest measurement which takes place within ±15 minutes. No collocation is recorded unless there is a TMI measurement within 25 km of the AMSR measurement.

The T_b's from low frequency channels less than 50 GHz are read from AMSR and TMI data records and averaged over 1° by 1° boxes. By examining the mean and standard deviation of

all the observed brightness temperatures for each channel, we set upper bound for T_b's in each channel to screen outliers in each 1° by 1° box, see Tables 3.1 and 3.2 [17]. The box is discarded if: it contains a rainy pixel, the standard deviation of T_b's in vertical polarization is greater than 2K or the standard deviation of T_b's in horizontal polarization is greater than 3K [17]. The box is also omitted if there is only one collocated measurement in it. Thus, data that are contaminated by land or rain in the field of view are eliminated. Furthermore, these criteria eliminate T_b outliers that have possible instrument problems.

Table 3.1: Upper Bound for AMSR T_b's Over Tropical Ocean

Channel	6.925H	6.925V	10.65H	10.65V	18.7H	18.7V	23.8H	23.8V	37H	37V
T_b (K)	100	180	110	190	175	230	250	265	210	250

Table 3.2: Upper Bound for TMI T_b's Over Tropical Ocean

Channel	10.65H	10.65V	19.35H	19.35V	21.3V	37H	37V
T_b (K)	115	185	200	230	260	210	240

Table 3.3: Upper Bound for WindSat T_b's Over Tropical Ocean

Channel	6.8H	6.8V	10.7H	10.7V	18.7H	18.7V	23.8H	23.8V	37H	37V
T_b (K)	120	200	150	200	200	250	230	260	200	250
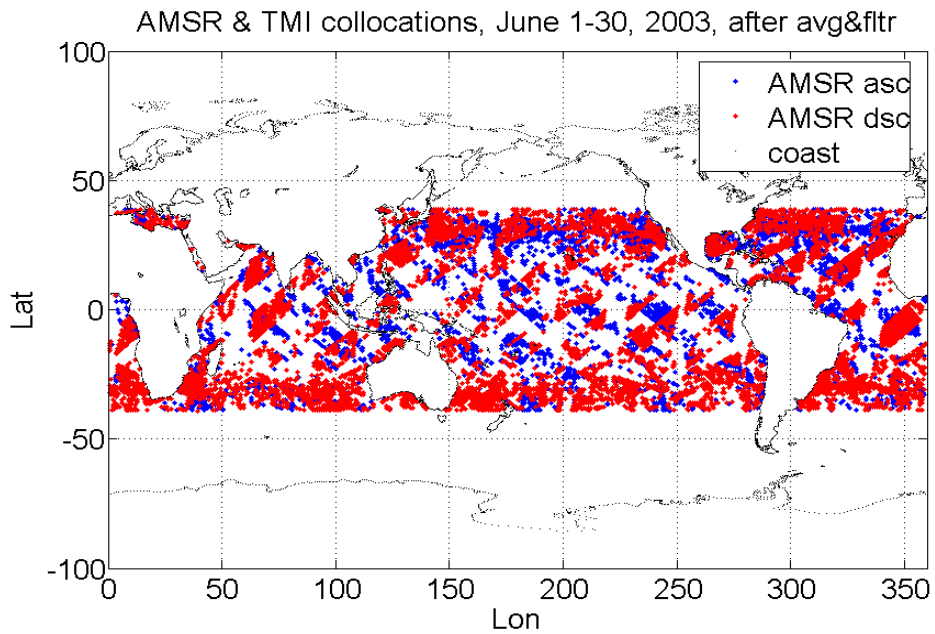
Figure 3.4: Collocations Between AMSR and TMI
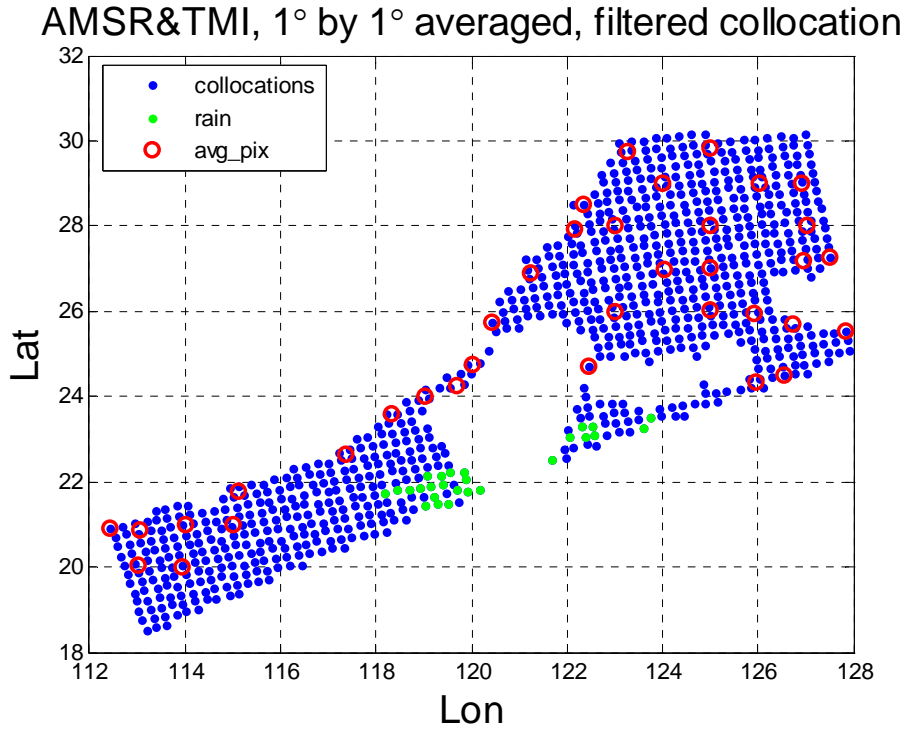
Figure 3.5: Example of AMSR and TMI Collocation

An example of the global AMSR and TMI collections during June, 2003 after box averaging and filtering is shown in Figure 3.4. There are 4149 collocated boxes from AMSR ascending paths, and 6634 collocated boxes from AMSR descending paths. Figure 3.5 is a detailed view of all the individual points in one collocation event from a single pass. There are in total 23784 collocated boxes in the selected time periods of 72 days.

The first group of collocations between TMI and WindSat is taken during three one-week-long periods in 2003, Nov.1 to Nov.7, Nov. 13 to Nov. 19 and Nov. 28 to Dec. 4. Collocations lie on high latitudes (20~40deg and -40~-20deg) during the first and third time periods, while those during the second time period lie on low latitudes (-20~20deg). Another group of collocations is chosen to analyze the seasonal stability of the calibration. Those data are the first seven days of each month of November 2003, February 2004, May 2004 and August 2004. For finding the collocations, we apply a temporal tolerance of ±15 minutes and a spatial tolerance of ±25 km. WindSat T_b's are Sensor Data Record (SDR) products with antenna pattern and polarization rotation angle corrections. The same data filtering and averaging procedures used in AMSR and TMI collocations are applied to these collocations. Upper bound limits for WindSat channels are shown in Table 3.3. The global TMI and WindSat collocations of the first group after box averaging and filtering, are shown in Figure 3.6. There are a total of 4816 collocations between TMI and WindSat during the selected week. There are 9213 boxes of collocations between WindSat and TMI in total.
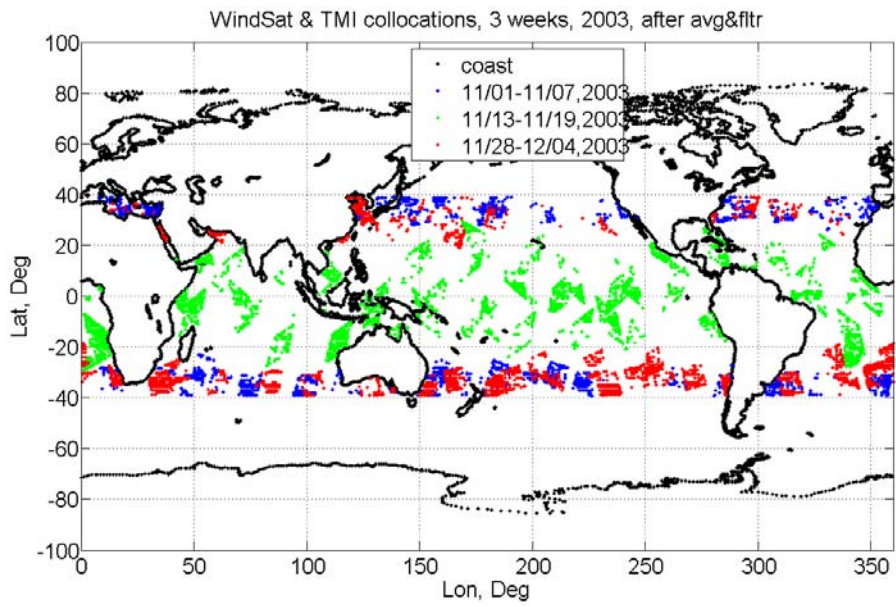
Figure 3.6: Collocations Between TMI and WindSat

CHAPTER 4 :   RADIATIVE TRANSFER MODELING

4.1   Radiative Transfer Theory

Since WindSat, TMI and AMSR have similar, but not identical, frequencies and earth incidence angles, some translation is needed to bring the collocated radiance measurements to a common basis for comparison. Because of the relatively high degree of homogeneity for oceanic scenes, theoretical modeling of radiative transfer is well suited for this purpose. Thus, a reliable radiative transfer model (RTM) is essential to inter-satellite calibration approaches, which have a physical basis.
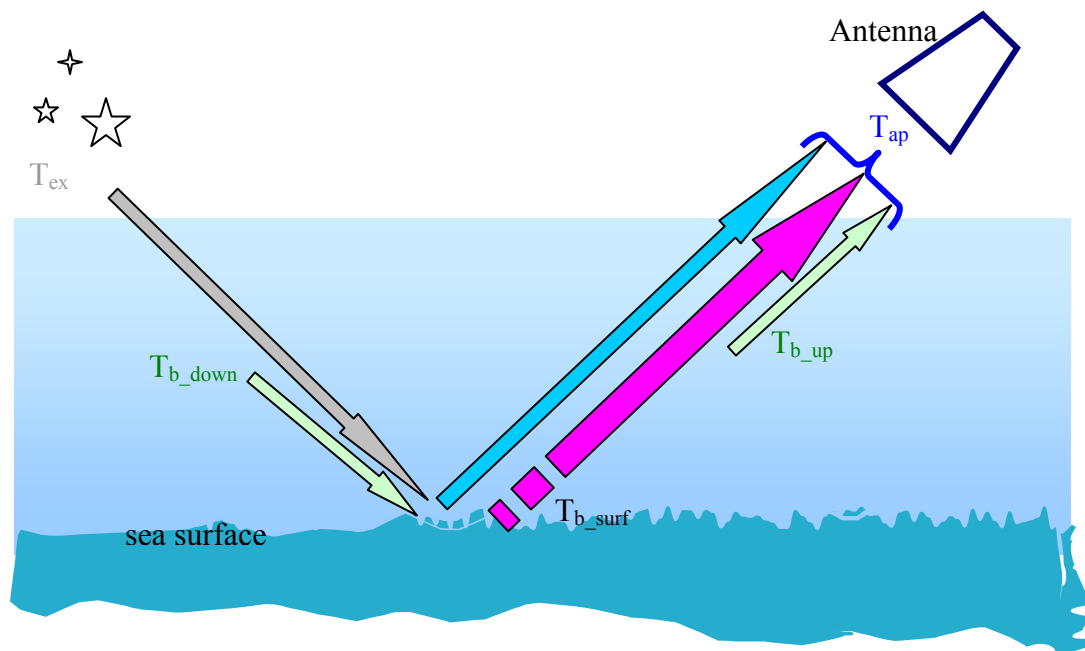
Figure 4.1: Radiative Transfer Model Over Ocean

Radiative transfer theory states that the T_b measured by a space-borne radiometer is the linear sum of individual contributions from the atmosphere and surface [2]. Figure 4.1 shows the major components that contribute to the apparent T_b captured by a radiometer antenna.

The sky brightness temperature, T_{sky} is defined as a sum of atmosphere down-welling and attenuated external (space) brightness temperature.

$$T_{sky} = \tau T_{ex} + T_{b\_down} \tag{4.1}$$

where τ is the atmospheric power transmissivity. The ocean surface reflects the sky brightness with some loss.

$$T_{refl} = (1 - \varepsilon) T_{sky} \tag{4.2}$$

where, ε is the ocean surface emissivity and ($1- \varepsilon$) is Fresnel power reflectivity. The ocean brightness temperature is

$$T_{b\_surf} = \varepsilon * SST \tag{4.3}$$

where, SST is the sea surface physical temperature in Kelvin. At the radiometer antenna, the apparent brightness temperature is the incoherent summation

$$T_{ap} = T_{b\_up} + \tau(T_{b\_surf} + T_{refl}) \tag{4.4}$$

4.2   Original Radiative Transfer Model

The inter-satellite calibration approach of Taylor series expansion prediction in this dissertation is built on simulation using a RTM known as RadTb. So, it is critical to start with tuning and validating the model to accurately simulate observed satellite radiometer measurements. RadTb is an improved version of the EnvaMod microwave RTM developed by

Wisler and Hollinger from the US Naval Research Lab in the 1970's [18]. The frequency range is approximately 1 GHz to 100 GHz with an incidence angle range of nadir (0°) to greater than 80° degrees and for dual linear polarizations (vertical and horizontal). This RTM is implemented using the FORTRAN programming language.

The RadTb takes as input fourteen environmental measurements of the ocean and atmosphere and three radiometric parameters. This radiative transfer process describes a nonlinear interaction between surface microwave emission, and the emission and absorption within the atmosphere that neglects scattering. With those important environmental parameters highlighted, this process is illustrated in a block diagram as shown in Figure 4.2. In the atmosphere, microwave absorption is primarily due to molecular oxygen, water vapor and cloud liquid water (rain omitted from this RTM). Each of these components has different optical properties and absorption spectra.
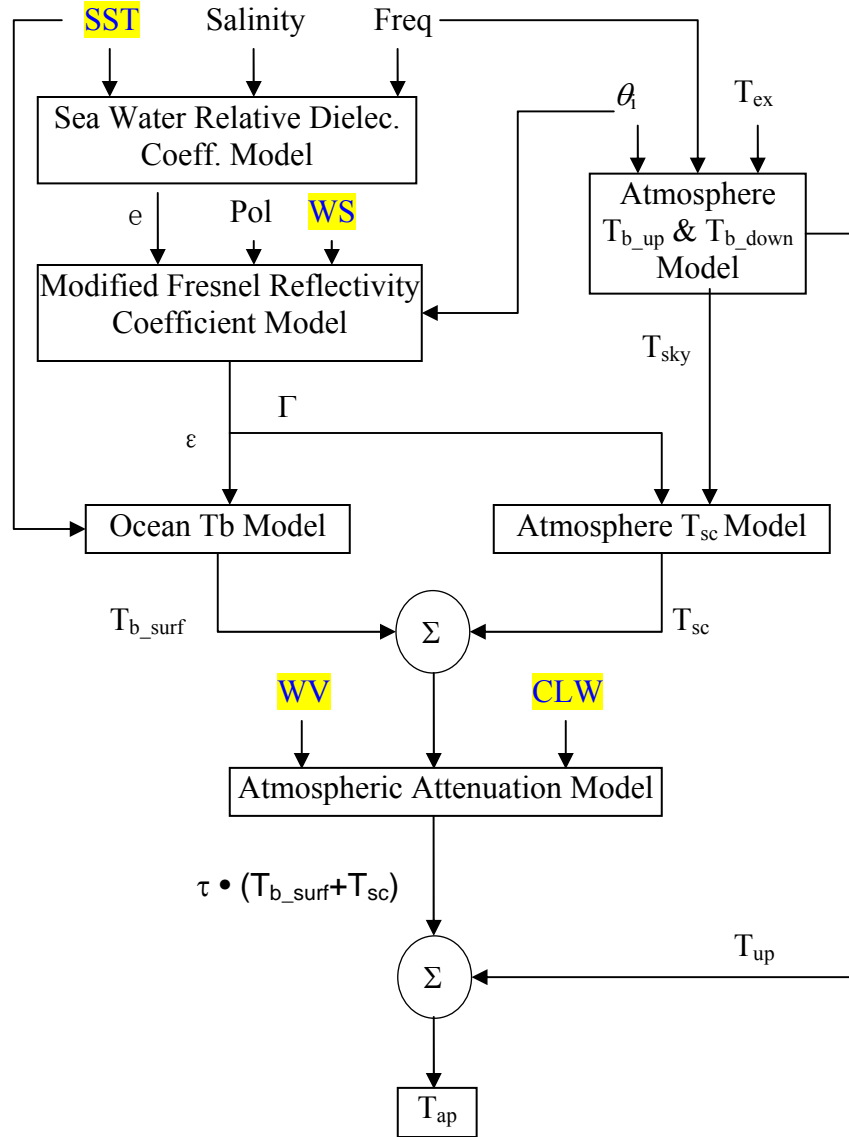
Figure 4.2: RTM Module

The relative complex dielectric constant (e) of seawater is modeled using the Debye equation, which is a function of sea surface temperature (SST), the dissolved salt content (salinity), and the EM frequency [19, 20]. The polarized ocean Fresnel power reflection (Γ) is a function of the relative dielectric constant of air and seawater, the polarization of the EM wave

and the incidence angle of propagation [2]. By the conservation of energy, the ocean emissivity is $\varepsilon = (1 - \Gamma)$, which is different for V- and H-polarizations. Also, the small-scale roughness of the ocean surface caused by the frictional air drag reduces the reflectivity as does the foam created by breaking ocean waves. This effect of surface winds on the emissivity is highly non-linear at strong winds, which complicates the modeling of the sea surface radiometric properties [21 - 24]. Molecular oxygen, water vapor and cloud liquid water affects the microwave atmospheric emission and transmissivity, and they contribute to both the upwelling and downwelling *Tb's*. This is modeled in RadTb using Rosenkranz's oxygen absorption model [25, 26] and Alex Stogryn's water vapor algorithm from Gross's formula [27]. Further, rain is a complex radiometric transfer process that involves both absorption and scattering and which is very difficult to model; so we exclude rain areas when selecting geographic collocations for inter-satellite radiometric calibrations.

In 2003, Yan Sun [28] evaluated RadTb to determine the systematic errors in the calculation of the apparent nadir-viewing ocean brightness temperature. Comparisons were made to the TOPEX/Poseidon satellite microwave radiometer (TMR) brightness temperature of the 18, 21 and 37 GHz channels viewing nadir over a variety of oceanic and atmospheric conditions. Results showed that the calculated T_b's followed the measurements quite well, except for small offsets (~3 - 5K) in the absolute. Her thesis suggested that future research should address the removal of T_b biases and "tune" the RadTb model to match a variety of satellite measurements from off-nadir viewing and two polarizations .

Later in 2004, Simonetta Thompson [29] evaluated the systematic biases produced by RadTb over a wider range of environmental conditions for off-nadir global viewing at four frequencies and for dual polarizations. She performed a statistical comparison of calculated and

measured brightness temperatures for WindSat using near-simultaneous collocations of numerical weather model results (NCEP) [30, 31] and microwave atmospheric parameter retrievals from SSM/I on DMSP F-13 satellite and the WindSat. Results showed that the systematic T_b error was produced in part by the ocean emissivity, which was not correctly accounting for the brightness temperature at different ranges of sea surface temperature. Thus, an empirical second-order adjustment was made to the emissivity factor as a function of SST in the RadTb model for the observed frequencies with respect to vertical and horizontal polarizations. The emissivity corrections showed significant improvement of calculated T_b's especially at the 6.8 and 10.7 GHz. The 18.7 and 37.0 GHz calculated brightness temperatures were also improved, but high water vapor contributed to error in the calculated T_b at sea surface temperature above 20° C. This observation suggested that the RadTb model needs to be improved to better model the water vapor parameter for the calculated brightness temperatures. The RTM evaluation also shows that high wind speed skews the calculated T_b results.

After adjustments and corrections were performed during research for this dissertation, the current version of RadTb has been modified to use ocean surface emissivity from Meissner and Wentz's dielectric constant and wind speed model (0 to 20 m/s) [24]. Further, the following adjustments are applied to the algorithms in RadTb to alleviate simulation errors dependence on several geophysical parameters: (1) the effect of partial cloud filling in the field of view is considered and an adjustment to the corresponding saturated water vapor value is made; (2) a revised correction to sea surface emissivity is made as a 2nd order polynomial of SST, and (3) an ad hoc adjustment to the input of atmospheric water vapor is made from satellite microwave radiometer retrievals. Details of these modifications are discussed in the following paragraphs.

4.3   RTM Refinements

4.3.1   RTM Tuning Data Source

The data set for tuning and validating the RadTb RTM is generated from approximately 4.7 M total cases of WindSat-GDAS collocations during October 2003 (~20 days). The T_b's are from WindSat Sensor Data Records (SDR), atmospheric profiles are from GDAS, and sea surface temperature, wind speed, columnar water vapor and cloud liquid water are from WindSat Environmental Data Records (EDR's). Salinity values are monthly averages from National Oceanographic Data Center World Ocean Atlas (NODC WOA 1998) salinity. Since rain has a strong effect on T_b measurements and is not included in our radiative transfer model, we avoid rainy areas. Finally, frequency and Earth Incidence Angle (EIA) are radiometer inputs to the RadTb RTM.

4.3.1.1 GDAS Data

The National Centers for Environmental Prediction's (NCEP) Global Data Assimilation System (GDAS) is a global analysis of the Earth's atmosphere and ocean surface generated every 6 hours for 00Z, 06Z, 12Z, and 18Z [32, 33]. The analysis incorporates a variety of meteorological and oceanographic measurements from buoys, ships, planes, radiosondes, weather radars, and earth orbiting satellites. The product version used for generating RMT inputs has a resolution of 1º by 1º global latitude/longitude. Atmospheric parameter profiles have 21 levels defined by atmosphere pressure between sea-level and 100 milibars. The list of surface

and profile parameters from this GDAS version is shown in Table 4.1 [33]. The collocation was

performed by interpolating every selected GDAS parameter at the corner of a 1º latitude by 1º

longitude bin which the WindSat SDR point fell in within ±3 hours. Thus, every WindSat SDR

point has a corresponding collocated set of GDAS parameters [32, 33].

Table 4.1: GDAS Grid Geophysical Parameters

	PARAMETER	UNITS	DESCRIPTION
1	Atmospheric Pressure	Pa	Surface Pressure
2	Sea Surface Temperature	K	Temperature at ocean surface
3	2 Meter Temperature	K	Temperature at 2 m above surface
4	Total Precipitable Water	kg/m^2	Total Atmospheric Column Precipitable Water
5	Cloud Liquid Water	kg/m^2	Total Atmospheric Column Cloud Liquid Water
6	Ice	N/A	Ice Flag, 0 to 1 (1 being ice)
7	Land	N/A	Land Flag, 0 = water, 1 = Land
8	Surface Wind Speed	m/s	Wind Speed at 10m above ocean surface
9	Surface Wind Direction	Degrees	Wind Direction at 10m above ocean surface
10	Wind Speed Profile	m/s	Wind Speed at 21 pressure levels
11	Wind Direction Profile	Degrees	Wind Direction at 21 pressure levels
12	Geopotential Height Profile	M	Geopotential Height at 21 pressure levels
13	Temperature Profile	K	Temperature at 21 pressure levels
14	Relative Humidity Profile	%	Percent Relative Humidity at 21 pressure levels
15	Cloud Water Profile	kg/kg	Cloud Water at 21 pressure levels

4.3.1.2 Calculating RTM Inputs

Geophysical data taken directly from the sources were converted or processed to generate

proper inputs to the RadTb, and the list of RTM input requirements are shown in Table 4.2.

Table 4.2: Description of RadTb Inputs

	RadTb Input	Unit	Source	Item in Source Data	Conversion
1	Month	N/A	SDR	File name	N/A
2	Longitude	deg	SDR	Longitude	N/A
3	Latitude	deg	SDR	Latitude	N/A
4	Surface Pressure	mb	GDAS	Atmospheric Pressure	GDAS(1)*0.01
5	Surface Air Temp.	°C	GDAS	2 Meter Temperature	GDAS(3)-273.16
6	Lapse Rate	°C/km	GDAS	Calculate from the Temp. vs. Height	FUNC(GDAS(13), GDAS(12))
7	Surface Absolute Humidity	g/m^2	GDAS	Calculate scale height, then AHS	FUNC(GDAS(14), GDAS(15), GDAS(12))
8	Water Vapor	g/cm^2	EDR	Water_Vapor	N/A
9	Mixing Ratio	N/A	Const.	N/A	2.00E-06
10	Cloud Liquid Water	g/cm^2	EDR	Cloud_Liquid_Water	N/A
11	Rain Rate	mm/hr	EDR	Rain_Rate	N/A
12	Wind Speed	m/s	EDR	Model_Wind_Speed	N/A
13	Sea Surface Temp.	°C	GDAS	Sea Surface Temperature	N/A
14	Salinity	PPT	WOA	from monthly salinity data	N/A

4.3.1.2.1 Lapse Rate

The calculation of Lapse Rate (LR) from GDAS data is the slope from the linear regression of, layer 1 to 15

$$T = LR \times H + T_0 \tag{4.5}$$

where T's are the set of temperatures at different heights from the Temperature Profile. H is the corresponding geopotential height (meters) for the pressure profile.

4.3.1.2.2 Surface Absolute Humidity

To calculate surface absolute humidity, calculations were performed with data from layers 1 to 7. In each layer, the saturated water vapor density ρ_{sat} (g/m^3) is calculated from temperature T (C)

$$\rho_{sat} = 4 \times 10^{-6} T^4 + 2.7 \times 10^{-5} T^3 + 0.013 T^2 + 0.34 T + 4.6 \tag{4.6}$$

Then, the actual water vapor density ρ_v (g/m^3) at each layer is computed as

$$\rho_v = RH \times \rho_{sat} \tag{4.7}$$

where, RH is the relative humidity and

$$\rho_v = \rho_0 e^{-z/H_{wv}} \tag{4.8}$$

where, z is the altitude in km. Taking the natural logarithm of the above equation, the water vapor scale height H_{wv} is calculated from the slope of regression between altitude z and ρ_v. Then the surface water vapor density is computed from

$$\rho_0 = WV / H_{wv} \tag{4.9}$$

where, WV is the columnar water vapor in mm.

4.3.1.2.3 TTP, HCB and HCT

From the input of Month and Latitude, RTM calculates Temperature of Tropopause, Height of cloud base (HCB) and Height of cloud top (HCT) using climatology.

HCB is set to 0.3 km. HCT is interpolated from the Table 4.3, which is used for calculation of HCT's in the Northern Hemisphere. Seasons are reversed when calculating HCT's in the Southern Hemisphere, unit is km.

Table 4.3: HCT Climatology for Northern Hemisphere (km)

Locations	1	2	3
LAT	7.5	38.7	71
winter	1.6	1.4	1.4
spring	1.8	1.3	1.1
summer	1.8	1.3	1.3
autumn	1.6	1.5	1.8

Temperature of Tropopause was interpolated from the Table 4.4, which is used for calculations in both the Northern and Southern Hemispheres.

Table 4.4 : TTP Climatology

Locations	1	2	3
Abs(LAT) (deg)	7.5	38.7	71
TTP (K)	193	218	220

4.3.2   RadTb Tuning Procedures

The RadTb works fine with moderate environmental conditions, but the natural climate has larger geophysical parameter variations. Sea surface temperature, wind speed, water vapor and cloud liquid water are the four major parameters we need to consider, and the effects to brightness temperature calculation from each of them needs to be evaluated and corrected. In this dissertation, further RTM refinements are applied to correct the brightness temperature calculation as a function of various environmental parameters in order:

1)   RTM inputs from WindSat and GDAS collocations instead of WindSat and NCEP collocations

2)   TTP, HCT, HCB calculated from month and latitude using climatology

3)   Fractional Clouds (or Cloud Fraction, CF) effect on absolute humidity calculation

4)   Dielectric constant and emissivity model with Wentz's model instead of Stogryn's

5)   Second order polynomial of SST as a correction to emissivity, and thus T_{b_surf}

6)   WV input correction to channels with Freq. > 20 GHz

During the tuning, the four major geophysical parameters were classified as the following

categories in Table 4.5 for ease of conditional analysis.

Table 4.5: Classifications of four major geophysical parameters

Geophysical parameter classifications	Wind Speed (m/s)	Water Vapor (mm)	Sea Surface Temperature (C)	Cloud Liquid Water (mm)
Low	≤4	≤20	≤10	≤0.1
Medium	4<WS<8	20<WV<40	10<SST<20	0.1<CLW<0.2
High	≥8	≥40	≥20	≥0.2

Note: geophysical conditions are indicated in the order of WS, WV, SST and CLW

4.3.2.1 Partial CLW Effects

When validating RTM simulations, we noticed that some of the histograms of the error distributions ($T_{b\_meas} - T_{b\_modeled}$) exhibited bi-modal rather than typical Gaussian distributions. By analyzing the relation between errors and geophysical parameters, we found that it was the effect of cloud liquid water (CLW) that lead to dual modes. This is because the absolute humidity (AH) was set to 100% relative humidity when clouds appear in that layer. This caused over adjustment for the humidity value when the clouds were light and only partially fill the antenna field of view. Our modification to the calculation of absolute humidity in clouds was to add a new variable, cloud fraction (CF) whose value varies from 0 to 1 to represent 0 to 100 percent fraction of clouds in the field of view. When the columnar CLW is greater than 0.1mm, CF is defined as 1, and when the columnar CLW is less than 0.001mm, CF is defined as 0.05. Between these values, cloud fraction is modeled to be inversely proportional to the exponential of CLW, such that

$$CF = 1 - e^{-b \times CLW} \tag{4.10}$$

where , b = 51.3/mm and the units of cloud liquid water are mm. Therefore the modified AH in a

layer where clouds exist is given by

$$AH = AH_{no\_cloud}(1 - CF) + AH_{100\%humidity}CF \qquad (4.11)$$

By applying the CF correction, the dual modes in the histogram of differences between

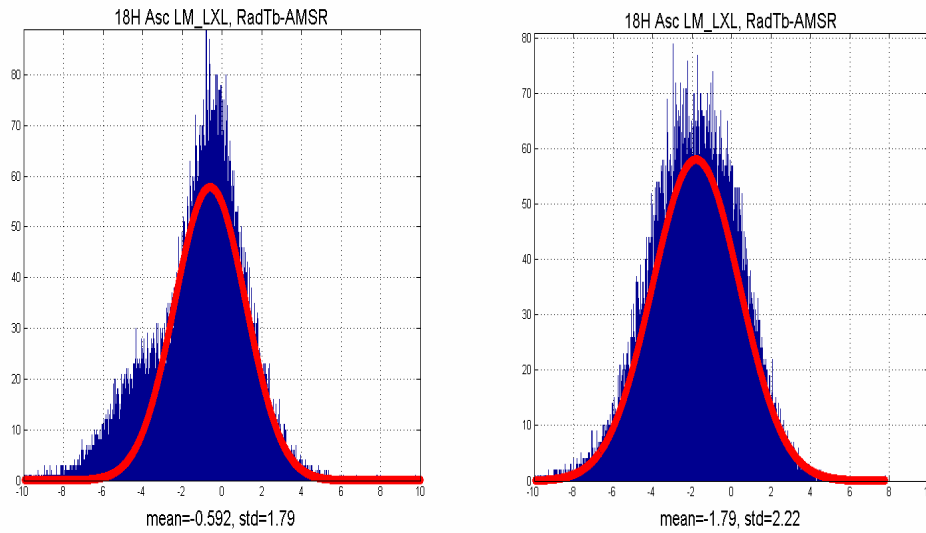RadTb simulated T_b's and radiometer observations disappear as seen in Figure 4.3.

Figure 4.3: CF Correction Effects on ΔT_b Histograms

The plot on the left is histogram of ΔT_b before CF is introduced; the plot on the right is
histogram of ΔT_b after CF is applied to the AH calculation

4.3.2.2 New Emissivity Model

Since ocean short-wave spectrum modeling is still an open issue, rough sea surface emissivity models remain questionable. Although the accuracy of radiative transfer and emissivity models is subject to debate, the global error of brightness temperature simulations with different models is lower than 5 K from comparison studies [10, 22, 23, 34]. For this dissertation we have adopted a well-known and accredited surface emissivity model from Frank Wentz [24]. His model is restricted to only a limited range of incidence angle 49 to 57 degrees which is common for satellite radiometer observations; and this model combines the effect of foam percentage and other roughness effects in one rough emissivity term. Wentz is considered the best surface emissivity model for higher incidence angles in his region, because it was validated against a long-term set of satellite radiometer measurements and has produced excellent comparisons with geophysical retrievals [21].

Surface winds cause roughening of the ocean surface by the generation of small ocean waves of centimeter length. Roughening the surface decreases the power reflectivity and therefore, by the conservation of energy, increases the emissivity. Further white caps, formed by breaking waves, have low reflectivity and can be considered as approximately a high emissivity blackbody [21 - 24]. Following paragraphs describe Wentz's emissivity model with wind effects considered [24].

The Fresnel equations calculate horizontal and vertical polarization voltage reflectivity coefficients

$$\rho_H = \frac{\cos\theta_i - \sqrt{\varepsilon - \sin^2\theta_i}}{\cos\theta_i + \sqrt{\varepsilon - \sin^2\theta_i}}$$

(4.12)

$$\rho_V = \frac{\varepsilon \cos\theta_i - \sqrt{\varepsilon - \sin^2\theta_i}}{\varepsilon \cos\theta_i + \sqrt{\varepsilon - \sin^2\theta_i}}$$

(4.13)

where, θ_i is the incidence angle. ε is the dielectric constant of sea water . The power reflectivity of horizontal polarization is

$$\Gamma_{0H} = |\rho_H|^2$$

(4.14)

and the power reflectivity of vertical polarization is

$$\Gamma_{0V} = |\rho_V|^2 + \Delta\Gamma_V$$

(4.15)

where $\Delta\Gamma_V$ is a correction term.

$$\Delta\Gamma_V = 4.887 \times 10^{-8} - 6.108 \times 10^{-8} \times (T_{surf} - 273)^3$$

(4.16)

where T_{surf} denotes the sea surface temperature. So, for both horizontal and vertical polarizations the reflectivity R_{geo} from the standard geometric optics model is given by

$$\Gamma_{geo} = \Gamma_0 - [r_0 + r_1(\theta_i - 53) + r_2(T_{surf} - 288) + r_3(\theta_i - 53)(T_{surf} - 288)]WS$$

(4.17)

where r_0, r_1, r_2 amd r_3 are coefficients which vary with frequency and polarization. WS is the surface wind speed in m/s. The final reflectivity of sea surface is computed as

$$\Gamma = (1 - F)\Gamma_{geo}$$

(4.18)

where F term is used to account for both foam and diffraction effects. The calculation equation for F is categorized in three different wind speed cases, when the wind speed is lower than 3m/s

$$F = m_1 WS$$

(4.19)

when the wind speed is greater than W_1 and lower than W_2, the equation is

$$F = m_1 WS + \frac{1}{2}(m_2 - m_1)(WS - W_1)^2 / (W_2 - W_1)$$

(4.20)

and when wind speed is higher than W2

$$F = m_2 WS - \frac{1}{2}(m_2 - m_1)(W_2 + W_1)$$

(4.21)

Thresholds for horizontal polarization are W1=7 m/s and W2=12 m/s, and the thresholds for vertical polarization are W1=3 m/s and W2=12 m/s. The sea surface emissivity ε can be calculated from $\varepsilon = 1-\Gamma$.

The above model was written as subroutines in FORTRAN language and added in the RadTb RTM.

4.3.2.3 <u>Second Order SST Polynomial Correction To Surface Emissivity</u>

Because of the excellent radiometric calibration of the Windsat [35 - 37], we use the measured ocean apparent T_b's to tune the RadTb. To improve comparisons of the modeled and measured T_b's, we introduce an empirical additive correction to the sea surface emissivity. We model the atmospheric upwelling and reflected sky brightness components and use these to estimate the measured ocean surface brightness. We define F(SST) as the difference between the estimated measured and the modeled ocean surface brightness temperatures

$$T_{app\_model} = T_{up} + \tau \left(T_{surf\_model} + (1-\varepsilon)T_{sky} \right)$$

(4.22)

$$T_{app\_measure} = T_{up} + \tau \left(T_{surf\_measure} + (1-\varepsilon)T_{sky} \right)$$

(4.23)

$$T_{surf\_measure} - T_{surf\_model} = F(SST)$$

(4.24)

$$T_{app\_measure} = T_{up} + \tau \left(T_{surf\_model} + F(SST) + (1-\varepsilon)T_{sky} \right)$$

(4.25)

where, T_{app_model} is the RTM calculated apparent brightness temperature, $T_{app\_measure}$ is the apparent brightness temperature from radiometer measurements. The T_{surf_model} is the RTM ocean surface brightness temperature, and $T_{surf\_measure}$ is the estimated ocean surface brightness temperature from radiometer measurements (adjusted for atmospheric effects). The sky brightness temperature, T_{sky}, is the combination of downwelling atmospheric emission and cosmic and galactic radiation, SST is the sea surface temperature, ε is the microwave emissivity of the ocean surface, and F(SST) is a second order polynomial of SST and T_{up} is the upwelling atmospheric emission.

The accuracy of the emissivity calculation is particularly important to the apparent brightness temperature calculation. Ocean surface brightness emission is the product of ocean emissivity and sea surface temperature. Including reflected T_{sky}, there are two parts that involve emissivity in the calculation of T_{app}. Since T_{sky} is only around 1/10 of SST, a small emissivity error contribution to the reflected T_{sky} is negligible compared to its effect on surface emission. So, the correction to the emissivity calculation calls for a correction to T_{surf_model} with a polynomial of SST. A plot of surface emission T_b differences (measured − modeled) versus SST was analyzed and a second order polynomial of SST was derived for F(SST) in equation 4.24. Then the F(SST) is applied to the calculation of T_{app} as an additive emissivity correction in equation 4.25.

The RTM tuning using F(SST) was performed by limiting, or bounding geophysical conditions (e.g. wind speed less than 8m/s, sea surface temperature under 27°C, columnar water vapor less than 20mm, columnar cloud liquid water less than 0.1mm). These conditions were selected to avoid more severe environmental conditions, which are difficult to model accurately. The resulting F(SST) was determined using 650,000 cases of measurements from vertical and

horizontal polarization channels of all WindSat frequencies (6.8, 10.7, 18.7, 23.8 and 37 GHz) and coefficients for any other radiometer frequencies can be calculated by interpolation.
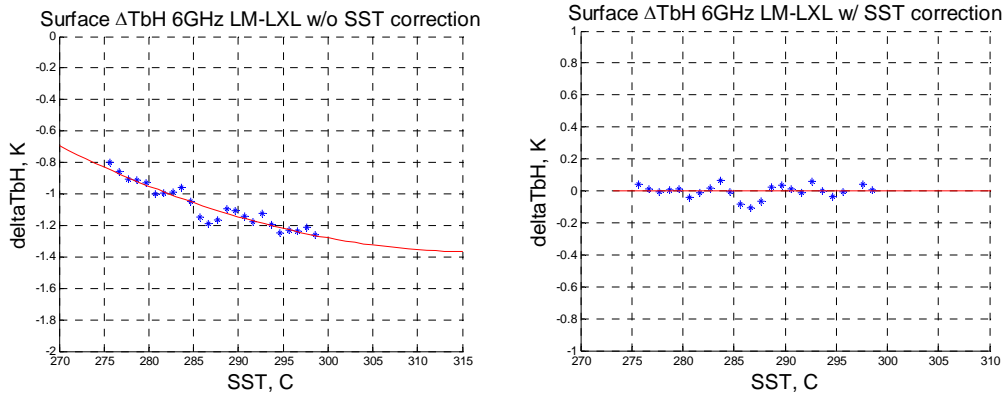

Figure 4.4: ΔT_b Variation With SST Before and After Emissivity Correction

Figure 4.4 shows an example of the emissivity correction to 6.8 GHz horizontal polarization channel and the best-fit second order polynomial that fits the scatter plot and represents F(SST). The right-hand panel plot shows an excellent match of RTM calculated surface brightness temperatures with the estimated WindSat surface brightness measurements after implementing the emissivity corrections.

After tuning, RadTb gives good results at all WindSat frequencies and there are very small biases between model simulations and WindSat measurements under the above constrained environmental conditions. Further, the model was validated with approximately 5 million cases over a wide range of geophysical conditions, and Fig 4.5 shows the corresponding differences between RadTb surface T_b simulations and WindSat estimated surface observations in each channel. The biases of RTM simulation for 6.8, 10.7, 18.7 and 23.8 GHz channels are less than 0.5K, and the largest bias at 37 GHz horizontal polarization channel is around 1K. The standard

deviation in model results increases as frequency increases, from 1K at 6.8 GHz to 4K at 23.8 GHz, and slightly decreases to around 3.5K at 37 GHz. Since the Windsat instantaneous incidence angle varies from case to case (< ± 0.5°) and the fixed nominal values used for the RTM simulations are slightly different, there are random differences of up to 1K, depending upon polarization and frequency.

For other frequencies, the coefficients for SST polynomials are created by interpolations from WindSat channels.
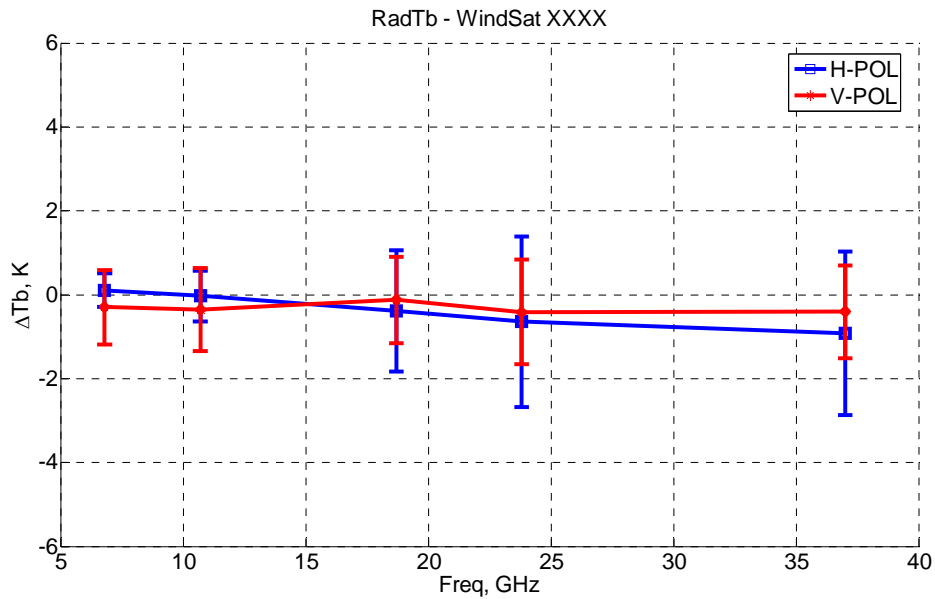
Figure 4.5: RTM Validation With WindSat Measurements

under all geophysical conditions

4.3.2.4 <u>Correction of Water Vapor Input</u>

For 5,000 random cases, under limited geophysical conditions (LM)XXL (See Table 4.5), comparisons of RadTb calculated Tb's and WindSat measurements showed large differences in the 23 GHz and 37 GHz channels that were functions of water vapor.

After extensive investigation of the water vapor absorption modeling used in RadTb, it was postulated that these differences were due to possible biases in the retrieved water vapor input parameter. Therefore, in order to reduce the observed differences between measured and modeled T_b's, an ad hoc correction was made to the microwave retrieved water vapor input to RadTb. By varying the correction value, within a range between -10 and 15 mm, the local minimum was found for the difference between RadTb T_b's and WindSat measurements, and the resulting correction found which minimized T_b difference. The correction values for all tuning cases were then plotted against the water vapor inputs and a third order polynomial fit was made as a function of water vapor.
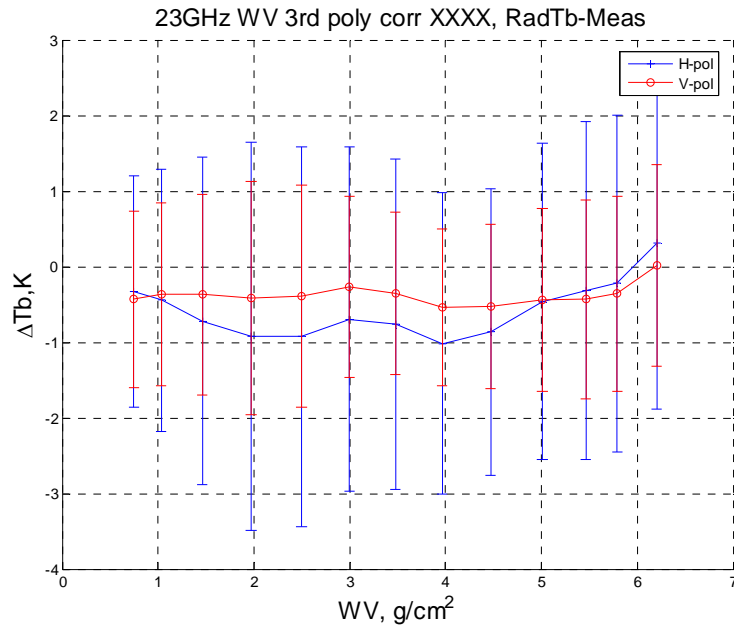
Figure 4.6: ΔT_b Variations with Water Vapor at 23 GHz Channels
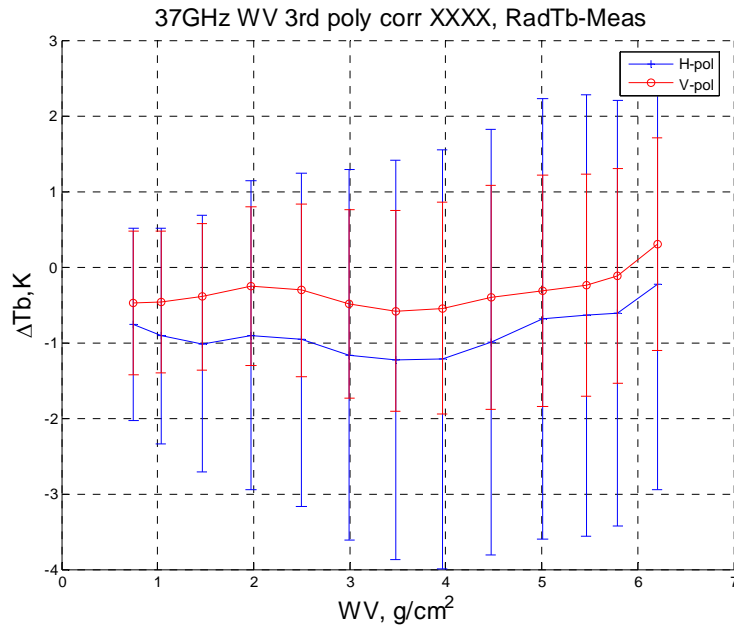
Figure 4.7: ΔT_b Variations with Water Vapor at 37 GHz Channels

For the 23 GHz and 37 GHz channels, the variations of T_b differences between the RadTb and WindSat measurements are less than ± 0.5K under MXXL geophysical conditions after the correction. Figures 4.6 and 4.7 show that the variation of T_b differences versus water vapor is almost within -1 to 0K for 23 G and 37 GHz channels under all geophysical conditions.

4.3.3   Evaluation of Tuned RTM

After tuned with the above procedures, RadTb was evaluated with comparisons to WindSat measurements under different geophysical conditions, and results for variations of wind speed (WS) and SST are shown in the following paragraphs.

4.3.3.1 Delta-T$_b$ versus WS

Plots in Fig 4.8, panels (a) to (j) show the variation of difference of RadTb and WindSat comparisons with wind speed changes. In most circumstances, ΔT_b's (defined as RadTb minus WindSat measurement) are within ± 1K, but there are exceptions, especially for wind speeds from 10m/s to 20m/s. For example, at 6.8 and 18.7 GHz horizontal channels, ΔT_b increases from 0K to 4K and ΔT_b drops from -1K to -2K, respectively. Also, for the 23.8 GHz horizontal channel, ΔT_b varies from -2K to 2K. Finally, for 37 GHz, the horizontal channel ΔT_b varies from 2K to -2K; and the vertical channel, ΔT_b drops from -1K to -2K.
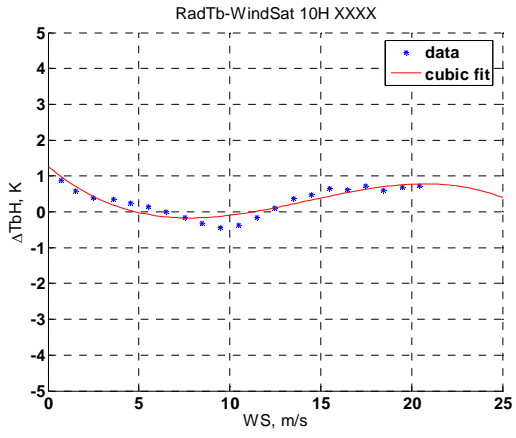
On the other hand, analysis of the same ΔT_b versus wind speed while limiting geophysical conditions to WV < 20mm and CLW < 0.1mm showed that WV and CLW didn't affect the trend much. Most differences between the two different conditions were within 0.3K, with maximum of 0.5k.
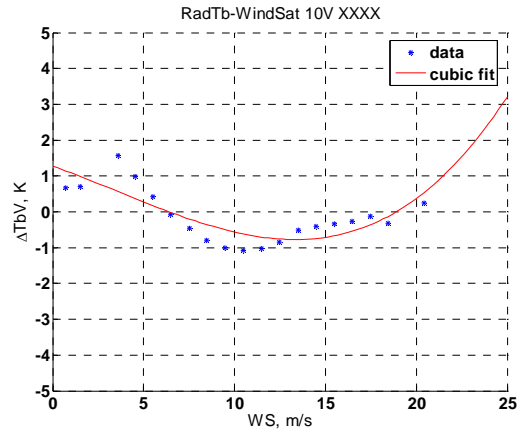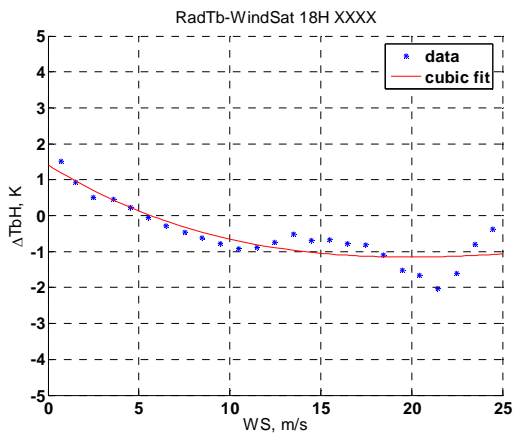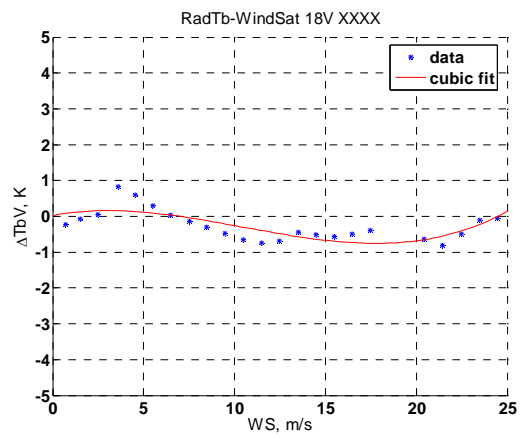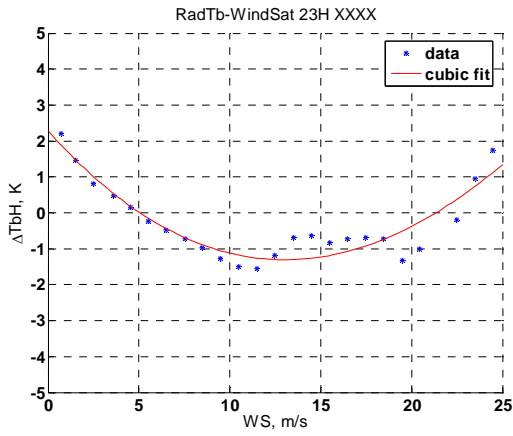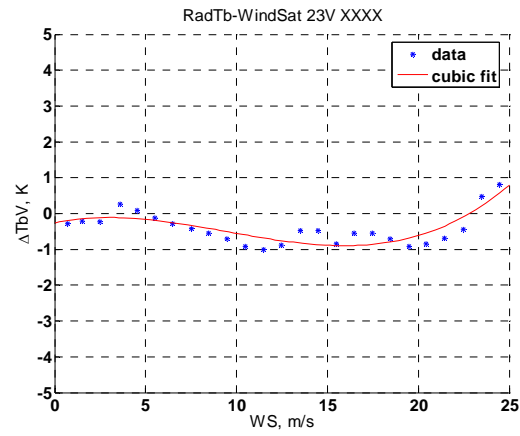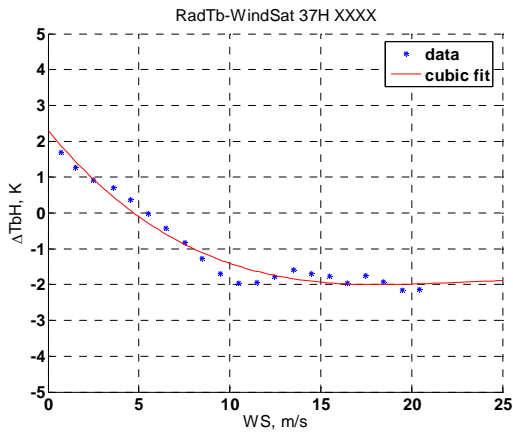
(a)

(b)

(c)
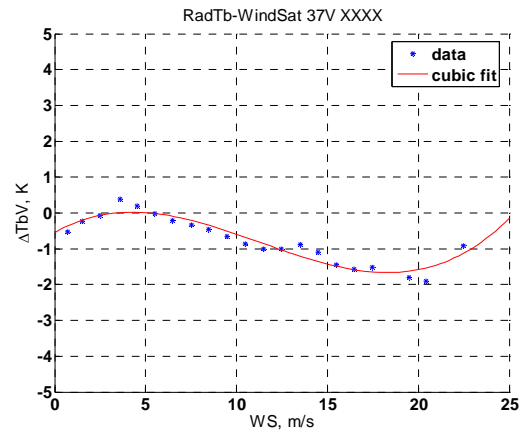
(d)

(e)

(f)

49
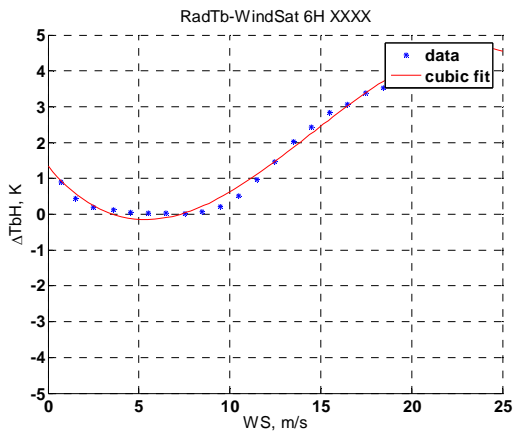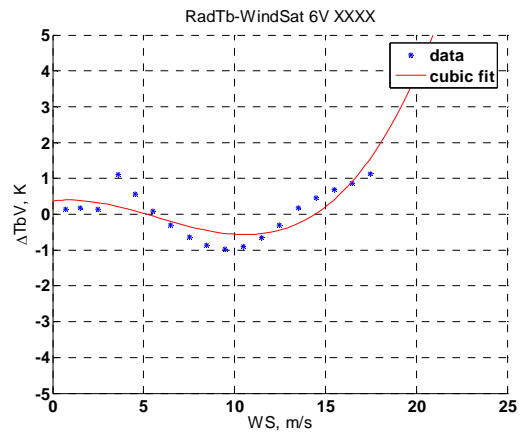
Figure 4.8: ΔT_b Variations with Wind Speed

4.3.3.2 Delta-T_b versus SST under different WS

T_b biases between RadTb and WindSat measurements were analyzed under different wind speed and water vapor bins (environmental parameter ranges). The plots in Appendix C show examples of T_b bias variation with SST. For 6.8 GHz channels, ΔT_b's are close to 0 except for two cases. Under HLXL condition, H-pol ΔT_b's are higher than 1K at low SST's. Under

HHXL condition, ΔT_b's are around -1K. For 10.7 GHz channels, H-pol ΔT_b's are close to 0 in all cases. V-pol ΔT_b's show 1K bias under low wind speed conditions and -1K bias under high wind speed conditions. For 18.7 GHz channels, the HHXL case shows a large bias of around -2.5K while other cases are within 1K. The 23.8 GHz and 37 GHz channels are most affected by water vapor line. And their ΔT_b's show the same slopes and biases in every case. The ΔT_b biases increase up to -3K with the raise of WV. WV effects on ΔT_b's are much larger than WS effects in 23.8 and 37 GHz channels.

4.3.3.3 Delta-T_b versus SST under different WV

In Appendix D, plots show ΔT_b variations with SST under limited WS, WV and CLW conditions. While WS and CLW remain low, the increase of WV affects all channels in the same way for both horizontal and vertical polarizations. The 6.8 and 10.7 GHz channels are stable under medium WV (<40mm). With high WV (>40mm), RTM simulations of WindSat 18.7, 23.8 and 37 GHz channels show large fluctuations from measurements (> ±0.5K).

CHAPTER 5 :   FREQUENCY AND EIA NORMALIZATION

5.1 T_b Simulations from RTM

Under given geophysical conditions, the observed brightness temperature is determined by the parameters of the radiometer and the observation geometry. For different channels of the radiometer, or channels from different radiometers, the major differences are in frequency and viewing angle. Viewing angles include incidence angle and azimuth angle relative to wind direction, which was neglected in our current models. The idea of Taylor series expansion calibration is to normalize frequencies and EIA's between source and target channels. The relations between T_b's and frequencies are derived from simulations using a validated radiative transfer model (RadTb) described in chapter 4.

So, by simulating radiometric measurements of brightness temperature under given geophysical conditions and with a fixed incidence angle, at a given polarization, we can derive a relation between T_b's and operating frequency, such as

$$Tb = polynomial(freq)$$

(5.1)

For the full range of probable of geophysical conditions, radiometer measurements were simulated for different channels from 30-days of WindSat EDR's and associated GDAS collocations. With these geophysical parameters as inputs to the RadTb, all channels of AMSR, TMI and WindSat were simulated at their operating frequencies but with the incidence angle fixed at 53.2°, which is the incidence angle for TMI. Taylor series are then derived for the frequency transforms from these simulated T_b's.

The frequency spectrum of T_b's varies as a function of geophysical conditions and of vertical and horizontal polarizations; and as a result, they are characterized separately. Of the 14 RadTb environmental inputs, Wind speed, water vapor, sea surface temperature and cloud liquid water are four major factors that affect microwave apparent brightness temperatures. Considering the distribution of environmental conditions, the sensitivity of T_b to geophysical parameters, and the desired accuracy of frequency normalization, we categorize these four geophysical parameters into different ranges, as defined in Table 5.1. So, a total of over 4.7 million observed environmental cases were sorted into 12,960 (= 6*36*10*6) categories of geophysical conditions for vertical or horizontal polarizations, while neglecting the variations of other (minor) geophysical parameters.

Table 5.1: Categorization of Major Geophysical Parameters

Geophysical parameter classifications	Wind Speed (m/s)	Water Vapor (mm)	Sea Surface Temperature (C)	Cloud Liquid Water (mm)
Range	0 - 25	0 - 70	0 - 36	0 - 0.5
Transformation	WS/5+1	WV/2+1	SST/4+1	CLW*10+1
Num. of Levels	6	36	10	6

Never the less, not all of these 12,960 categories were adequately populated because some of the categories are extreme conditions that are rare. Thus, there are no radiometer observations in categories where they are unnatural conditions e.g. high water vapor at cold sea surface temperature. Since the majority of our cross-calibration opportunities occur over tropical oceans, these 4.7 million cases are very sufficient for calibrations in our research, and the simulated T_b's from these cases are averaged in each of the geophysical categories.

T_b simulations are performed using RadTb with 33 frequencies (4, 5, 6, 6.8, 6.925, 7, 8, 9, 10, 10.65, 10.7, 12, 14, 16, 18.7, 19.35, 20, 21.3, 22, 22.2, 23, 23.8, 25, 27, 29, 31, 33, 35, 36.5, 37, 38, 39, & 41 GHz) and an EIA of 53.2° as inputs. Polynomials of order 21 are used for the fit that resulted in residuals < 1K for most cases. Exceptions are with frequencies close to the 22.2 GHz water vapor line and under WV > 20mm conditions. For these conditions, there are two ways to reduce these regression residuals, by dividing frequencies ranges into different sections and by having more T_b simulations around 22.2 GHz. Deriving polynomial of frequencies over the full range of 4 to 41 GHz will be used for generalized cross-calibrations between any radiometers working at this frequency range. On the other hand, for the purpose of cross-calibrating WindSat and TMI, or AMSR and TMI, polynomials can be derived from T_b simulations over the reduced frequency range of these three radiometers with adequate accuracy and much less computing.

5.2   Frequency and EIA Normalization

The Taylor series expansion of T_b as a function of frequency about a source f_o is

$$T_b(f_1) = T_b(f_0) + T_b'(f_0) \cdot (f_1 - f_0) + T_b''(f_0) \cdot \frac{(f_1 - f_0)^2}{2!} + T_b'''(f_0) \cdot \frac{(f_1 - f_0)^3}{3!} + \dots$$
$$+ T_b^{(n)}(f_0) \cdot \frac{(f_1 - f_0)^n}{n!} + \dots$$

(5.2)

$$T_b^{(n)} = \left. \frac{\partial^{(n)} T_b(f)}{\partial f^{(n)}} \right|_{f=f_o}$$

(5.3)

where, $T_b(f)$ is the brightness temperature as a function of frequency, f_1 is the frequency of the destination channel, and f_o is the frequency of the source channel.

For the normalization of incidence angle difference between radiometer channels, the same algorithm is applied, and the variation of T_b as a function of incidence angle is derived from the RadTb with other parameters fixed. For the full-range of environmental conditions and within the range of incidence angles of AMSR, TMI and WindSat, the T_b is approximately a linear function of incidence angle. Thus the transformation can be expressed as in equation 5.4, with coefficients varying for different geophysical conditions.

$$T_b(\theta_1) = T_b(\theta_0) + \partial(T)/\partial(\theta) \times (\theta_1 - \theta_0)$$

(5.4)

Because of the design of the WindSat feed array, the incidence angles vary with the different channels. Further, the actual on-orbit incidence angles are slightly different from designed values. From the statistics of WindSat SDR's used in our collocations, the lowest incidence angle is approximately 50.38° for the 10.7 GHz channels, and the highest is approximately 55.89° for the 18.7 GHz channels. Under typical orbit conditions, the variation of incidence angles for each channel is approximately ±0.5° standard deviation about its mean value. For TMI, the mean incidence angle for all channels is approximately 53.2° and the variation is approximately ±0.3°. For AMSR, the channel incidence angles are not recorded in the data product used in this study, so the published nominal value of 55.0° has been assumed for all channels.

Frequency and incidence angle transforms are performed sequentially. For the calibration of TMI, the strategy used was to transform the T_b's of the WindSat channels from their incidence angles to that of TMI channels before applying the frequency transforms. On the other hand, for the calibration of AMSR, order of transforms was reversed.

5.3   WindSat to TMI Calibration

An example of the apparent T_b spectrum for typical environmental conditions is shown in Figure 5.1 with the channel frequencies of TMI, WindSat and AMSR identified. A Taylor series expansion for frequency normalization is calculated on the basis of T_b simulations at a fixed incidence angle of 53.2°, corresponding to TMI. Thus, for the WindSat to TMI calibration, the incidence angle transform is performed first by converting WindSat measurements to equivalent T_b's at the TMI incidence angle; then the following frequency transforms are performed. The source channel frequency is selected with smallest difference from target channel frequency and preferably on the same side of water vapor line. All target TMI channels and their corresponding source WindSat channels are listed in Table 5.2.

For the TMI 10.65 GHz vertical polarization channel prediction, a Taylor series 4th order expansion is performed about the WindSat 10.7 GHz vertical channel. In each geophysical category, Taylor series coefficients (equation 5.3) are derived from a 5th order polynomial fit to curves of T_b versus frequency formed by RadTb simulated T_b's of WindSat 6.8, 10.7, 18.7, 23.8 and 37 GHz and TMI 10.65 GHz vertical polarization channels.

To predict the TMI vertically polarized target channels, 19.35 and 21.3 GHz, the WindSat 18.7 GHz vertically polarized channel is selected as the source; and the same orders of T_b function polynomial fit and Taylor series expansion are used as the previous 10.65 GHz channel prediction. Also, the same procedures are applied to achieve TMI horizontal polarization channel predictions, except for 21.3 GHz where TMI has no horizontally polarized channel. Figures 5.2 and 5.3 show 3-D plots of ΔT_b (which is the sum of frequency and EIA normalization for WindSat 18.7 GHz channels to predict TMI 19.35 GHz channels) versus SST and WV. For

56

both polarizations, ΔT_b's increase with SST and WV; and over the whole SST and WV range, prediction of TMI 19.35 GHz horizontal polarization needs larger ΔT_b's added to the source WindSat channel than the vertical polarization.
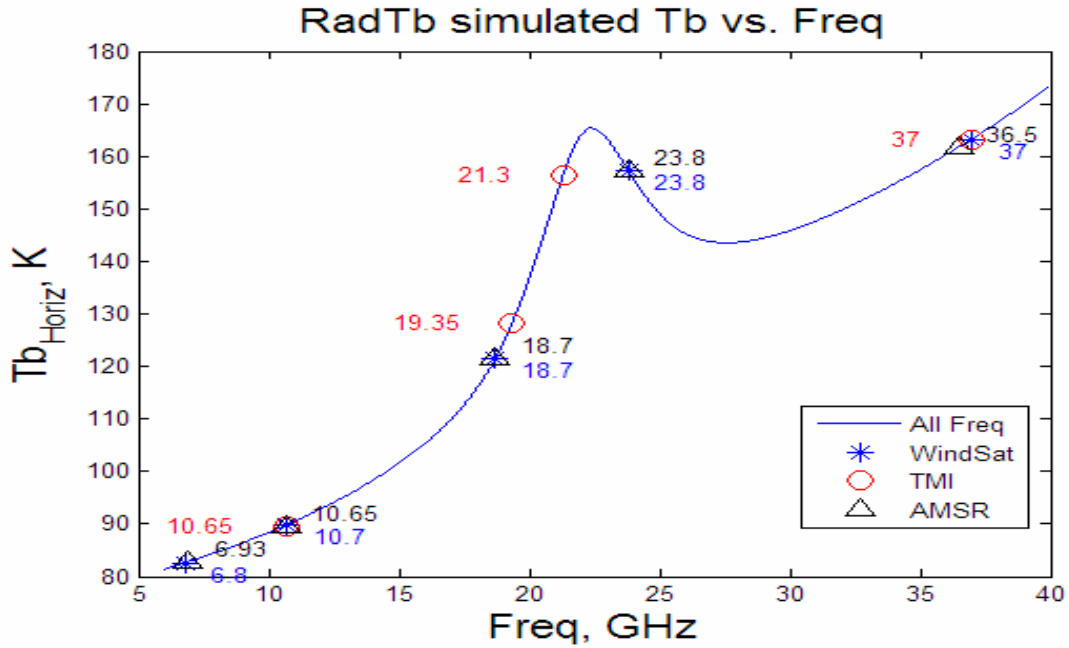

Figure 5.1: T_b Spectrum Example

Table 5.2: Source and Target Channels of WindSat to TMI Calibration

Example of ΔT_b under LMML Geophysical Condition, $\Delta T_b = \text{TMI} - \text{WindSat}$

Target: TMI f(GHz)	10.65H	10.65V	19.35H	19.35V	21.3V	37H	37V
Source: WindSat f(GHz)	10.7H	10.7V	18.7H	18.7V	18.7V	37H	37V
Freq. Norm. ΔT_b (K)	-0.10	-0.11	9.06	5.48	27.79	0.00	0.00
EIA Norm. ΔT_b (K)	-3.00	6.46	0.79	-6.79	-6.79	0.04	-0.65
Total ΔT_b (K)	-3.09	6.35	9.84	-1.31	21.00	0.04	-0.65
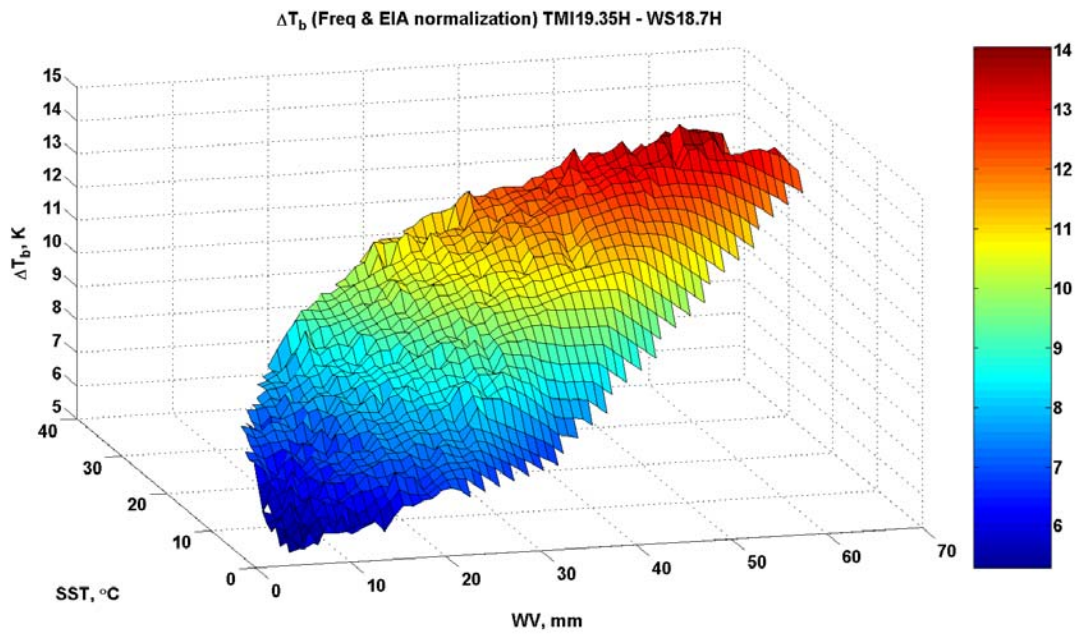
Figure 5.2: WindSat 18.7H to TMI 19.35H Freq. and EIA Normalization
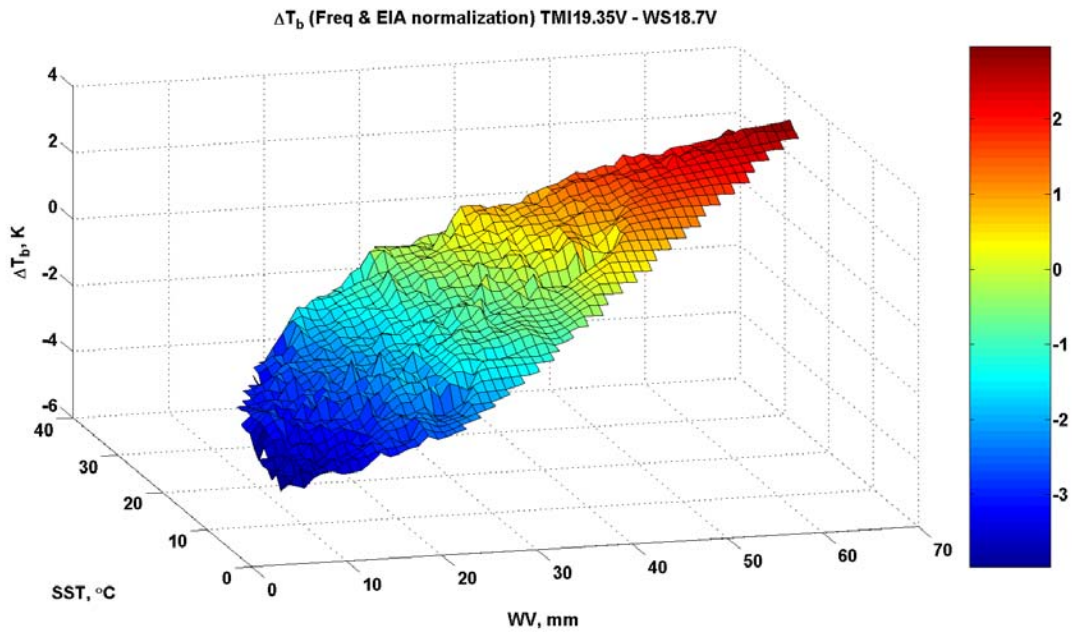
Figure 5.3: WindSat 18.7V to TMI 19.35V Freq. and EIA Normalization

For TMI 37 GHz channels, corresponding WindSat channels are at the identical frequency; thus, no frequency transform is needed in this case.

After these incidence angle and frequency normalizations, WindSat measurements are transformed to equivalent TMI channels and comparisons between TMI and transformed WindSat measurements are performed.

5.4   TMI to AMSR Calibration

Because the frequency normalization is based on RadTb simulations at the TMI incidence angle, the order of incidence angle and frequency transforms for TMI to AMSR calibration is reverse of the order for WindSat to TMI calibration. For TMI to AMSR calibrations, the TMI channels are the source which are transformed to equivalent T_b's at the AMSR frequencies; and target AMSR channels and their corresponding source TMI channels are listed in Table 5.3. Then, the equivalent T_b's are transformed from the TMI incidence angle to the AMSR incidence angle.

For the AMSR 6.925 GHz vertical polarization channel prediction, a TMI 10.65 GHz vertical channel Taylor series 3rd order expansion is used. In each geophysical category, these Taylor series coefficients are derived from a 4th order polynomial fit to the curves of T_b versus frequency from RadTb calculated T_b's of TMI 10.65, 19.35, 21.3 and 37 GHz and AMSR 6.925 GHz vertical polarization T_b's. Since both AMSR and TMI have 10.65 GHz channels, no frequency transform is needed in this case. The same procedures as in vertical channel predictions are applied to achieve the AMSR horizontal polarization channel predictions except for 23.8 GHz, which is predicted with the TMI 19.35 GHz horizontal channel.

Table 5.3: Source and Target Channels of TMI to AMSR Calibration

Example of ΔT_b under LMML Geophysical Condition

Target: AMSR f(GHz)	6.925H	10.65H	18.7H	23.8H	36.5H
Source: TMI f(GHz)	10.65H	10.65H	19.35H	19.35H	37H
Freq. Norm. ΔT_b (K)	-5.46	0.00	-9.06	35.81	-1.40
EIA Norm. ΔT_b (K)	-2.10	-1.96	-0.56	0.78	-0.21
ΔT_b :AMSR – TMI (K)	-7.56	-1.96	-9.61	36.59	-1.61
Target: AMSR f(GHz)	6.925V	10.65V	18.7V	23.8V	36.5V
Source: TMI f(GHz)	10.65V	10.65V	19.35V	21.3V	37V
Freq. Norm. ΔT_b (K)	-6.86	0.00	-5.48	-0.45	-0.91
EIA Norm. ΔT_b (K)	4.52	4.53	4.47	4.09	4.10
ΔT_b :AMSR – TMI (K)	-2.33	4.53	-1.01	3.64	3.19

After these incidence angle and frequency normalizations, TMI measurements are transformed to equivalent AMSR channels and comparisons between AMSR measurements and transformed TMI measurements are then performed.

5.5   Validation of Taylor Series Expansion Prediction

To access the accuracy of the Taylor series prediction procedure, a computer simulation was performed using 5000 cases of selected geophysical conditions (distinct from the RadTb tuning set). Afterwards, the Taylor series expansion prediction procedures were applied to these simulated T_b's; and in Fig. 5.4, results show small differences between predictions from WindSat RadTb simulated source channels by Taylor series expansion and TMI RadTb simulated target channels set. At the 10 and 37 GHz channels, there are negligible differences in channel frequencies; therefore the simulation validates the use of a first order incidence angle adjustment. At the 19 and 21 GHz channels, the frequency differences are 0.65 and 2.6 GHz respectively and

the larger standard deviation are believed to be a measure of the inability of the Taylor series to accurately predict the T_b simulation in the vicinity of the water vapor line (22.225 GHz peak). Fortunately, the differences are nearly zero in the mean.

An identical simulation was performed using the same 5000 geophysical cases but now using the TMI source channels to predict AMSR target frequencies. Results shown in Fig. 5.5 are similar with a few notable differences. First, the results at 6.9 GHz show a larger standard deviation over those at 10 GHz because TMI uses the 10.65 GHz source channel to predict both the AMSR 6.9 GHz and 10.65 GHz T_b's. This illustrates the difficulty of using the Taylor's series to predict T_b's when the frequency differences between the source and target channels become large. Never-the-less, the mean errors are nearly zero and the standard deviations are approximately less than 0.5 K. The standard deviation of errors in predicting AMSR 23.8 GHz, both vertical and horizontal channels, is larger than in other channels. Also, at the AMSR 23.8 GHz channel, the vertical polarization comparisons are significantly improved compared to the horizontal polarization comparisons. This is because of the difference in the source channels used for vertical and horizontal polarizations (TMI has no 21.3 GHz horizontal channel). The standard deviations of errors in predicting AMSR 36.5 GHz vertical and horizontal channels are less than 0.1 K, because the source TMI 37 GHz channels are very close in frequency and the difference between AMSR and TMI incidence angles is small ($\sim 1.8^o$).
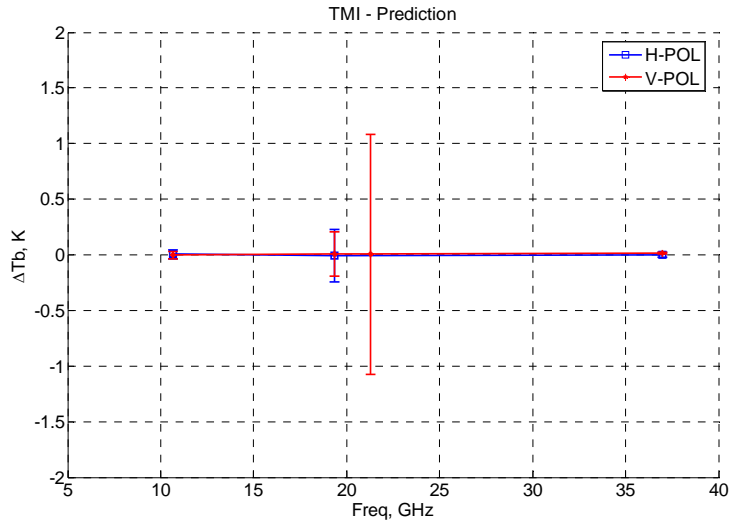
Figure 5.4: Taylor Series Prediction Validation between WindSat and TMI

where ΔT_b Equals to TMI Minus WindSat Prediction T_b's
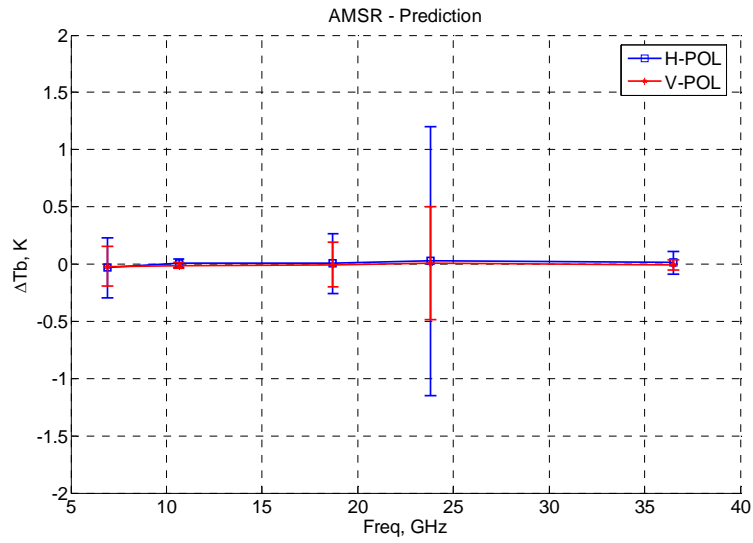
Figure 5.5: Taylor Series Prediction Validation between TMI and AMSR

where ΔT_b Equals to AMSR Minus TMI Prediction T_b's

For generalized inter-satellite cross-calibrations, predictions will be made from any source frequency to any target frequency, and Tables 5.4 - 5.7 show analysis of the errors from Taylor series predictions. Errors were taken as differences between Taylor series predictions and the RadTb simulated T_b's at frequencies around the source frequency. In the following tables, columns show frequency offset from center frequencies (GHz), and rows show samples of source frequencies. Most of the error biases are within ±1K, except for frequencies near 22.2 GHz. As described in the beginning of this chapter, segmented polynomial fits and denser samples of simulated T_b's around water vapor line would help reduce these prediction errors.

Table 5.4: Simulation Results: H-pol T_b Prediction Mean Errors (Kelvin)

Column is Frequency Difference of Target Channel (GHz) from Taylor Center Frequency and

Row is Taylor Series Center Frequency

Freq. (GHz)	-4	-2	-1	-0.5	-0.25	-0.1	0	0.1	0.25	0.5	1	2	4
10.65	-0.75	-0.44	-0.82	-0.43	-0.20	-0.07	0.00	0.05	0.11	0.14	-0.09	-1.06	0.37
10.7	-0.72	-0.52	-0.81	-0.40	-0.17	-0.06	0.00	0.05	0.11	0.12	-0.15	-1.11	0.41
18.7	2.52	0.83	-1.25	-1.17	-0.72	-0.32	0.00	0.19	0.54	1.28	3.04	3.02	1.13
19.35	1.18	-2.54	-2.73	-1.49	-0.82	-0.34	0.00	0.35	0.90	1.77	1.09	0.03	1.12
21.3	-2.61	-0.34	0.85	0.99	0.61	0.27	0.00	-0.29	-0.74	-1.43	-1.83	0.87	-1.23
37	1.27	0.14	2.18	1.77	0.99	0.41	0.00	-0.39	-0.91	-1.33	0.76	0.77	1.04

Table 5.5: Simulation Results: H-pol T_b Prediction Error Standard Deviation (Kelvin)

Column is Frequency Difference of Target Channel (GHz) from Taylor Center Frequency and

Row is Taylor Series Center Frequency

Freq. (GHz)	-4	-2	-1	-0.5	-0.25	-0.1	0	0.1	0.25	0.5	1	2	4
10.65	0.48	0.28	0.35	0.17	0.07	0.03	0.00	0.03	0.07	0.11	0.14	0.53	0.63
10.7	0.47	0.30	0.35	0.16	0.07	0.02	0.00	0.03	0.07	0.10	0.14	0.56	0.64
18.7	1.86	1.00	0.70	0.55	0.33	0.14	0.00	0.12	0.33	0.74	1.69	2.12	3.03
19.35	1.73	1.57	1.43	0.83	0.45	0.18	0.00	0.19	0.48	0.97	1.51	2.25	1.94
21.3	3.03	2.21	1.39	0.83	0.46	0.19	0.00	0.20	0.51	1.02	1.47	0.89	2.04
37	0.61	0.22	0.89	0.73	0.41	0.17	0.00	0.16	0.38	0.56	0.32	0.39	0.80

Table 5.6: Simulation Results: V-pol T_b Prediction Mean Errors (Kelvin)

Column is Frequency Difference of Target Channel (GHz) from Taylor Center Frequency and

Row is Taylor Series Center Frequency

Freq. (GHz)	-4	-2	-1	-0.5	-0.25	-0.1	0	0.1	0.25	0.5	1	2	4
10.65	-0.36	-0.22	-0.35	-0.15	-0.05	-0.02	0.00	0.02	0.08	0.13	0.03	-0.54	0.23
10.7	-0.33	-0.24	-0.33	-0.12	-0.03	0.00	0.00	0.05	0.11	0.14	0.01	-0.55	0.27
18.7	1.36	0.41	-0.72	-0.66	-0.40	-0.18	0.00	0.10	0.30	0.70	1.63	1.48	0.61
19.35	0.64	-1.42	-1.49	-0.80	-0.44	-0.18	0.00	0.19	0.47	0.92	0.47	-0.13	0.50
21.3	-1.31	-0.04	0.49	0.52	0.31	0.13	0.00	-0.14	-0.35	-0.65	-0.75	0.51	-0.51
37	0.64	0.01	1.08	0.89	0.50	0.21	0.00	-0.20	-0.46	-0.69	0.31	0.34	0.75

Table 5.7: Simulation Results: V-pol T_b Prediction Error Standard Deviation (Kelvin)

Column is Frequency Difference of Target Channel (GHz) from Taylor Center Frequency and

Row is Taylor Series Center Frequency

Freq. (GHz)	-4	-2	-1	-0.5	-0.25	-0.1	0	0.1	0.25	0.5	1	2	4
10.65	0.33	0.18	0.18	0.08	0.04	0.01	0.00	0.02	0.04	0.07	0.09	0.29	0.40
10.7	0.32	0.19	0.18	0.08	0.03	0.01	0.00	0.02	0.04	0.07	0.09	0.30	0.40
18.7	1.04	0.56	0.42	0.31	0.18	0.08	0.00	0.07	0.18	0.39	0.87	1.21	1.59
19.35	1.02	0.90	0.77	0.43	0.23	0.10	0.00	0.10	0.24	0.49	0.94	1.24	1.04
21.3	1.69	1.23	0.72	0.43	0.24	0.10	0.00	0.10	0.26	0.52	0.79	0.53	1.10
37	0.32	0.14	0.42	0.35	0.20	0.08	0.00	0.08	0.18	0.28	0.17	0.21	0.54

CHAPTER 6 :   RESULTS AND DISCUSSION

Inter-satellite radiometric calibrations were performed between WindSat, TMI and AMSR radiometers by applying the Taylor series expansion prediction technique with near-simultaneous collocated T_b measurements from these sensors. For comparison purposes, this same data set was also processed using the multi-channel regression calibration method.

6.1   Cross Calibration between WindSat and TMI

6.1.1 T_b Bias Temporal Variation

First, three groups of collocations between WindSat and TMI were analyzed during November 2003. There are over 1000 cases in each 1-week-long time period where T_b's were binned to 1° latitude by 1° longitude boxes and average values were calculated for each box, excluding rainy and noisy data where the standard deviation exceeded a fixed threshold (see chapter-3 for details). Changes in geo-location and geophysical condition of collocations cause differences in the number of filtered cases collected per week, and Figure 6.1 shows the geo-locations of boxes during these three weeks. The statistics of ΔT_b between TMI measurements and corresponding predictions from WindSat channels by Taylor series expansion are shown in Table 6.1; and similar results from the multi-channel regression approach are show in Table 6.2. In addition, Figure 6.2 shows scatter plots of TMI predictions vs. measurements during these selected 3 weeks with both approaches. With significant normalizations made for frequency and EIA differences, results from both approaches seem very consistent in the slopes of the scatter

66

plot for all channels. Both predictions present constant slopes (~1) and offsets (up to 4 K) from target channel measurements with small standard deviations (< 1.5 K for most of the channels in both approaches) during the 3 weeks. The largest difference in the amplitude of offsets between two calibration approaches is at 19.35 GHz horizontally polarized channel, which is roughly 1.6 K, as also seen in Tables 6.1 and 6.2.
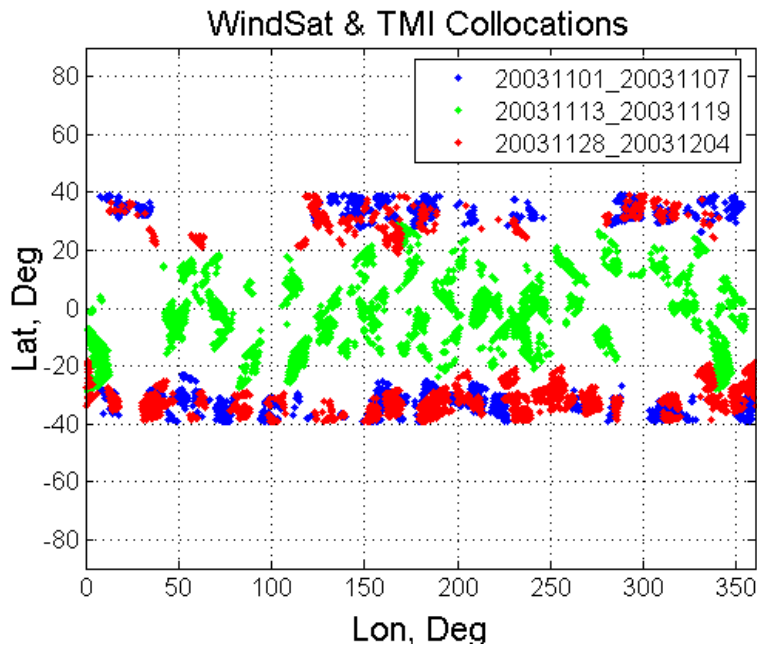
Figure 6.1: Geo-locations of WindSat and TMI Collocations (3 Weeks during 1 Month)

Table 6.1: ΔT_b in WindSat to TMI Prediction by Taylor Series Expansion (3 Weeks Data)

Δ= Prediction -TMI		10H	10V	19H	19V	21V	37H	37V	# cases
11/01-11/07	mean	2.32	0.09	4.34	1.26	3.50	2.87	3.26	1311
11/13-11/19	mean	1.92	-0.32	4.04	1.19	5.21	2.38	3.17	1983
11/28-12/04	mean	1.51	-0.78	3.50	0.58	2.69	1.77	2.37	1522
Total 3 Weeks	mean	1.88	-0.36	3.95	0.99	3.91	2.32	2.94	4816
	std	0.89	0.86	1.02	0.98	1.75	1.22	1.04	

Table 6.2: ΔT_b in WindSat to TMI Prediction by Multi-Channel Regression (3 Weeks Data)

Δ= Prediction -TMI		10H	10V	19H	19V	21V	37H	37V	# cases
11/01-11/07	mean	2.10	1.47	2.63	2.67	3.61	2.63	4.29	1311
11/13-11/19	mean	1.79	1.20	2.48	2.29	3.13	2.58	4.30	1983
11/28-12/04	mean	1.21	0.86	1.87	1.80	2.76	1.62	3.52	1522
Total 3 Weeks	mean	1.71	1.14	2.31	2.27	3.14	2.34	4.02	4816
	std	0.94	0.82	1.10	1.07	1.25	1.23	1.25	
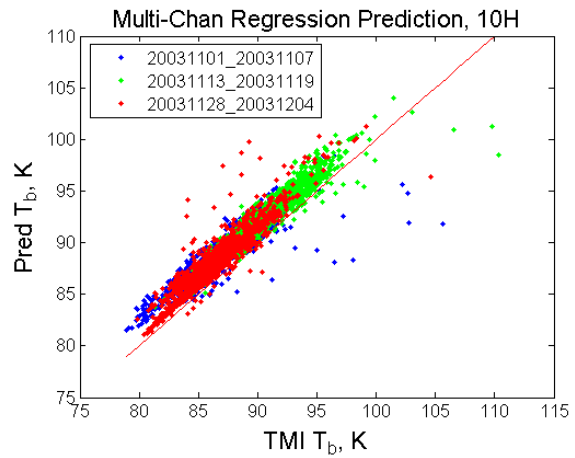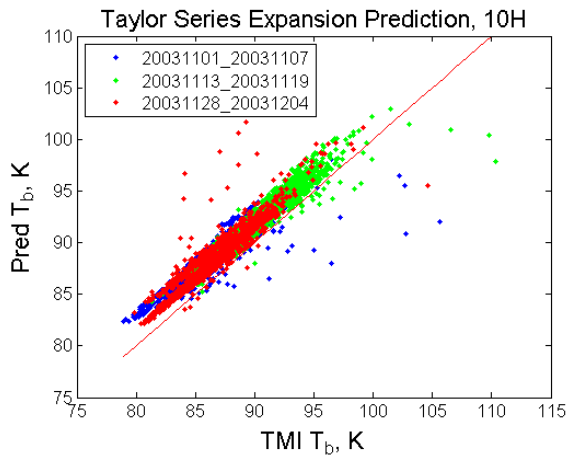
(a)   10.65 GHz, H-pol
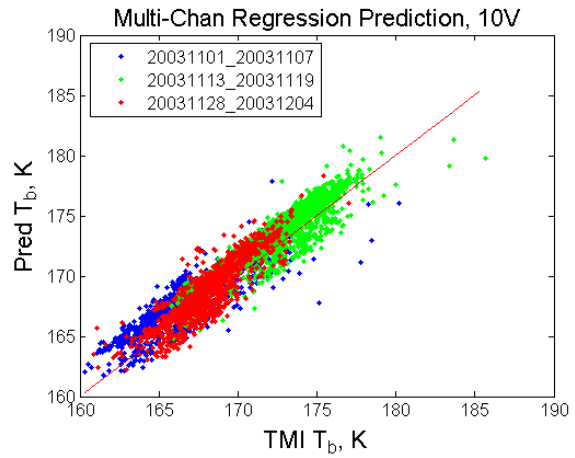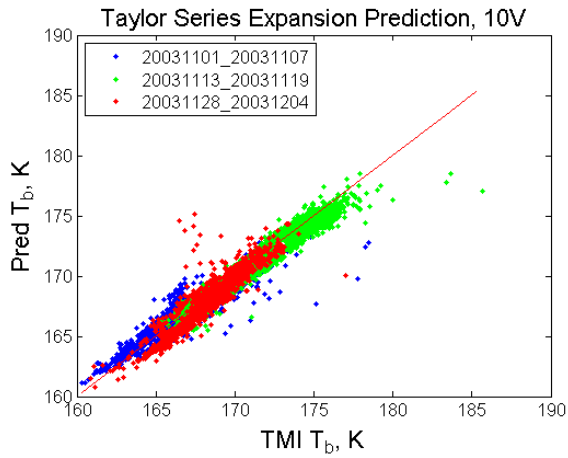
(b)   10.65 GHz, V-pol
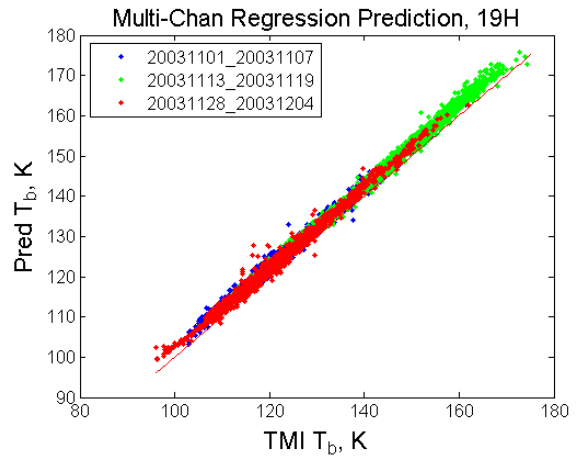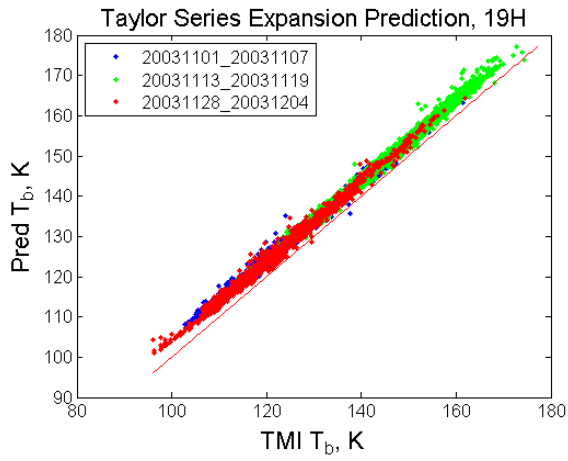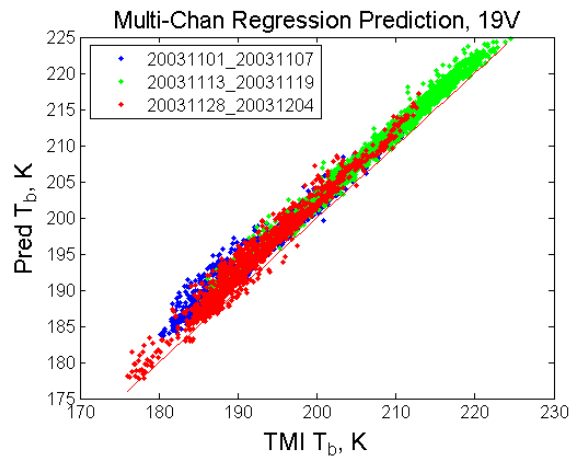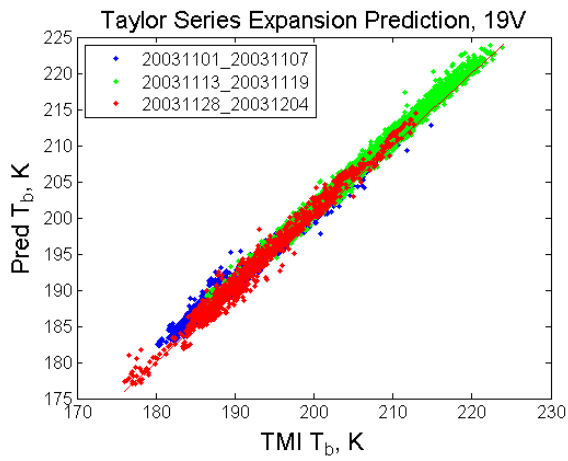
(c)   19.35 GHz, H-pol

(d)   19.35 GHz, V-pol
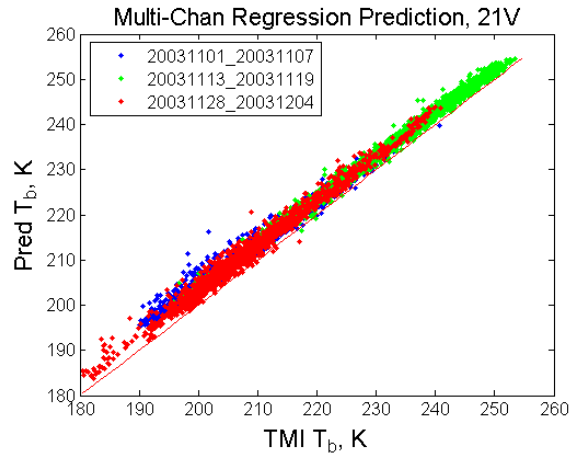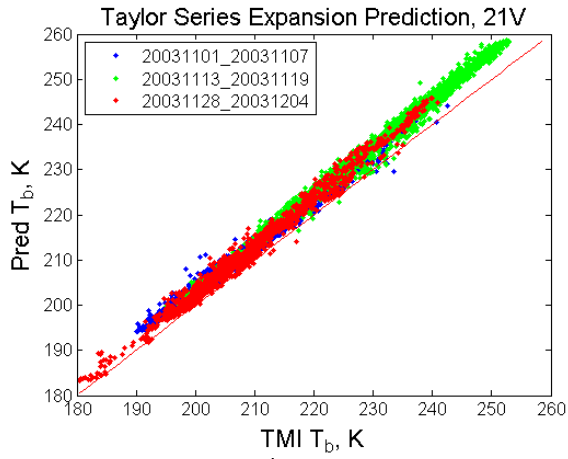
(e)   21.3 GHz, V-pol
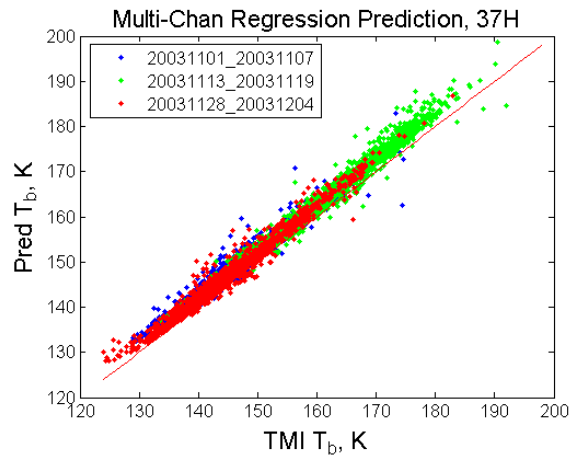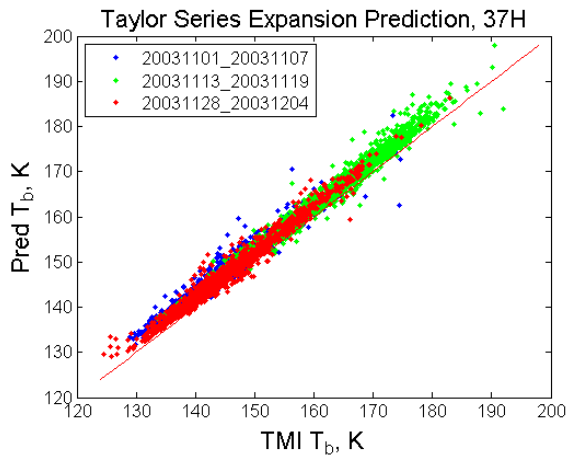
(f)   37 GHz, H-pol
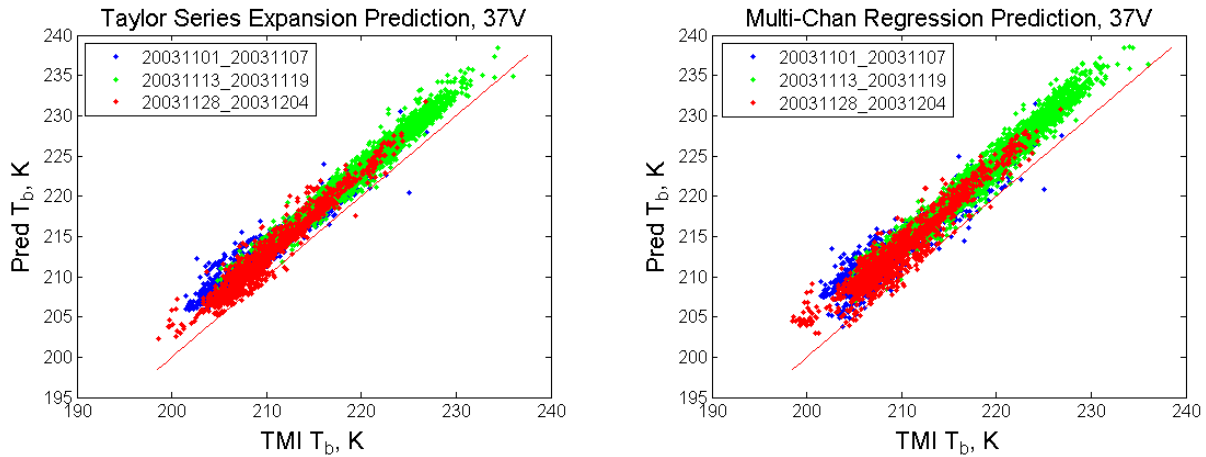
(g)   37 GHz, V-pol

Figure 6.2: TMI predictions (from WindSat) and collocated and simultaneous TMI

measurements (3 weeks).

Both approaches show that the predictions from the WindSat channels are larger than corresponding measurements for TMI channels during all selected time periods. The only exception is the 10.65 GHz vertical polarization channel for the Taylor series expansion, where the prediction is slightly smaller than the measurement. From these results for the TMI 10.65H and 37H channels, biases calculated using both approaches are very similar. Noticeably, the largest difference between biases in these two approaches occurs at 19.35 GHz H-pol channel, where it is approximately 1.64 K.

Results suggest a time dependence of the TMI biases observed from Nov. 1st to Dec. 4th in 2003. Plots in Figure 6.3 show slopes of around -1 K/month, excluding the 21.3 GHz V-pol channel. Moreover, in Figure 6.4, ΔT_b's of all channels in multi-channel regression prediction show similar slope of up to -1 K/month. This suggests a possible short term drift of cross calibrations between WindSat and TMI.

71
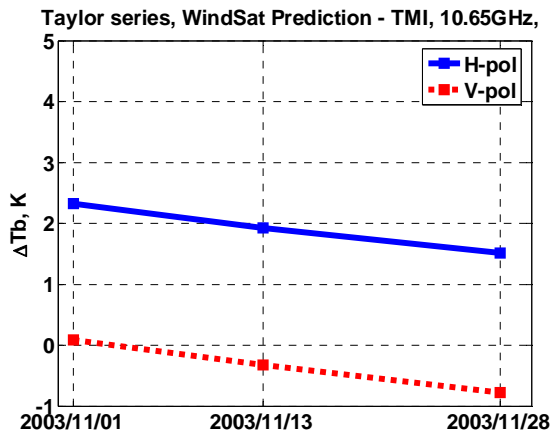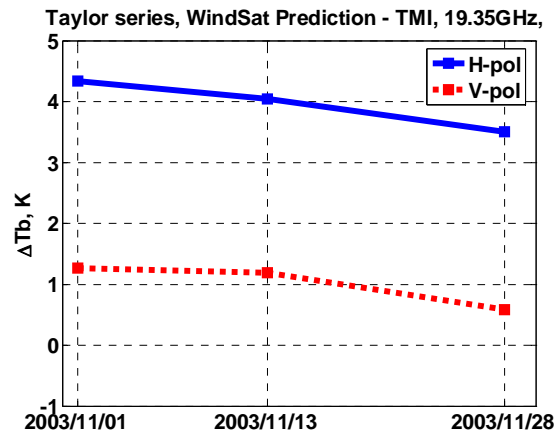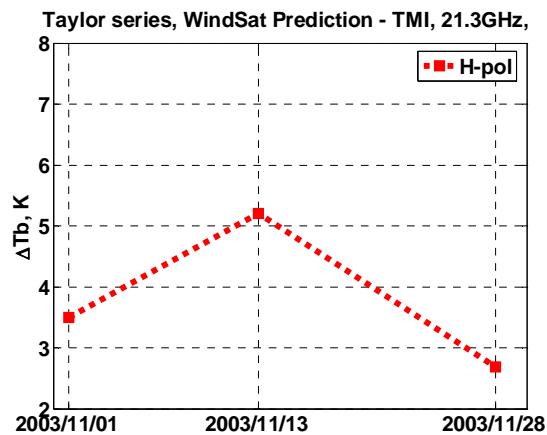
(a)   10.65 GHz
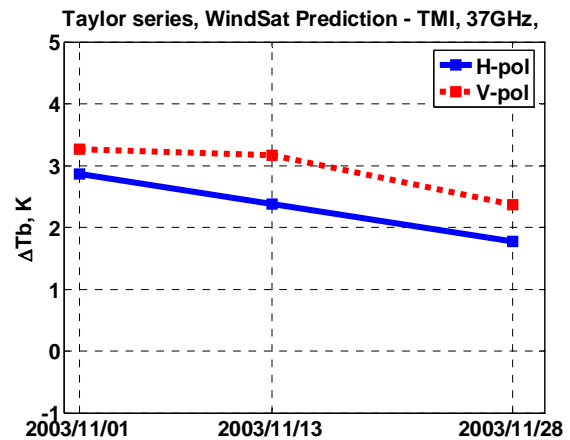
(b)   19.35 GHz

(c)   21.3 GHz

(d)   37 GHz

Figure 6.3: WindSat to TMI Calibration by Taylor Series Expansion Prediction (3 Weeks Data)
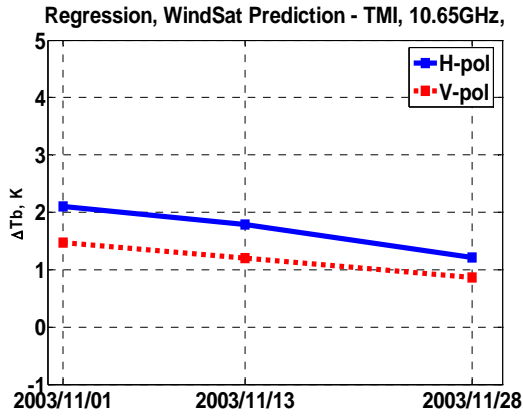
(a)   10.65 GHz   (b)   19.35 GHz
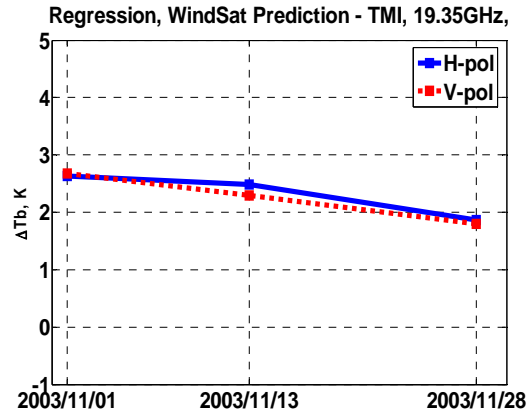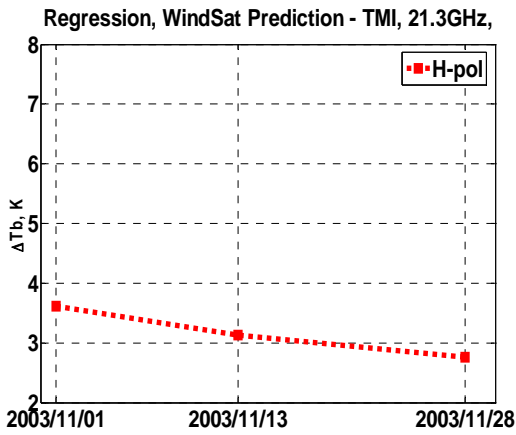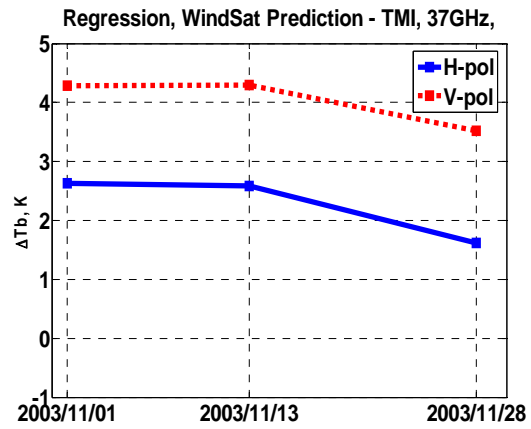
(c)   21.3 GHz   (d)   37 GHz

Figure 6.4: WindSat to TMI Calibration by Multi-Channel Regression Prediction (3 Weeks Data)

Also, another group of WindSat and TMI collocated data were analyzed by selecting one week's collocations per season over the period Nov. 2003 to Aug. 2004; and results from the two calibration approaches are shown in Tables 6.3 and 6.4. Here, the seasonal fluctuations of T_b biases are within a smaller range of approximately 0.5K, and there is no apparent time

73

dependence. Figure 6.5 shows geo-locations of boxes during these 4 weeks in different seasons; and there does not appear to be any latitudinal dependence of these biases. Figure 6.6 shows scatter plots of prediction vs. measurement during the selected 4 weeks with both approaches. Results, presented in both Figure 6.2 and Figure 6.6, are consistent. Plots in Figure 6.7 show the Taylor series expansion predicted ΔT_b's during these 4 weeks. Finally, Figure 6.8 shows plots of multi-channel regression predicted ΔT_b's during the same time periods. Differences between ΔT_b's from both approaches exist between 1- 2 K in 10V, 19H, 19V, 37V and two weeks in 21V, where reasons are not understood. All other channels are consistent for both approaches with differences much less than 1 K. In these Figures, there are no common trends among variations of ΔT_b time series of different channel displayed. So, according to this sparse sampling of time periods of the year, no seasonal drift was found for the cross calibration between WindSat and TMI. Additional collocations, e.g. during a whole year, are needed for analysis of continuous time series variation of ΔT_b's to investigate the existence of higher frequency temporal dependencies.
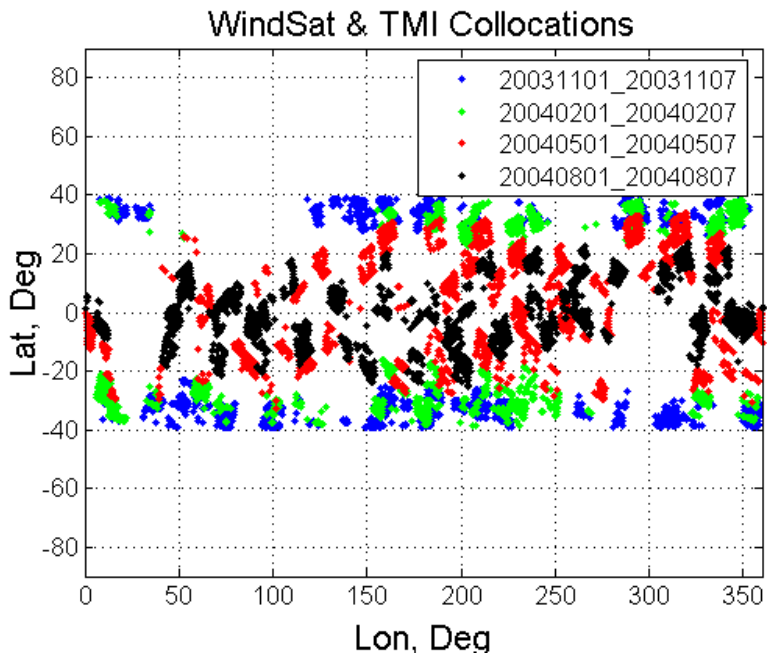
Figure 6.5: Geo-locations of WindSat and TMI Collocations (4 Weeks in Different Seasons).
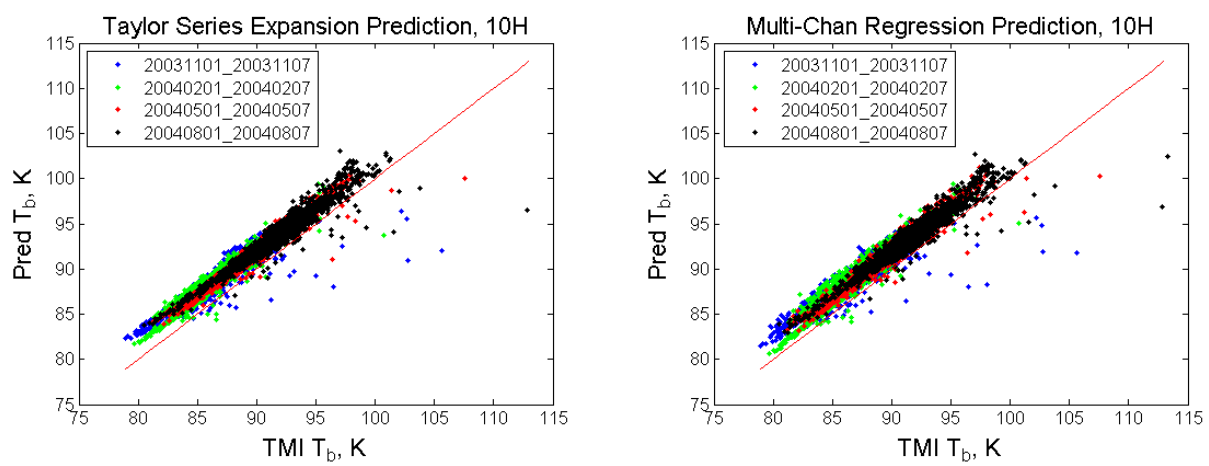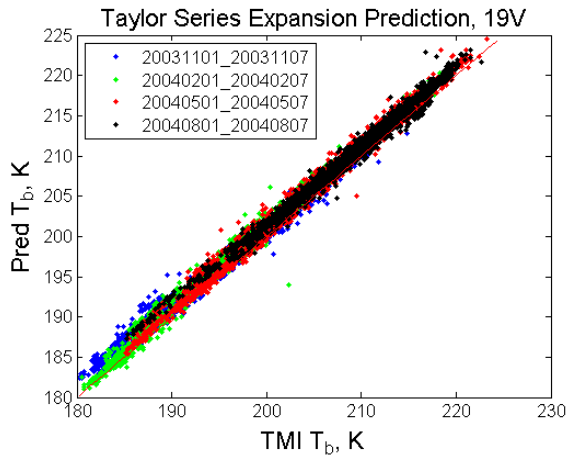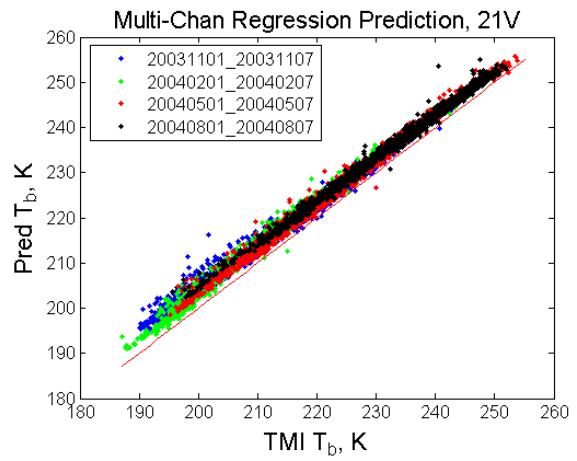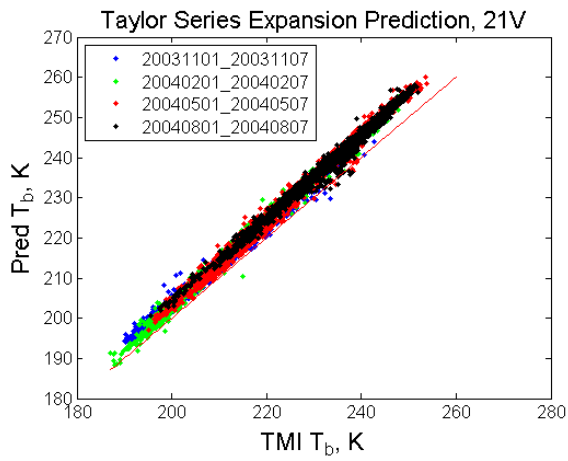

(a)   10.65 GHz, H-pol
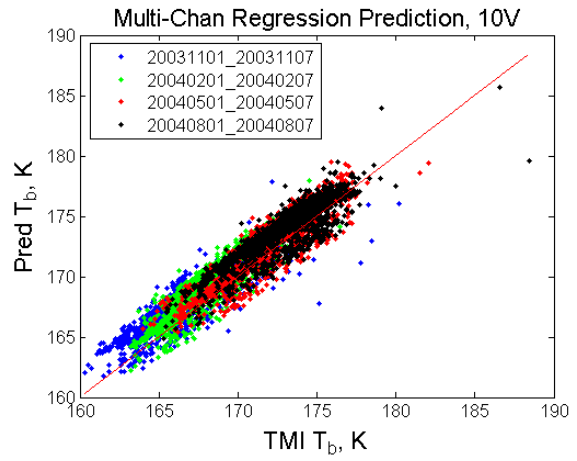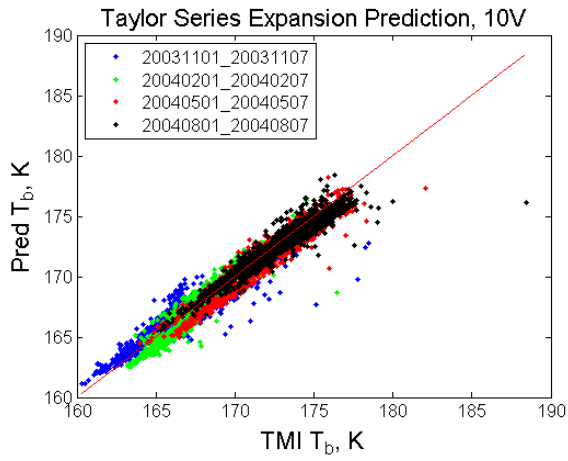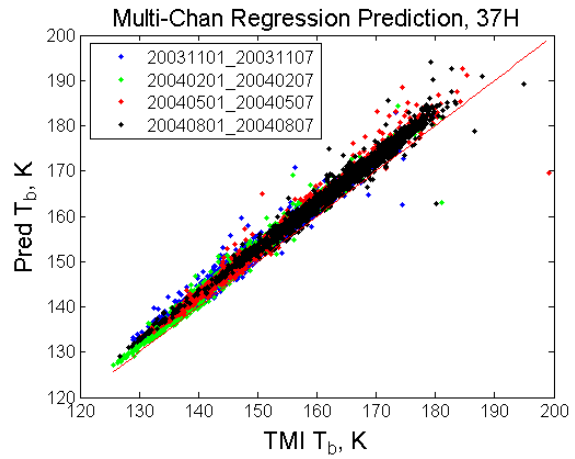
(b)   10.65 GHz, V-pol
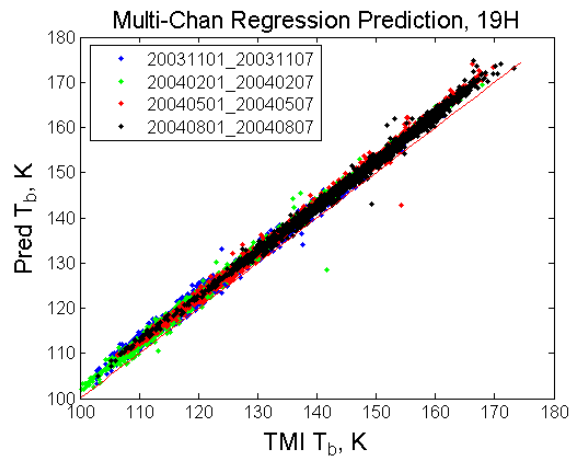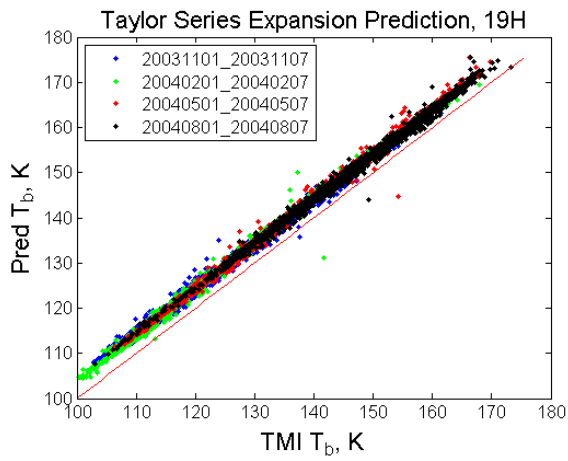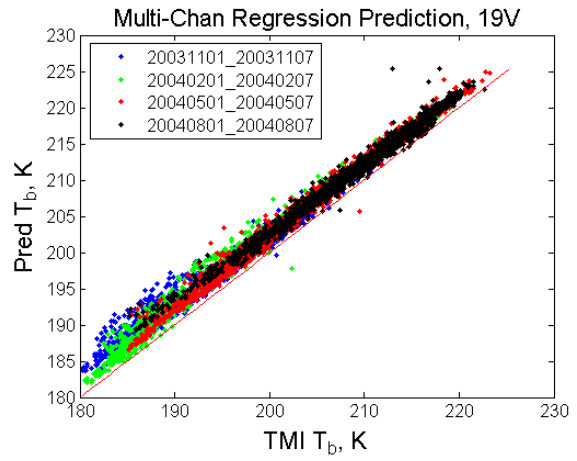
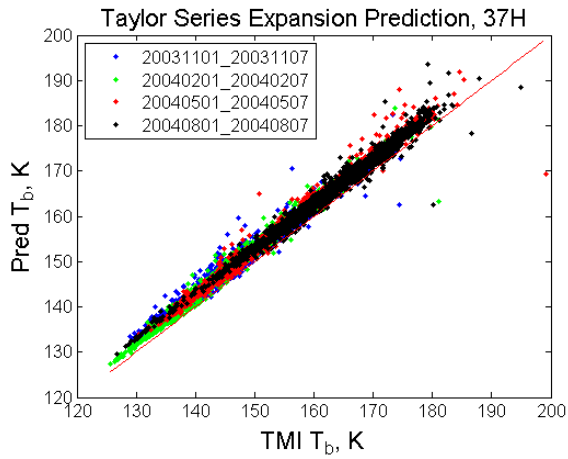
(c)   19.35 GHz, H-pol

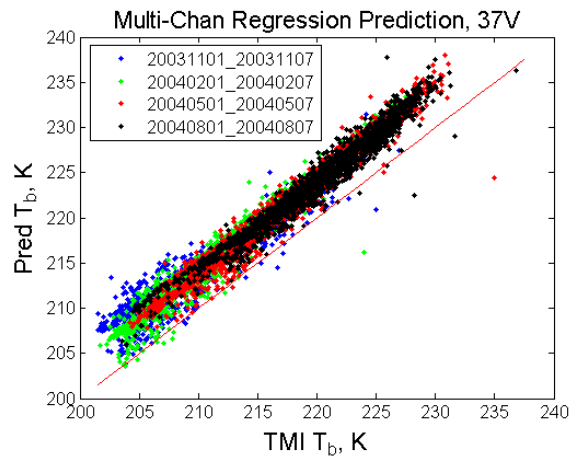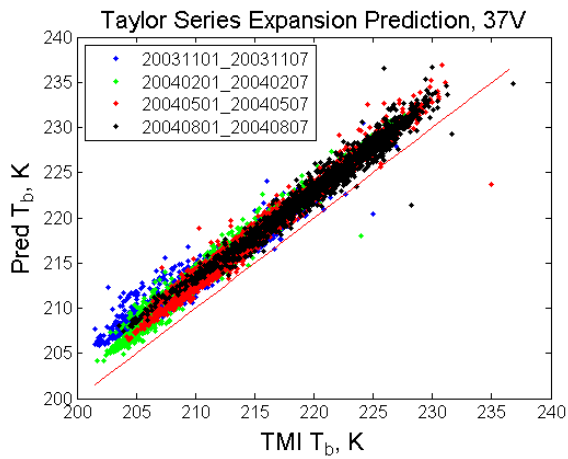(d)   19.35 GHz, V-pol

(e)   21.3 GHz, V-pol

(f)   37 GHz, H-pol

(g)   37 GHz, V-pol

Figure 6.6: TMI predictions (from WindSat) and collocated and simultaneous TMI

measurements (4 weeks in different seasons).

Table 6.3: Mean ΔT_b in WindSat to TMI Prediction by Taylor Series Expansion (4 Seasons)

Δ= Prediction -TMI	10H	10V	19H	19V	21V	37H	37V	# cases
11/01-11/07, 2003	2.32	0.09	4.34	1.26	3.50	2.87	3.26	1311
02/01-02/07, 2004	2.90	0.01	4.36	1.29	3.58	2.81	3.15	1155
05/01-05/07, 2004	2.01	-0.46	4.22	1.09	5.00	2.87	2.98	1451
08/01-08/07, 2004	1.95	-0.23	4.02	1.23	5.38	2.71	3.11	1791

Table 6.4: Mean ΔT_b in WindSat to TMI Prediction by Multi-Channel Regression (4 Seasons)
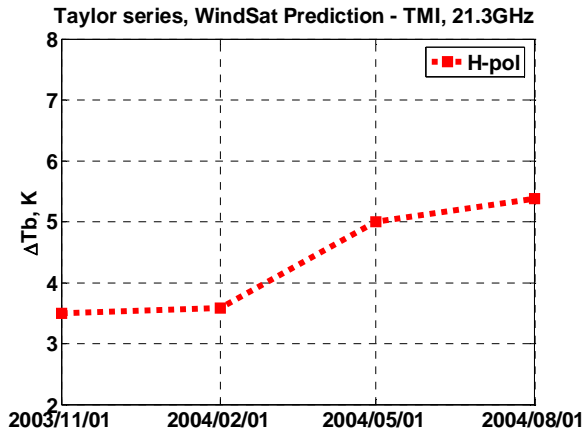
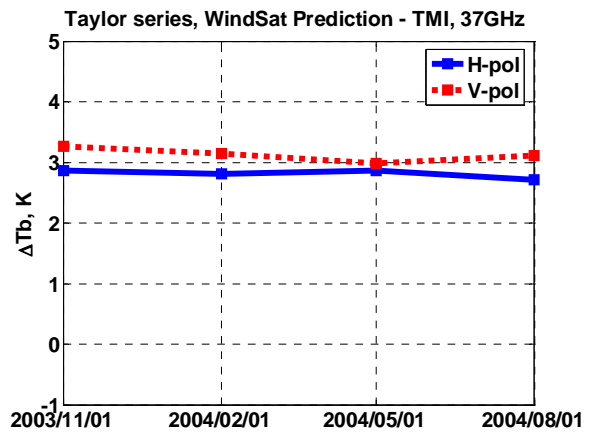| Δ= Prediction -TMI	10H	10V	19H	19V	21V	37H	37V	# cases
11/01-11/07, 2003	2.10	1.47	2.63	2.67	3.61	2.63	4.29	1311
02/01-02/07, 2004	2.12	1.30	2.73	2.64	3.28	2.69	4.25	1155
05/01-05/07, 2004	1.84	0.94	2.78	2.24	3.07	3.00	4.10	1451
08/01-08/07, 2004	1.78	1.28	2.68	2.31	3.10	2.90	4.21	1791
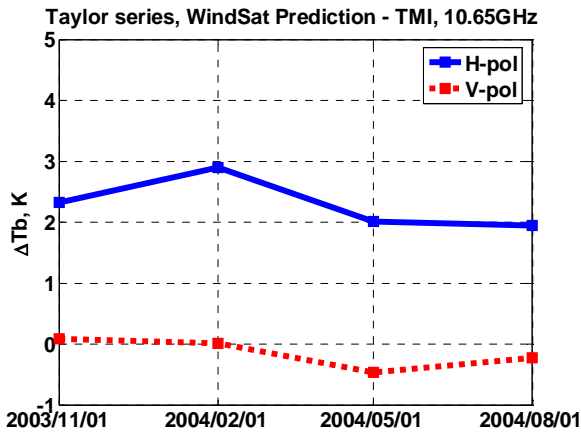
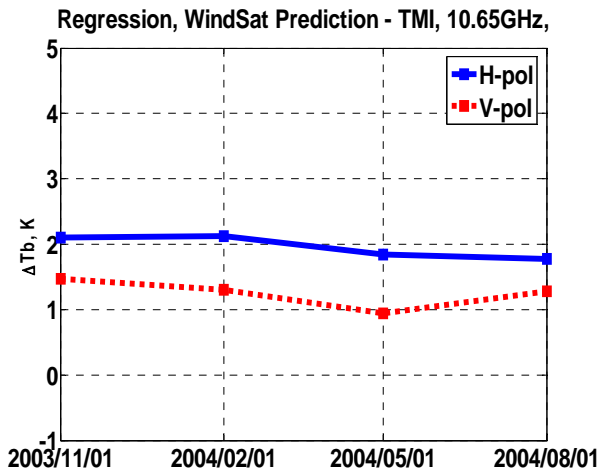(a)   10.65 GHz   (b)   19.35 GHz
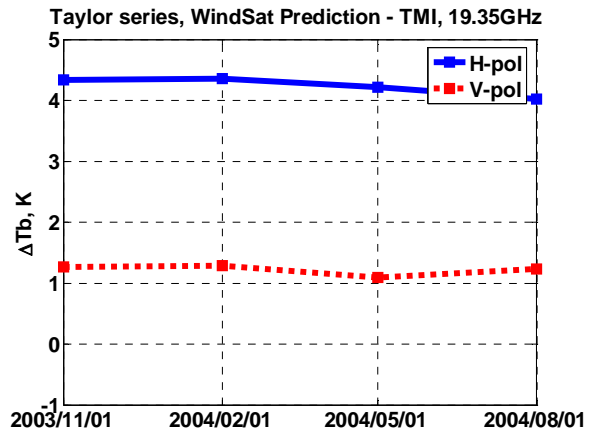
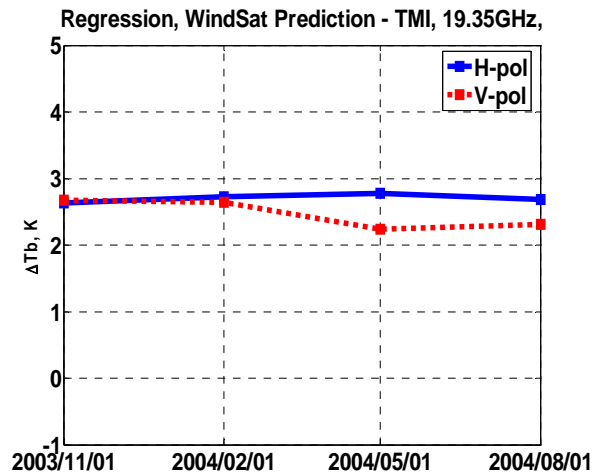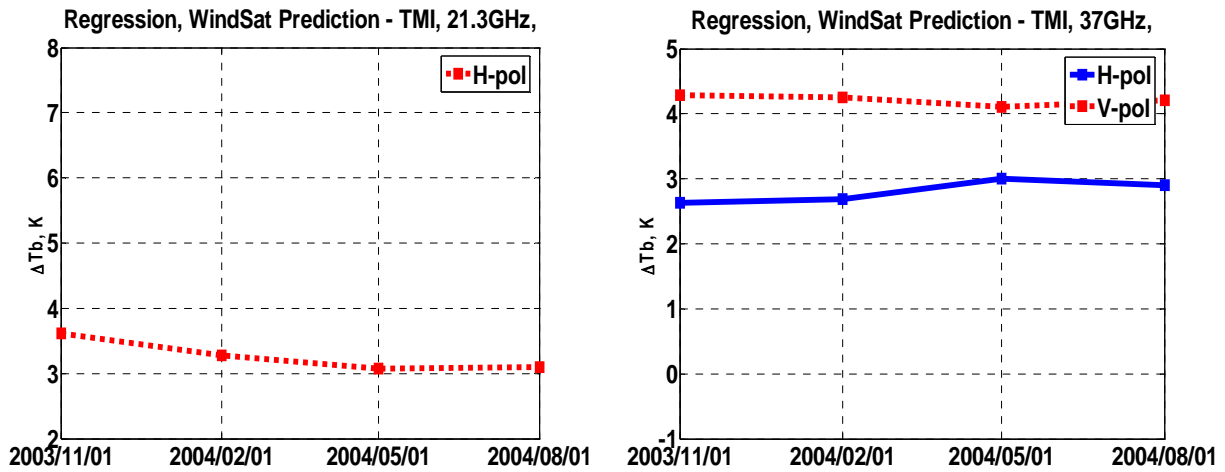(c)   21.3 GHz   (d)   37 GHz

Figure 6.7: WindSat to TMI Calibration during by Taylor Series Expansion Prediction (4 Weeks

in Different Seasons)

(a)   10.65 GHz   (b)   19.35 GHz

(c)   21.3 GHz   (d)   37 GHz

Figure 6.8: WindSat to TMI Calibration by Multi-Channel Regression Prediction (4 Weeks in

Different Seasons)

6.1.2 T_b Bias Spatial Variation

In order to investigate whether or not there are systematic T_b biases as a function of the satellite's orbital position, the geographic distributions of WindSat to TMI inter-calibration were analyzed. All collected collocations are bin averaged in an interval of 1 º latitude or longitude, and bins with less than 50 cases are discarded. For both calibration approaches, no pattern of functions between $\varDelta T_b$ and latitude is found. The $\varDelta T_b$ variations along latitude are less than 1 K for most channels (e.g. Figure 9 shows an example of 10.65 GHz) except for 21V in Taylor series expansion prediction, as seen in Figure 6.10. Correlations between V and H Pols are greater than 0.8 for most of the frequencies except for Multi-channel regression 19 GHz, which

is 0.5. Since the total fluctuation of ΔT_b along latitude is small compared to the ΔT_b absolute values, the correlation between V and H Pols may be statistically insignificant.

Because of land mask, collocations are not continuous along 1º-longitude bins. Also, geophysical conditions do not vary as much with longitude as with latitude. Analyses on ΔT_b's over longitude do not show any meaningful patterns.
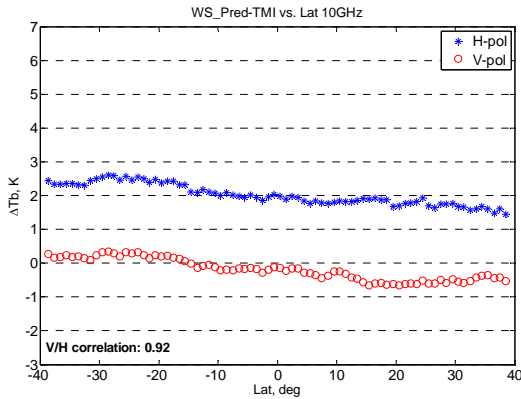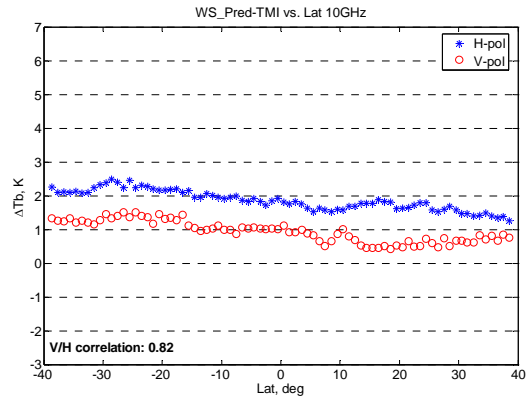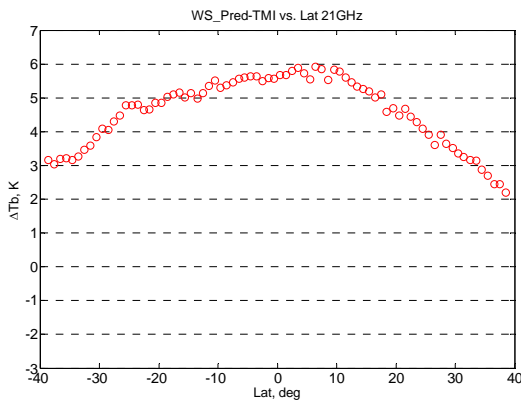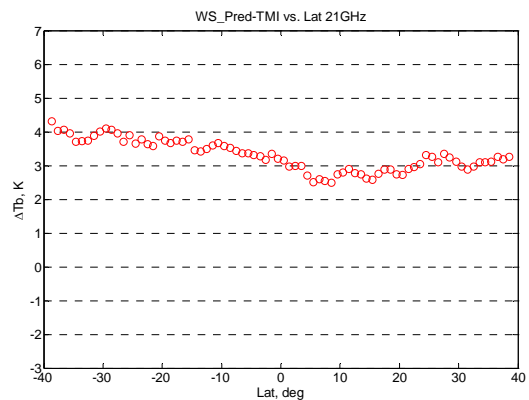

(a) Taylor series expansion　　　　　　　　(b) Multi-channel regression

Figure 6.9: WindSat to TMI Calibration vs. Latitude (10.65 GHz)

(a) Taylor series expansion　　　　　　　　(b) Multi-channel regression

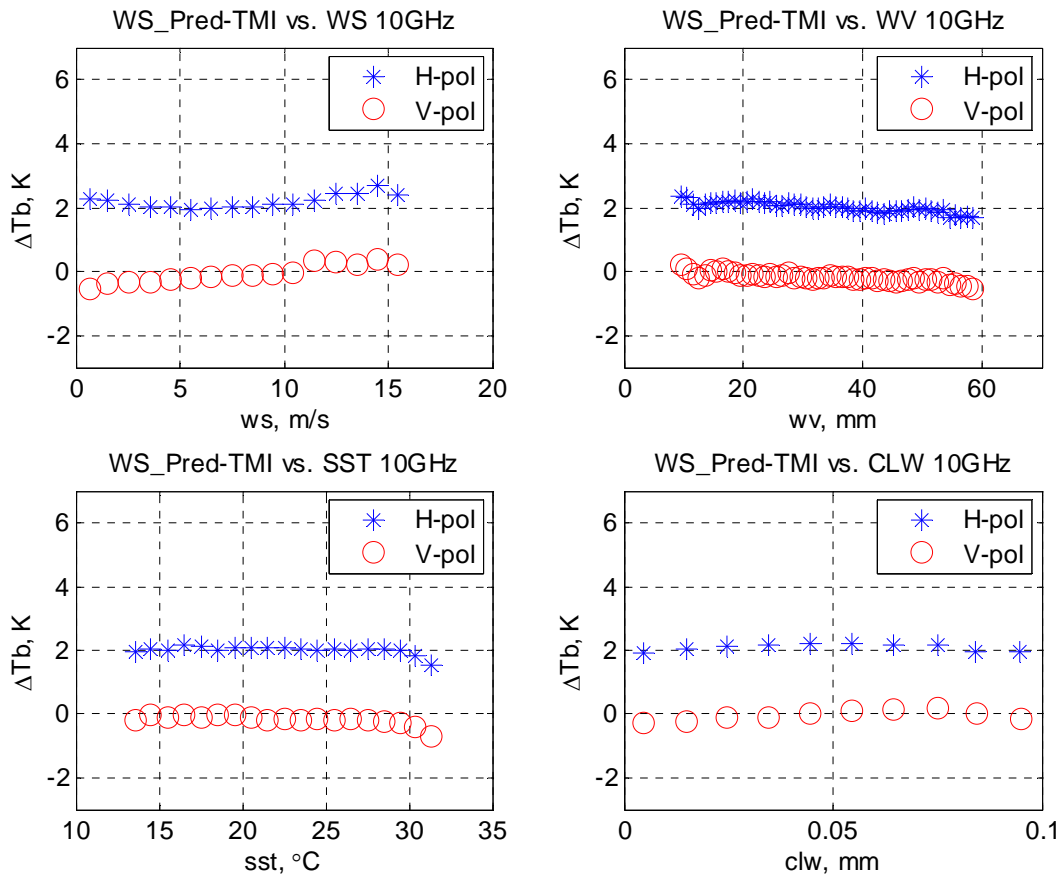Figure 6.10: WindSat to TMI Calibration vs. Latitude (21.3 GHz)

82

6.1.3 T_b Bias Geophysical Condition Dependence

With collocations during all collected time periods, ΔT_b variations against four major geophysical conditions are analyzed in both approaches. There are 14,865 cases in total for collocations between WindSat and TMI during all collected time periods. The ΔT_b equals to prediction from WindSat channel(s) minus simultaneously collocated TMI measurement. In these analyses, ΔT_b's are bin averaged against each geophysical parameter: wind speed values of all cases are binned with a 1 m/s interval in the range of 0 to 30 m/s; columnar water vapor values are binned with 1 mm interval in the range of 0 to 70 mm; sea surface temperature values are binned with 1 C interval in the range of 10 to 35 C; and columnar cloud liquid water values are binned with 0.01mm interval in the range of 0 to 0.1mm. Bins with less than 50 cases are discarded.
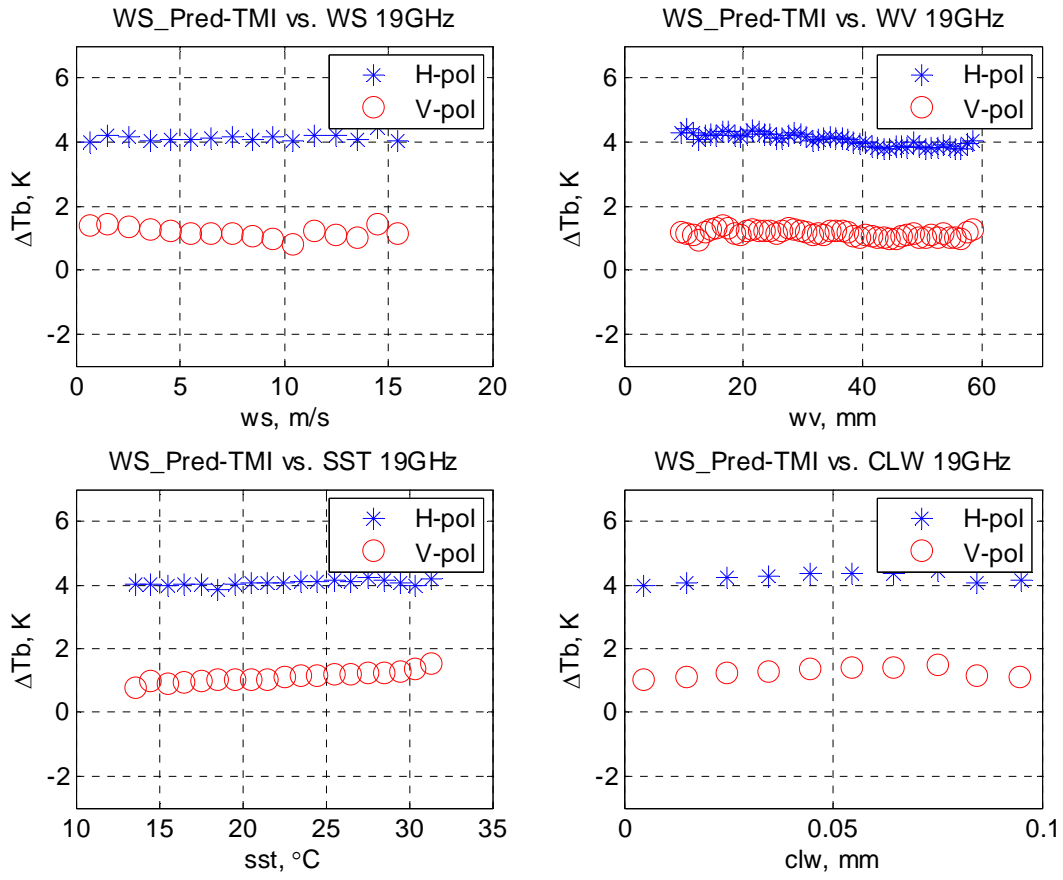
In both Taylor series expansion and multi-channel regression approaches, no pattern of ΔT_b as function of any geophysical parameters is discovered. Figures 6.11 and 6.12 show 10 GHz ΔT_b variations from both approaches, where standard deviations of ΔT_b's are within 1 K for most of the channels.

Exceptions occur in Taylor series expansion 21 GHz V-pol channel, where there are noticeable monotonically increasing slopes in both ΔT_b vs. WV and ΔT_b vs. SST plots for Taylor series expansion approach and monotonically decreasing slope in ΔT_b vs. WV for multi-channel regression approach. For both approaches, this is because of imperfect WV modeling in RadTb simulation of channels near 22.2 GHz, and for Taylor series expansion approach, 2nd order SST polynomial correction to the RadTb emissivity model is noisy near 22.2 GHz; TMI 21.3 V is

predicted by WindSat 23.8 V, these two frequencies lie on different sides of 22.235 GHz water vapor line.
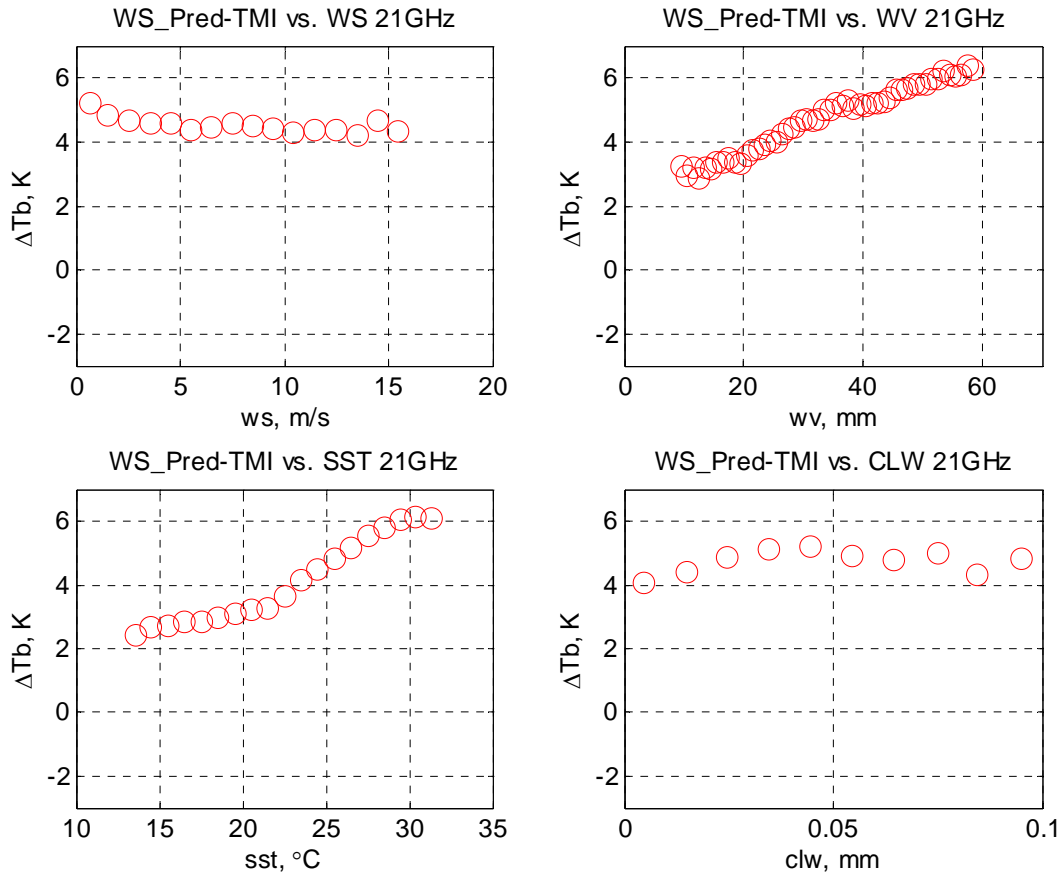

(a)   10.65 GHz

(b)   19.35 GHz

(c)   21.3 GHz

(d)   37 GHz

Figure 6.11: WindSat to TMI Calibration (Taylor Series Expansion) vs. Geophysical Conditions
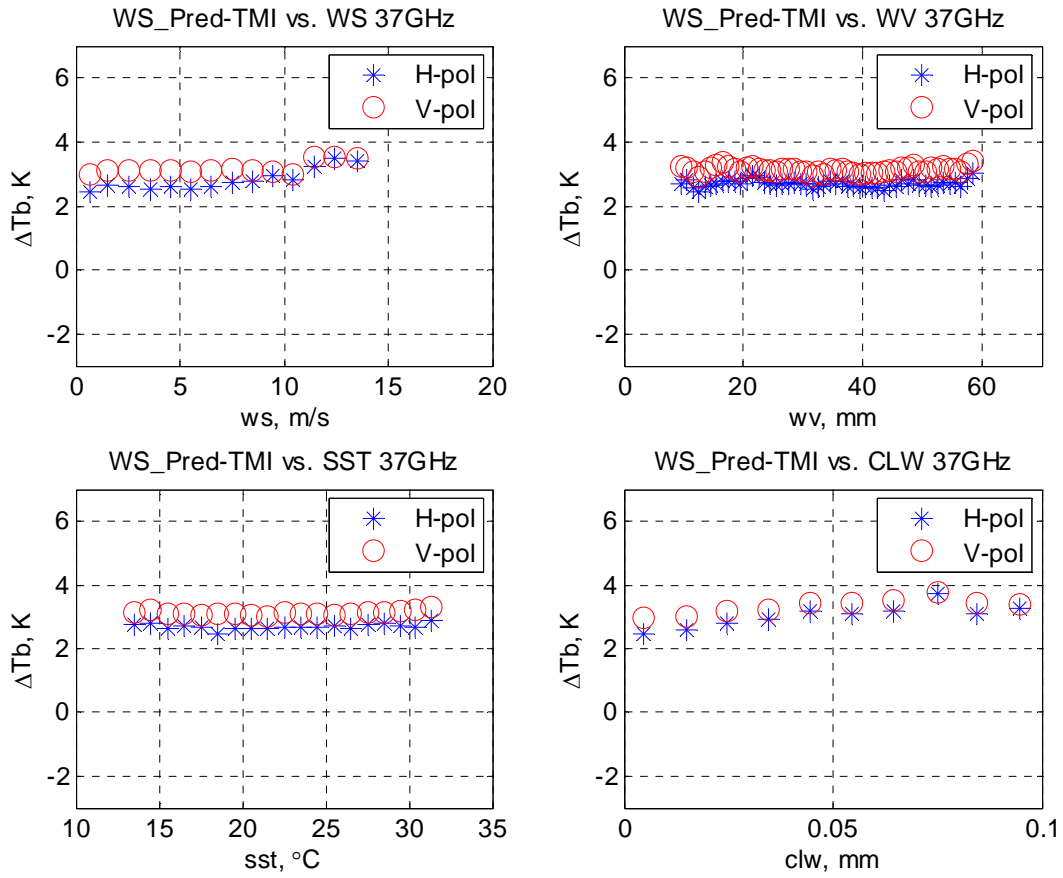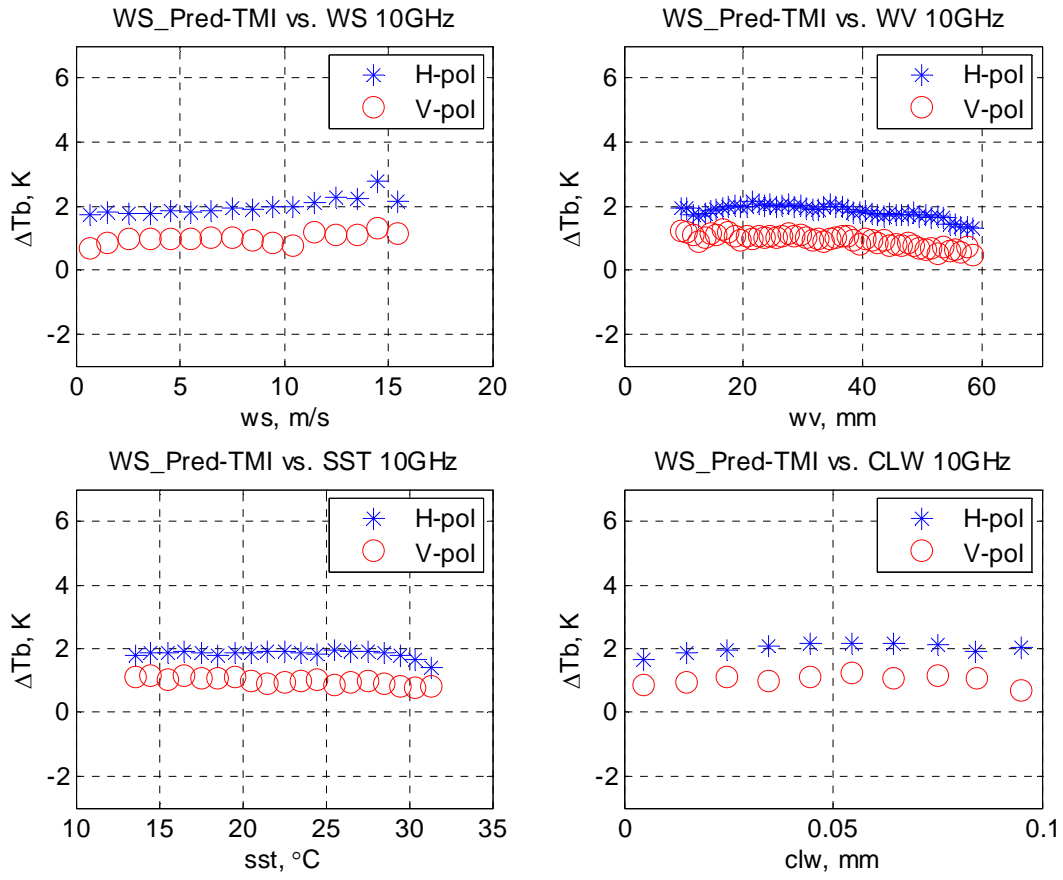
(a)   10.65 GHz
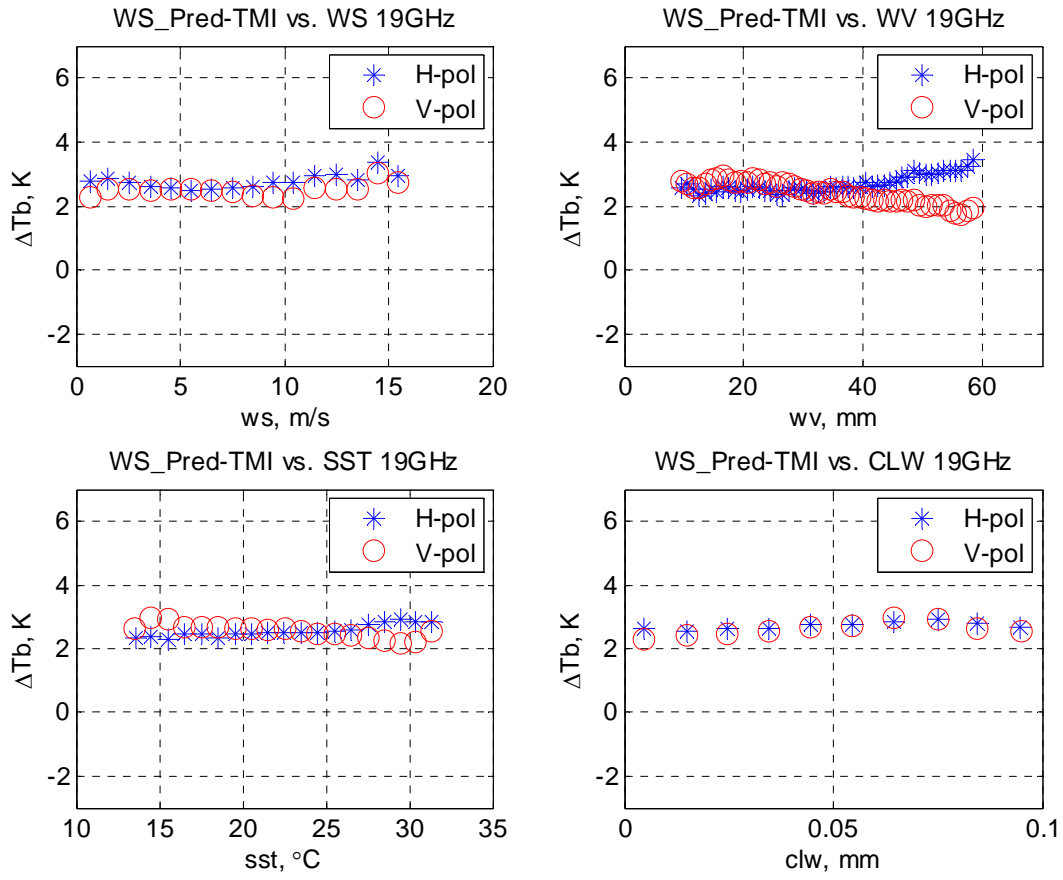
(b)   19.35 GHz
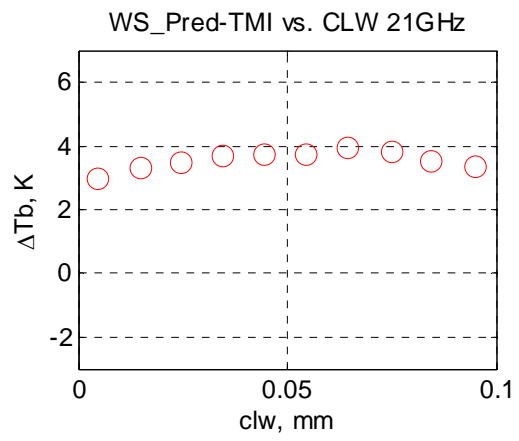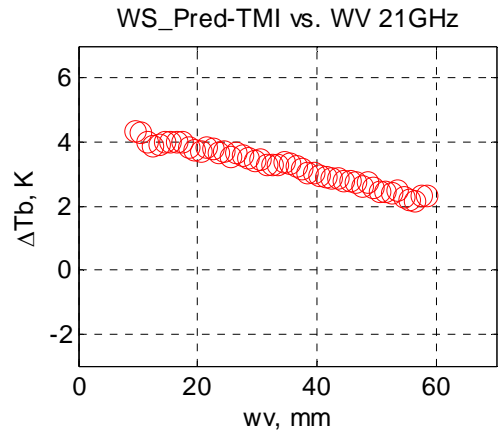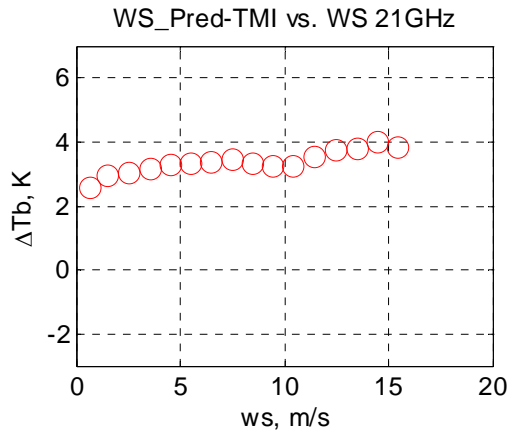
(c)   21.3 GHz
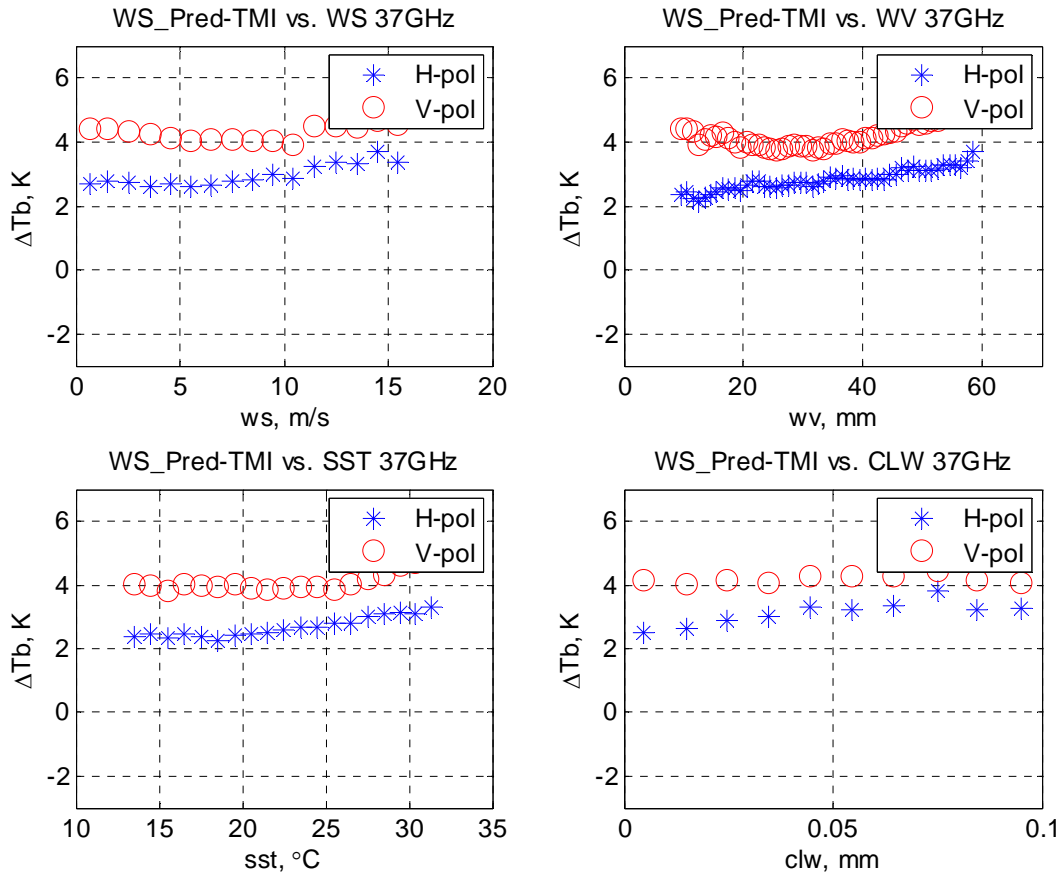
(d)　37 GHz

Figure 6.12: WindSat to TMI Calibration (Multi-Channel Regression) vs. Geophysical

Conditions

6.1.4　Tb Bias in Two Approaches with All Collocations

For all the collected collocations (14,865 cases) between WindSat and TMI, the standard deviations of the biases between predictions and measurements are at the same level (~1 K) for both approaches.

Also, for both approaches, the biases for most of TMI channels are unexpectedly large. Our temporal and spatial tolerances for collocations between WindSat and TMI are strict enough to prevent fluctuations in geophysical conditions that could 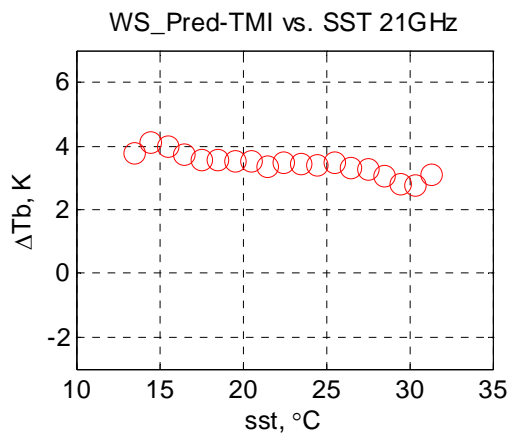cause large variations in T_b. These notable biases agree with comparison between WindSat and TMI 37 GHz channel measurements from a few pairs of randomly selected collocations between these two radiometers.

Using all collocations between WindSat and TMI, calibrations results were derived as shown in Table 6.5 by applying both approaches. A subset of collocations under limited geophysical condition where WS $\leq$ 8m/s, WV $\leq$ 40mm and CLW $\leq$ 0.1mm, as shown in Table 6.6, presented very similar results (mean and std) to Table 6.5. Differences of mean values are smaller than 0.2 except for mean value of 21V channel, where the difference is up to 0.6 K. And Figure 6.13 shows scatter plots of calibration results from both approaches. Except for 19.35 GHz and 21.3 GHz channels, where scatter plots are a bit noisy, scatter plots of all other channels align or parallel with the 45 degree line.

Table 6.5: ΔT_b in WindSat to TMI Prediction by Taylor Series Expansion for All Cases

14865 Cases in Total

Δ= Prediction -TMI		10H	10V	19H	19V	21V	37H	37V
Taylor Series	mean	1.93	-0.26	4.09	1.11	4.65	2.58	3.02
Expansion	std	0.78	0.80	0.85	0.88	1.71	1.07	0.88
Multi-Channel	mean	1.78	1.18	2.59	2.30	3.18	2.69	4.14
Regression	std	0.84	0.84	0.93	0.91	1.12	1.08	1.10

Table 6.6: ΔT_b in WindSat to TMI Prediction by Taylor Series Expansion for Limited Cases

where WS ≤ 8m/s, WV ≤ 40mm and CLW ≤ 0.1mm, 7702 Cases in Total

Δ= Prediction -TMI		10H	10V	19H	19V	21V	37H	37V
Taylor Series	mean	1.95	-0.26	4.18	1.17	4.07	2.53	2.99
Expansion	std	0.79	0.81	0.82	0.89	1.62	1.03	0.89
Multi-Channel	mean	1.81	1.23	2.43	2.48	3.46	2.51	3.98
Regression	std	0.86	0.85	0.90	0.93	1.06	1.03	1.03
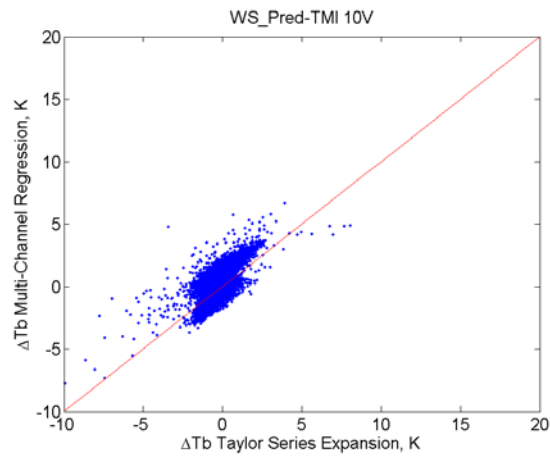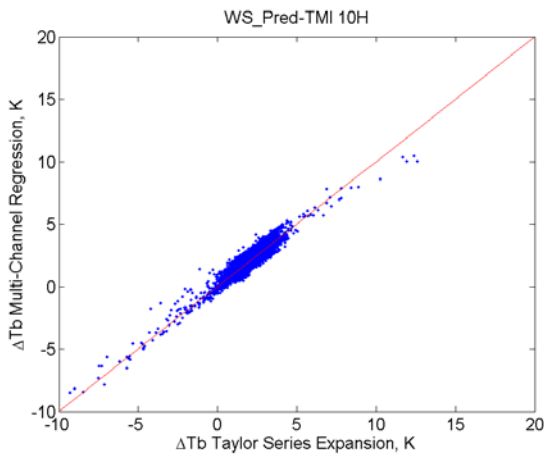
(a)   10.65 GHz
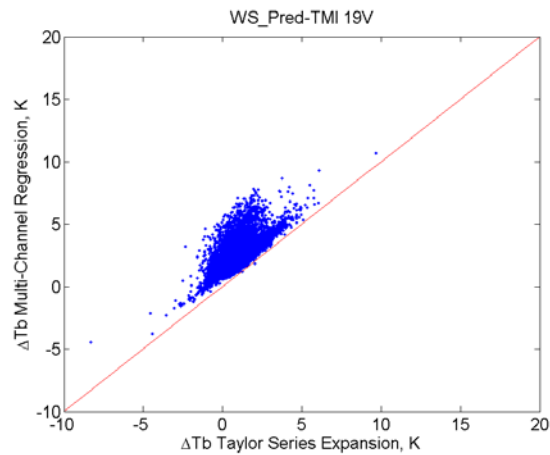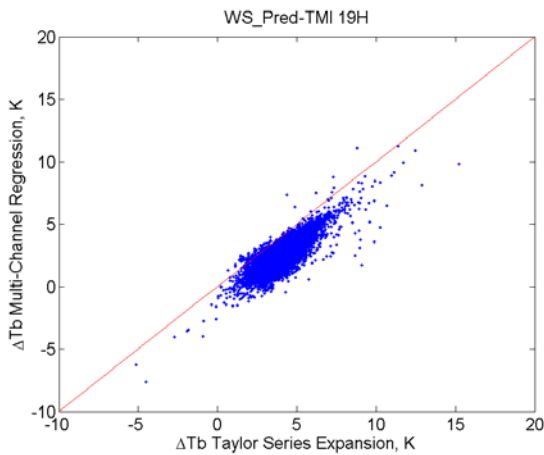
(b)   19.35 GHz
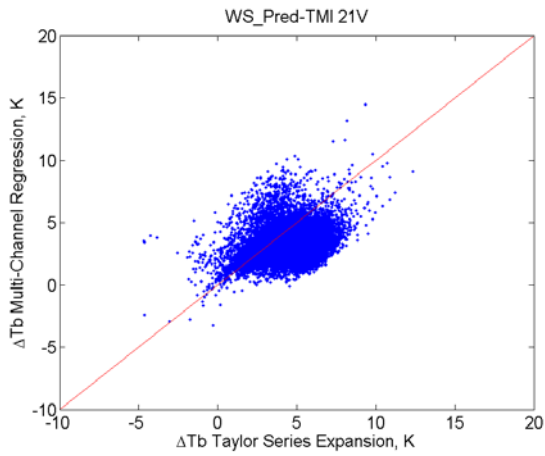
(c)   21.3 GHz
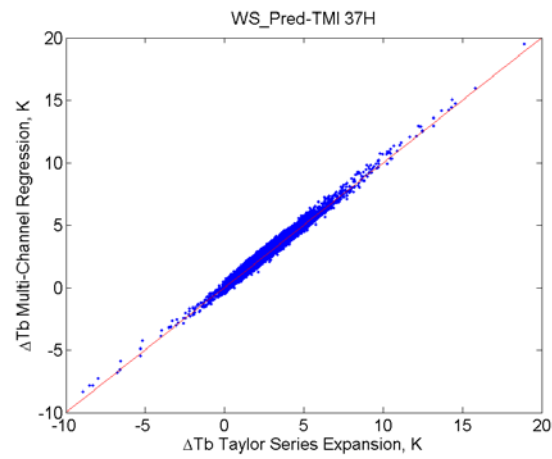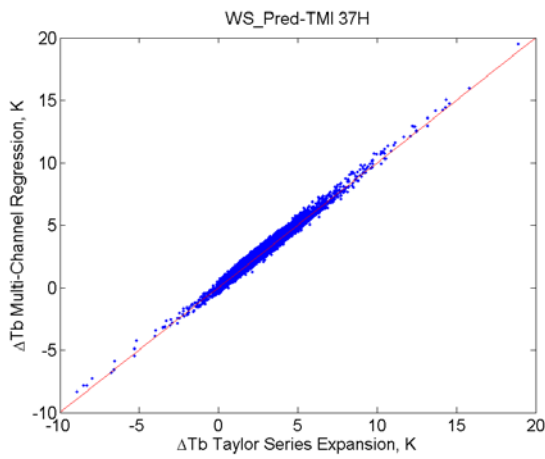
(d)   37 GHz

Figure 6.13: Scatter Plot of WindSat to TMI Calibration T_b biases in Both Approaches

6.2   TMI and AMSR

6.2.1   Tb Bias Temporal Variation

During June 1 to June 30 of 2003, both collocations between WindSat and TMI and those between TMI and AMSR were analyzed. Same data averaging and filtering processes, as used in WindSat to TMI calibration, were applied except that AMSR ascending and descending paths were separately analyzed. The statistics of differences between predictions from TMI channels and AMSR channels by Taylor series expansion are shown in Table 6.7. And the results from multi-channel regression prediction are show in Table 6.8. In both approaches, the predicted brightness temperatures are smaller than the measurements. For most of the AMSR channels on the descending orbital segments, most biases between predictions and measurements are slightly larger than those on ascending segments. There are no clear patterns of discrepancies between ascending and descending paths except for the 37H channel. All standard deviations of biases are less than 2K.

Table 6.7: ΔT_b in TMI to AMSR Prediction by Taylor Series Expansion during 1 Month

Δ= Prediction - TMI		6H	6V	10H	10V	18H	18V	23H	23V	37H	37V	# cases
Asc	mean	-1.25	-1.03	-1.04	-0.63	-2.92	-1.41	-3.37	-5.87	-1.66	-1.25	4149
	std	0.53	0.56	0.54	0.37	0.71	0.44	1.14	1.61	0.88	0.53	
Dsc	mean	-1.77	-0.34	-1.78	-0.86	-3.21	-1.48	-4.39	-4.92	-4.37	-1.77	6634
	std	1.02	0.59	0.87	0.47	0.77	0.61	1.72	1.94	0.65	1.02	
Asc + Dsc	mean	-1.45	-0.59	-1.37	-0.75	-3.08	-1.44	-3.87	-5.23	-3.64	-1.45	10783
	std	0.82	0.69	0.80	0.44	0.76	0.53	1.55	1.94	1.73	0.82	

Table 6.8: ΔT_b in TMI to AMSR Prediction by Multi-Channel Regression during 1 Month

Δ= Prediction - TMI		6H	6V	10H	10V	18H	18V	23H	23V	37H	37V	# cases
Asc	mean	-0.67	-0.36	-2.68	-2.92	-1.68	-1.36	-2.83	-1.74	-1.88	-2.62	4149
	std	0.57	0.56	0.53	0.38	0.66	0.44	0.80	0.60	0.87	0.57	
Dsc	mean	-1.31	0.27	-3.33	-3.11	-2.22	-1.49	-3.39	-1.66	-4.57	-3.31	6634
	std	0.75	0.80	1.05	0.56	0.71	0.56	0.91	0.75	0.74	0.67	
Asc + Dsc	mean	-1.01	-0.04	-2.91	-3.01	-1.99	-1.43	-3.15	-1.69	-3.78	-3.01	10783
	std	0.79	0.80	0.83	0.49	0.76	0.51	0.91	0.69	1.79	0.73	

Another set of data is collected in 7 consecutive months in 2003 from April to October (1 week's collocation between TMI and AMSR are collected in each month), and the geographic distribution of the collocations is shown in Figure 6.14. According to results in Tables 6.9 and 6.10, with a data sampling rate of one week per month, the T_b biases fluctuate at a range of up to 1K during the 7 weeks. In both calibration approaches, for all the channels, the trend of fluctuations of H-pol shows an opposite pattern as that of V-pol. Scatter plots of prediction vs. measurement during the selected 7 weeks with both approaches is shown in Figure 6.15.
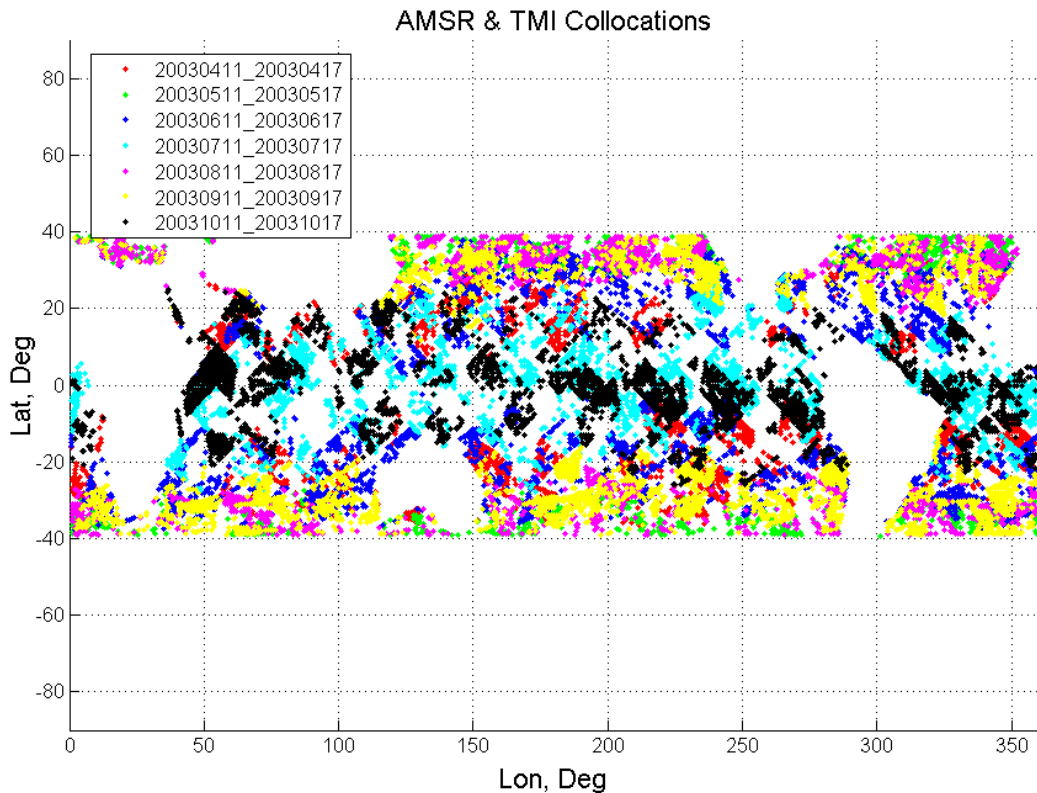
Figure 6.14: Geo-locations of TMI and AMSR Collocations during One Week Each in 7

Consecutive Months

Table 6.9: Mean ΔT_b (TMI to AMSR) by Taylor Series Expansion during 7 Months

in 2003

| Δ= Prediction - TMI	6H	6V	10H	10V	18H	18V	23H	23V	37H	37V	# cases
04/11 - 04/17	-1.27	-0.47	-1.12	-0.65	-3.01	-1.47	-3.70	-5.55	-3.14	-4.22	2045
05/11 - 05/17	-1.80	0.16	-1.94	-0.33	-3.25	-1.03	-5.34	-3.10	-3.77	-4.23	1441
06/11 - 06/17	-1.13	-0.91	-0.95	-0.78	-2.82	-1.56	-3.23	-5.34	-3.02	-4.47	2689
07/11 - 07/17	-1.48	-0.24	-1.27	-0.26	-2.63	-0.85	-3.68	-5.60	-2.90	-3.76	2310
08/11 - 08/17	-1.88	0.03	-1.77	-0.18	-3.03	-0.81	-4.43	-4.32	-3.41	-4.00	1913
09/11 - 09/17	-1.10	-0.44	-1.04	-0.78	-2.82	-1.52	-3.54	-4.19	-3.36	-4.40	2593
10/11 - 10/17	-1.62	-0.57	-1.37	-0.47	-2.94	-1.15	-4.20	-5.80	-3.31	-1.62	2699

Table 6.10: Mean ΔT_b (TMI to AMSR) by Multi-Channel Regression during 7 Months

in 2003

Δ= Prediction - TMI	6H	6V	10H	10V	18H	18V	23H	23V	37H	37V	# cases
04/11 - 04/17	-0.59	0.37	-2.70	-2.90	-1.78	-1.57	-2.55	-1.61	-3.30	-3.06	2045
05/11 - 05/17	-1.71	0.26	-3.39	-2.41	-2.31	-1.09	-3.47	-1.42	-3.74	-2.38	1441
06/11 - 06/17	-0.63	-0.27	-2.60	-3.08	-1.55	-1.48	-2.93	-1.86	-3.22	-3.28	2689
07/11 - 07/17	-0.68	0.71	-3.05	-2.69	-1.73	-0.79	-2.62	-0.82	-3.22	-2.33	2310
08/11 - 08/17	-1.32	0.65	-3.39	-2.35	-2.02	-0.92	-2.58	-1.13	-3.57	-2.34	1913
09/11 - 09/17	-0.67	-0.18	-2.62	-3.01	-1.69	-1.48	-3.09	-2.01	-3.41	-3.06	2593
10/11 - 10/17	-0.99	0.21	-3.09	-2.83	-2.08	-1.27	-2.51	-1.18	-3.51	-2.63	2699
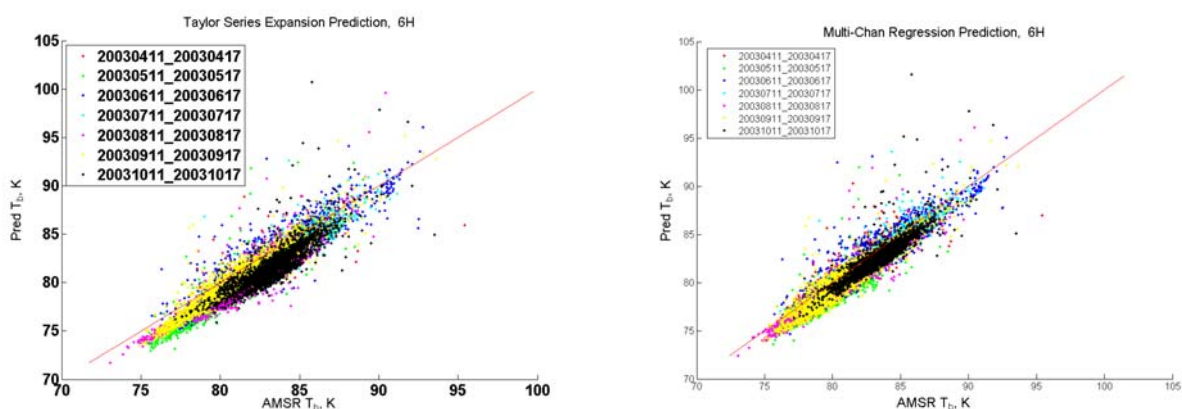
(a)   6.925 GHz, H-pol
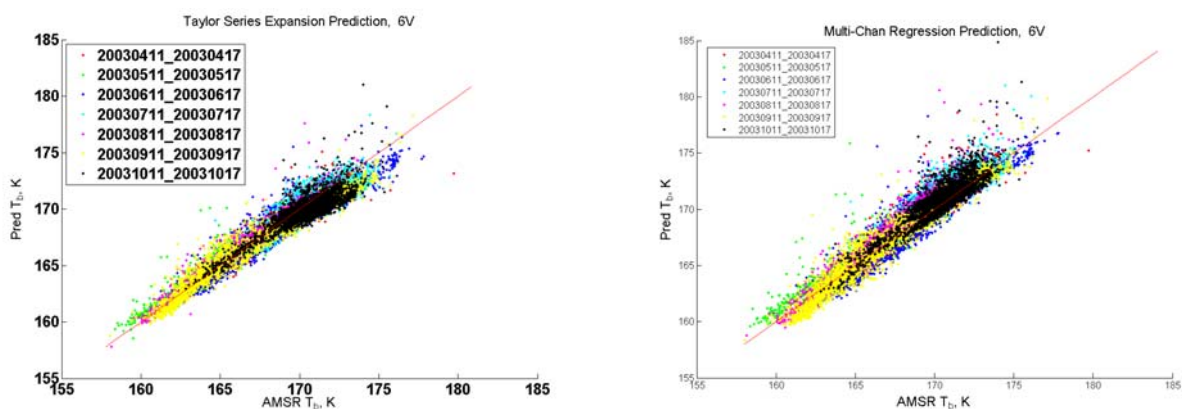
(b)   6.925 GHz, V-pol
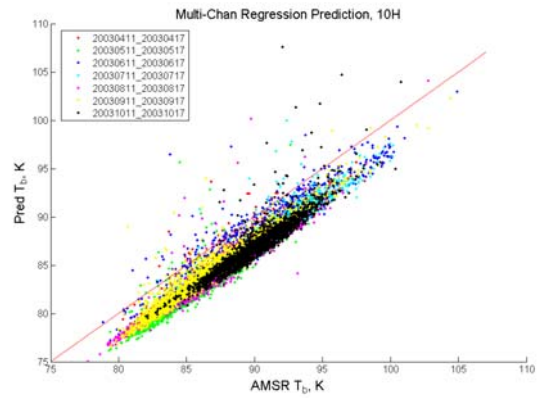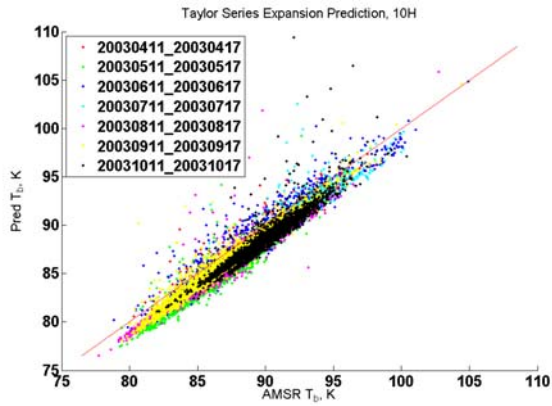
(c)   10.7 GHz, H-pol
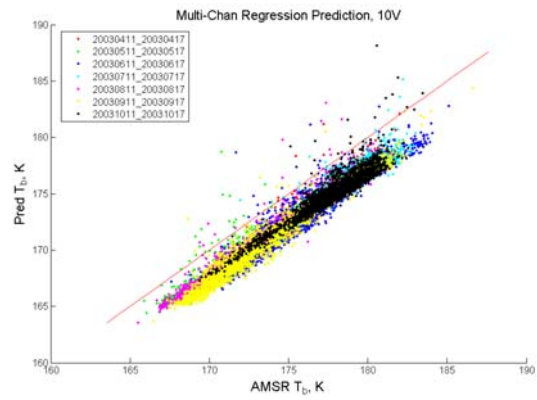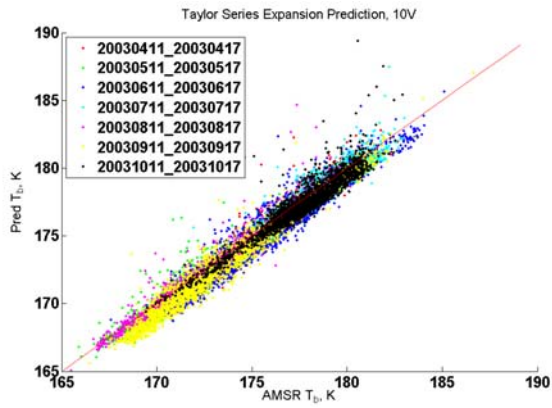
(d)   10.7 GHz, V-pol
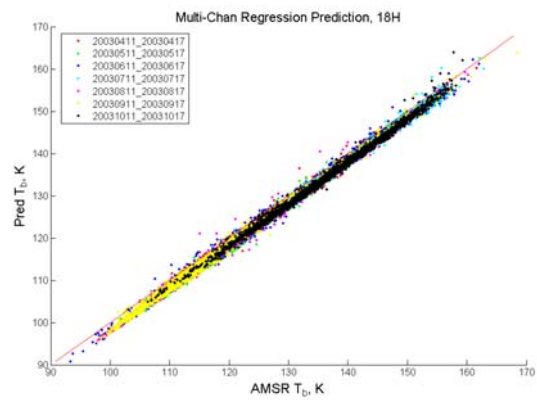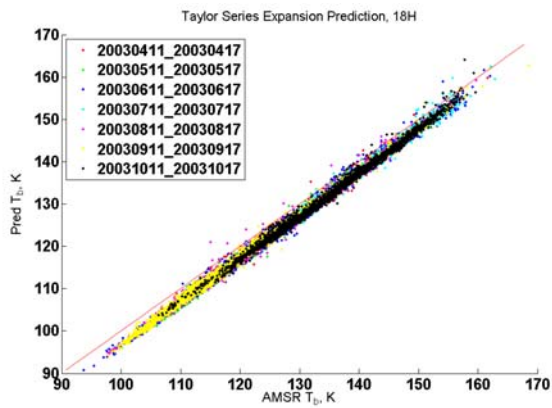
(e)   18.7 GHz, H-pol
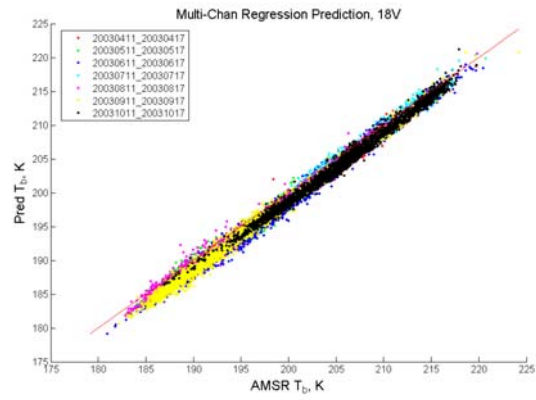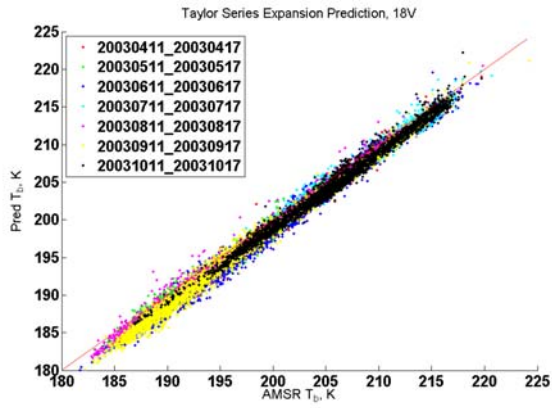
(f)   18.7 GHz, V-pol
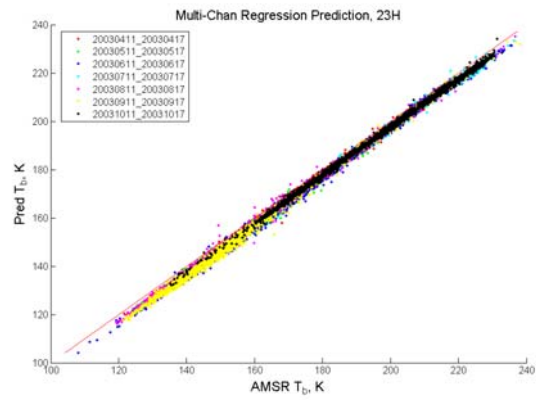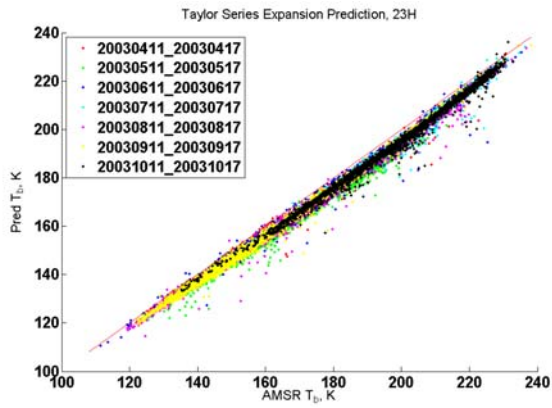
(g)   23.8 GHz, H-pol
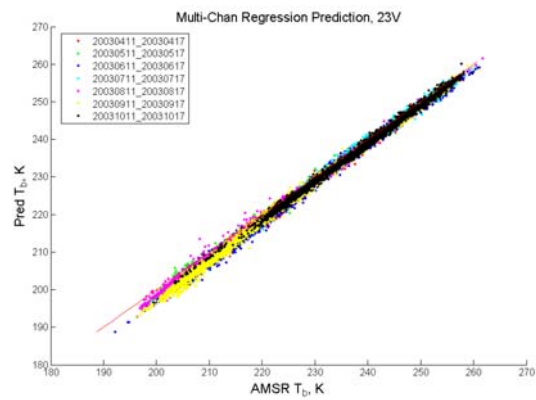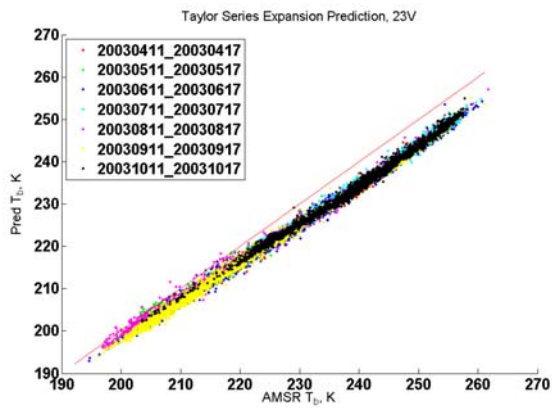
(h)   23.8 GHz, V-pol
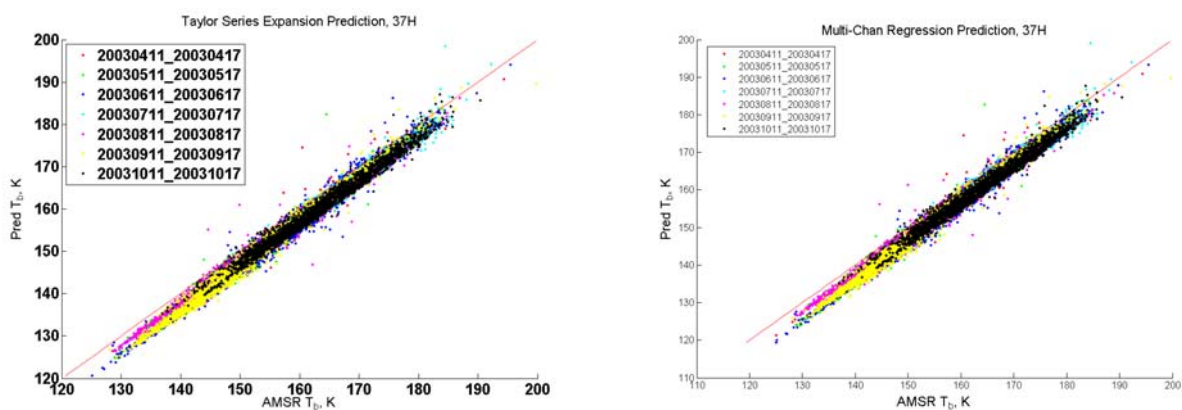
(i)   36.5 GHz, H-pol
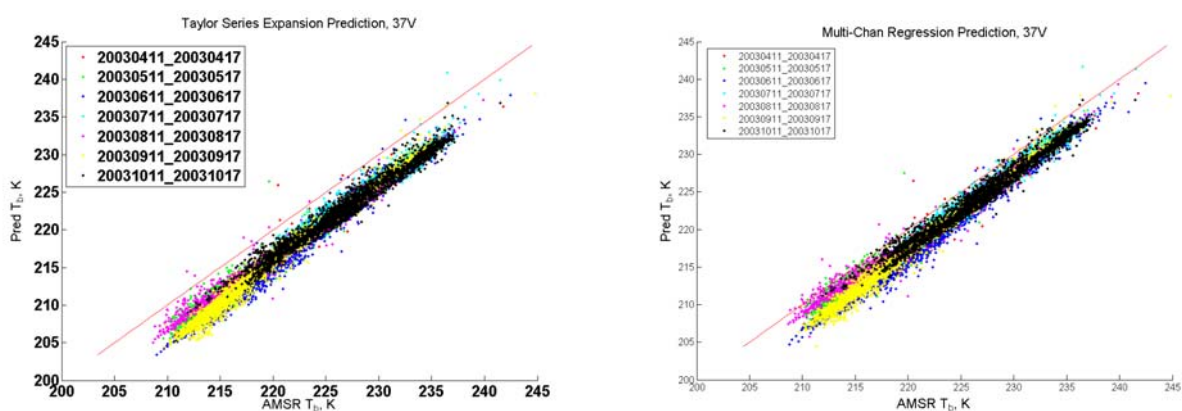
(j)   36.5 GHz, V-pol

Figure 6.15: Scatter Plot of TMI Predictions vs. AMSR Measurements during One Week Each in

7 Consecutive Months

Figures 6.16 and 6.17 show how T_b biases in TMI to AMSR calibration varies with the month of year in 2003. For both calibration approaches, V and H-pols appear to be anti-correlated to some extent, especially in 10 GHz channels. In order to further investigate the fluctuation functions for both V and H polarizations, continuous collection of collocations over a long time period, e.g. 1 year, is recommended.
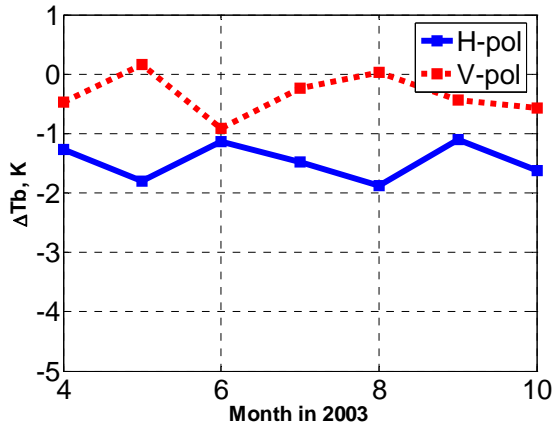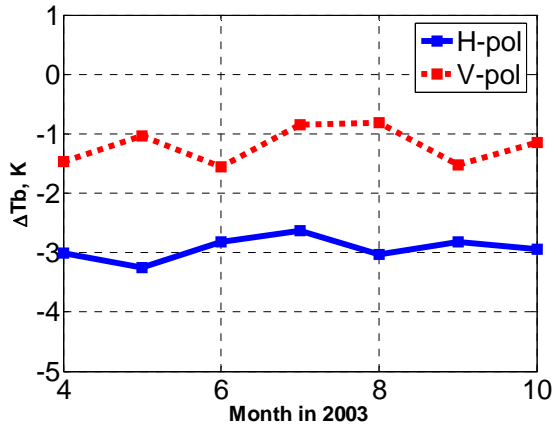
(a)   6.925 GHz

(b)   10.65 GHz

(c)   18.7 GHz
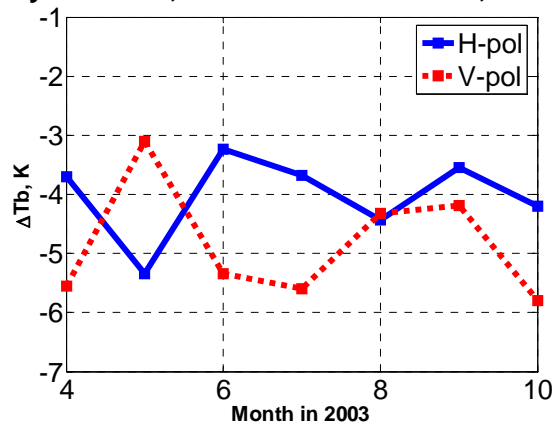
(d)   23.8 GHz
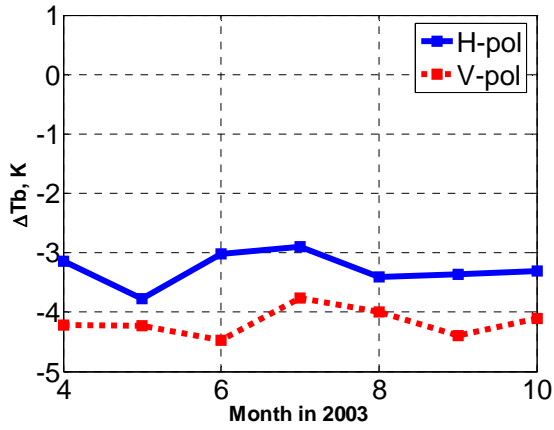
(e)   36.5 GHz

Figure 6.16: TMI to AMSR Calibration by Taylor Series Expansion Prediction in 7 Months

(a)   6.925 GHz

(b)   10.65 GHz

(c)   18.7 GHz

(d)   23.8 GHz
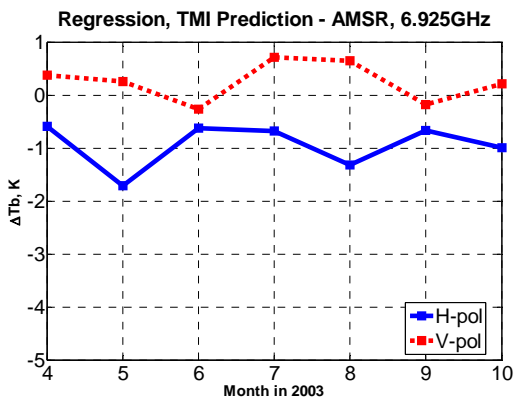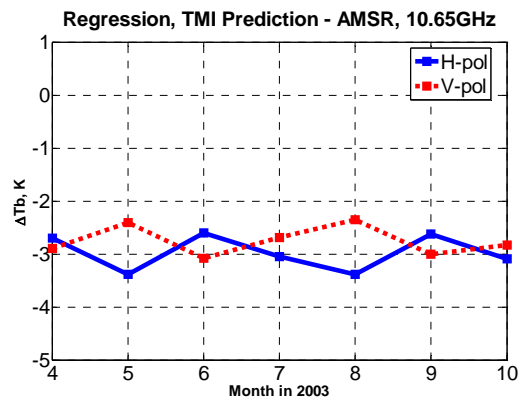
(e)   36.5 GHz
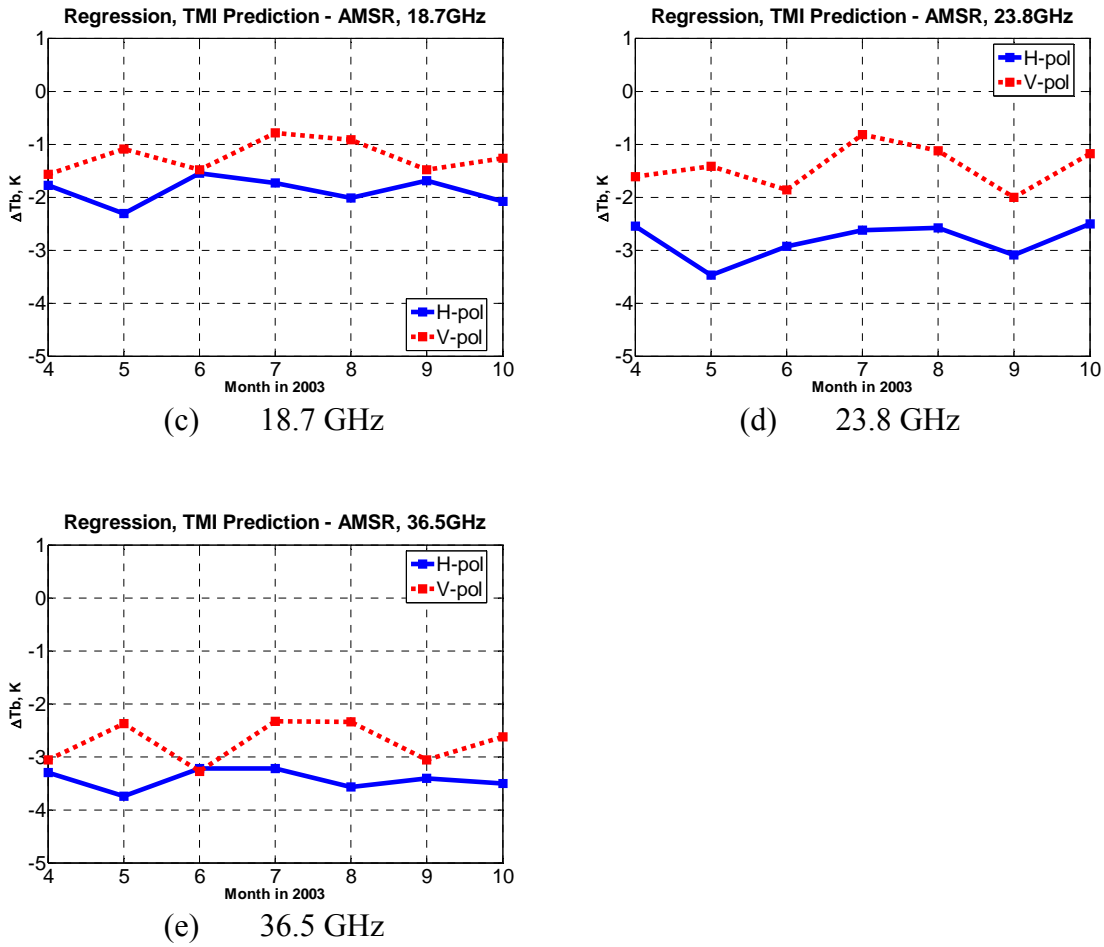
Figure 6.17: TMI to AMSR Calibration by Multi-Channel Regression Prediction in 7 Months

6.2.2   Tb Bias Spatial Variation

To investigate the possibility of T_b bias spatial dependence, the same procedures are performed to TMI and AMSR calibration results as were done for WindSat to TMI. An example of ΔT_b vs. latitude (10.7 GHz) is shown in Figure 6.18. For both calibration approaches, there is no apparent functional dependence between ΔT_b and latitude. For most channels, fluctuations of $\Delta T_b's$ are less than 1 K, and there are smaller correlations between V and H polarizations than

those exhibited for WindSat to TMI results. In the Taylor series expansion, there are larger fluctuations in 23.8 GHz channels, as shown in Figure 6.19, which is probably caused by imperfect WV modeling, noisy 2nd order SST polynomial adjustment to sea surface emissivities and the latitude dependence of WV and SST values.
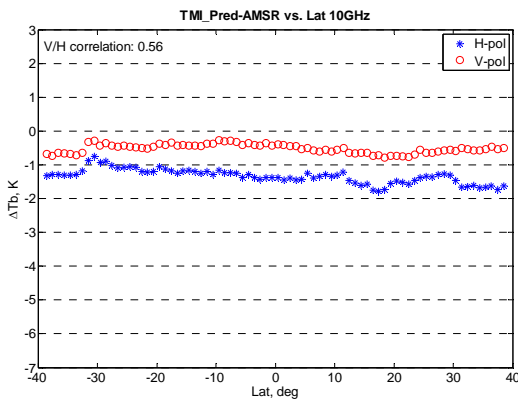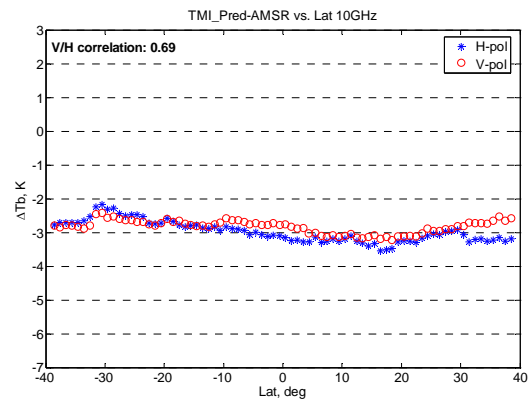
(a) Taylor series expansion　　　　　　(b) Multi-channel regression

Figure 6.18: TMI to AMSR Calibration vs. Latitude (10.7 GHz)
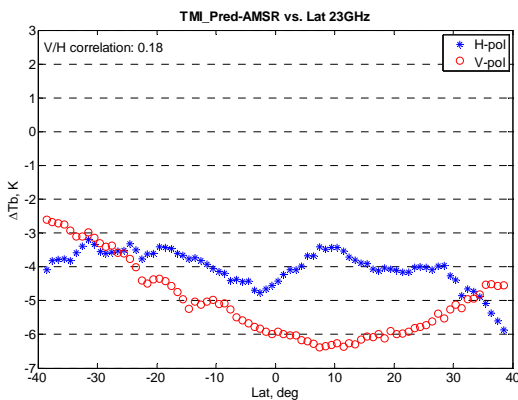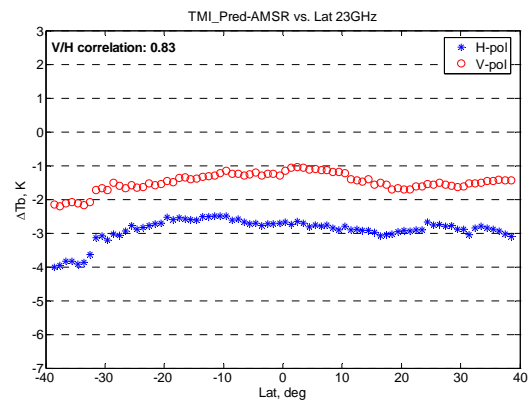
(a) Taylor series expansion　　　　　　(b) Multi-channel regression

Figure 6.19: TMI to AMSR Calibration vs. Latitude (23.8 GHz)

6.2.3 Tb Bias Geophysical Parameter Dependence

Identical procedures, as in WindSat to TMI calibration results, are performed to analyze ΔT_b variations against four major geophysical parameters with TMI and AMSR calibration results from all collected collocations (23,784 cases in total). The ΔT_b equals the prediction from TMI channel(s) minus simultaneously collocated AMSR measurement.

In both Taylor series expansion and multi-channel regression approaches, no pattern of ΔT_b dependence as function of any geophysical parameters is found, and figures 6.20 and 6.21 show ΔT_b variations from both approaches, where the standard deviations of ΔT_b's are within 1K for most of the channels.
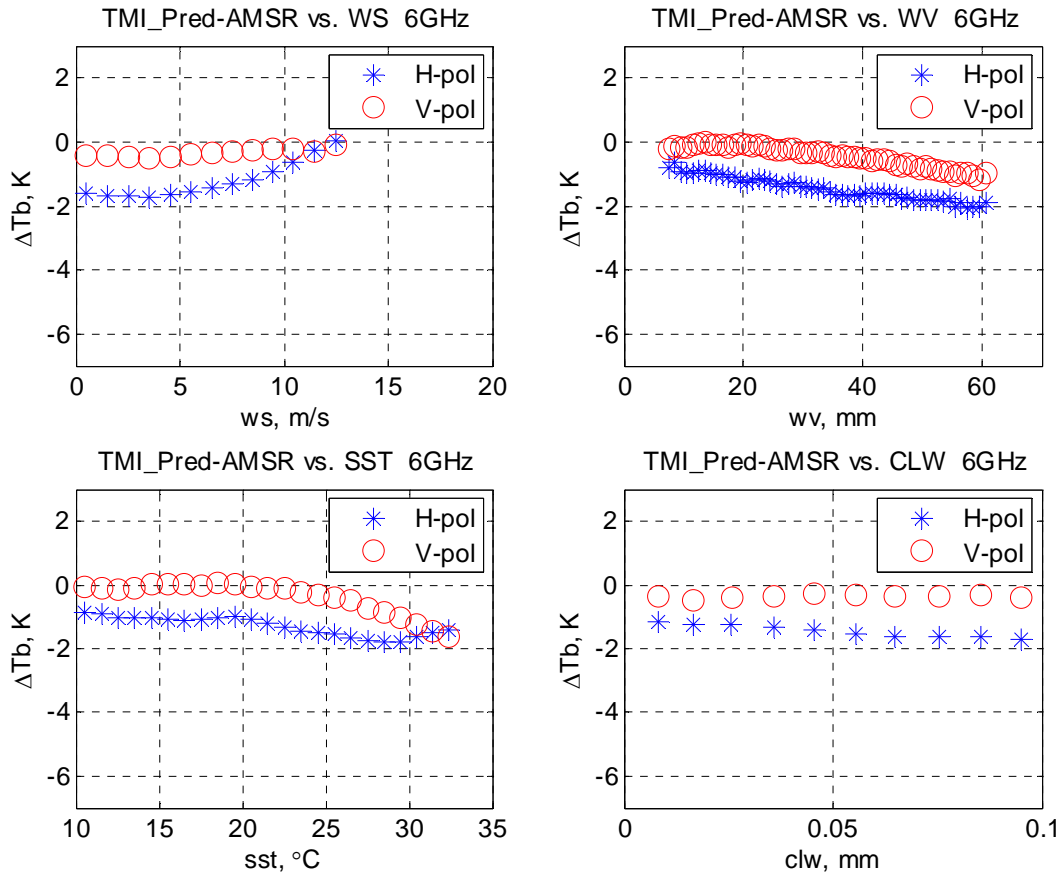
(a)   6.925 GHz
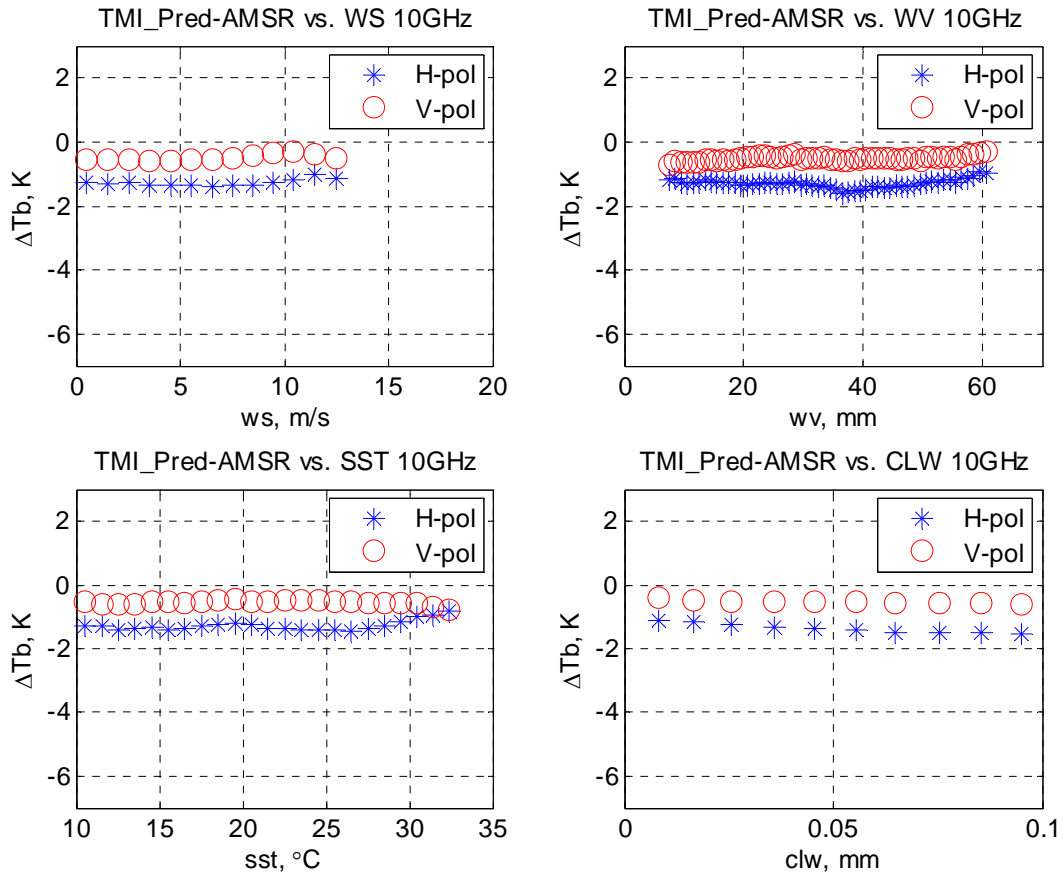
(b)   10.65 GHz
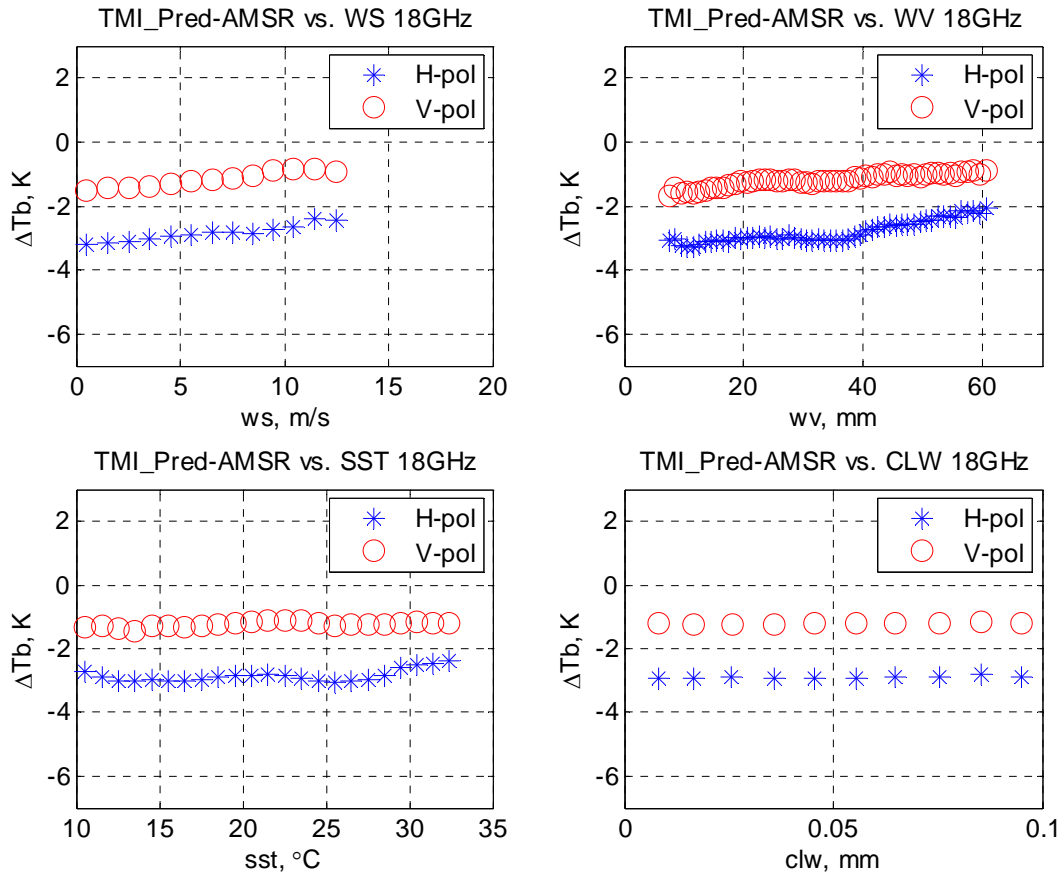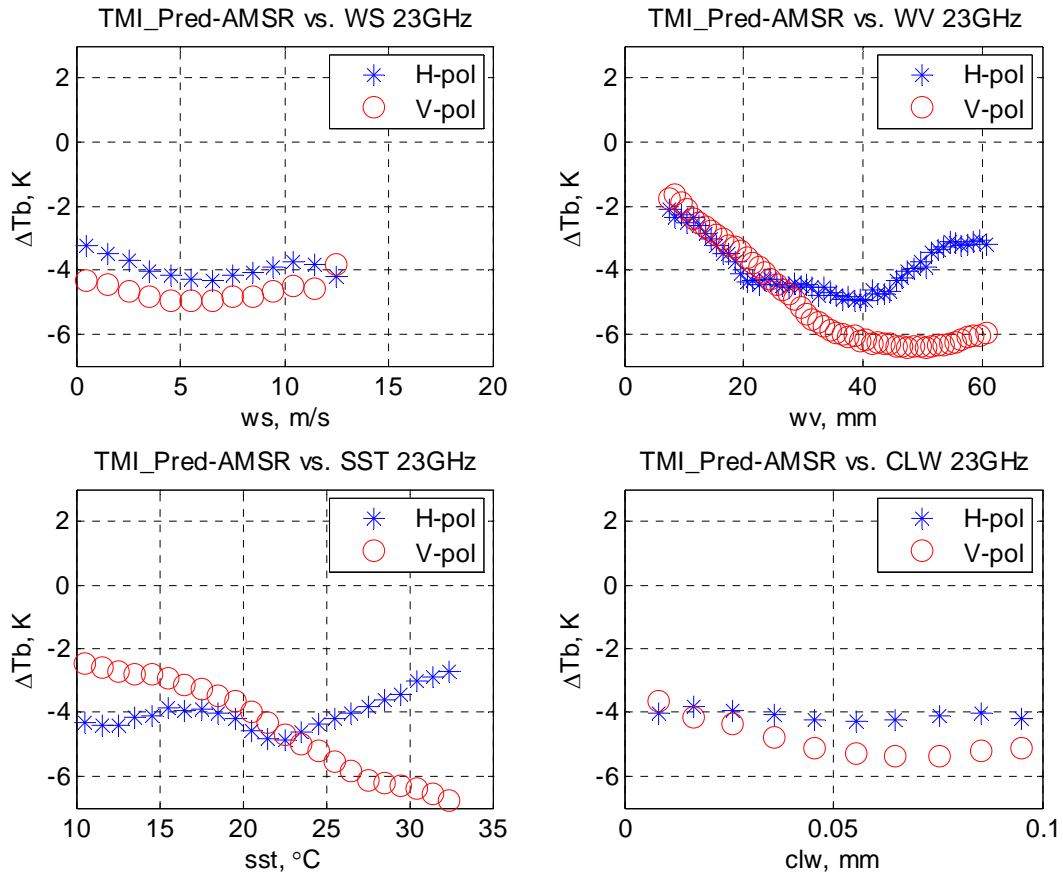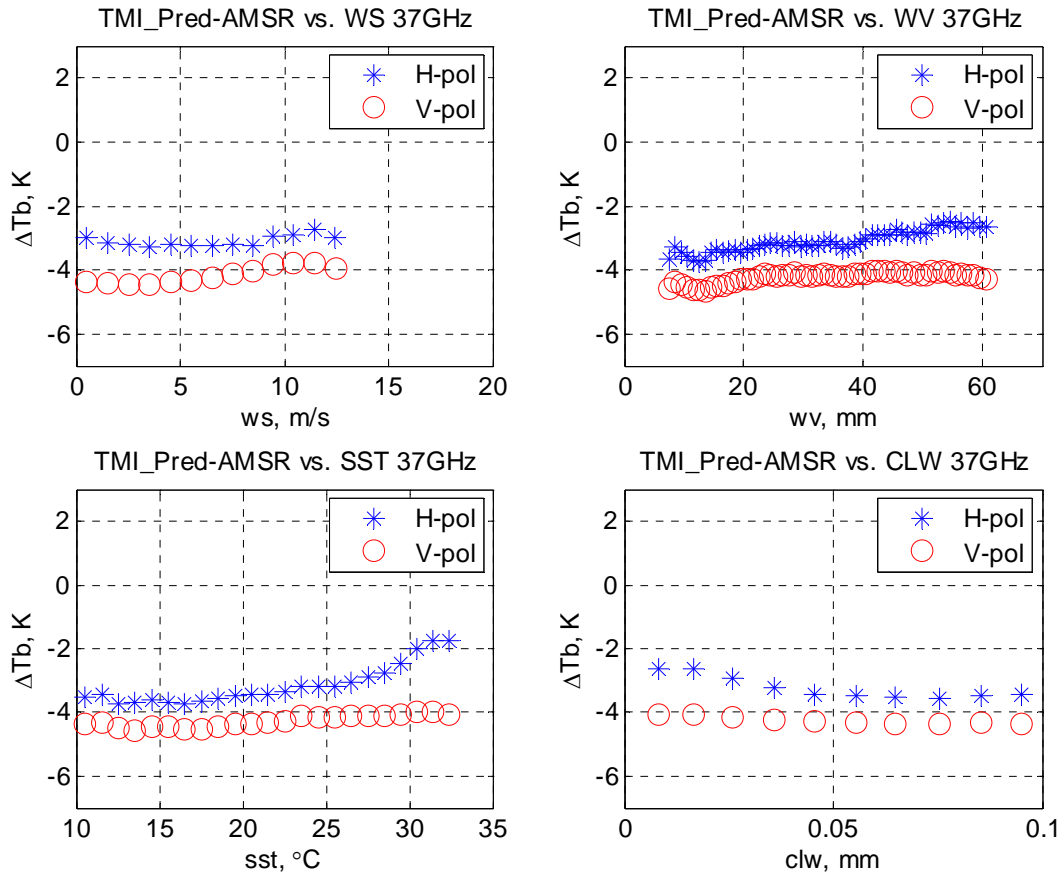
(c)   18.7 GHz

(d)   23.8 GHz

(e)   36.5 GHz

Figure 6.20: TMI to AMSR Calibration (Taylor Series Expansion) vs. Geophysical Conditions
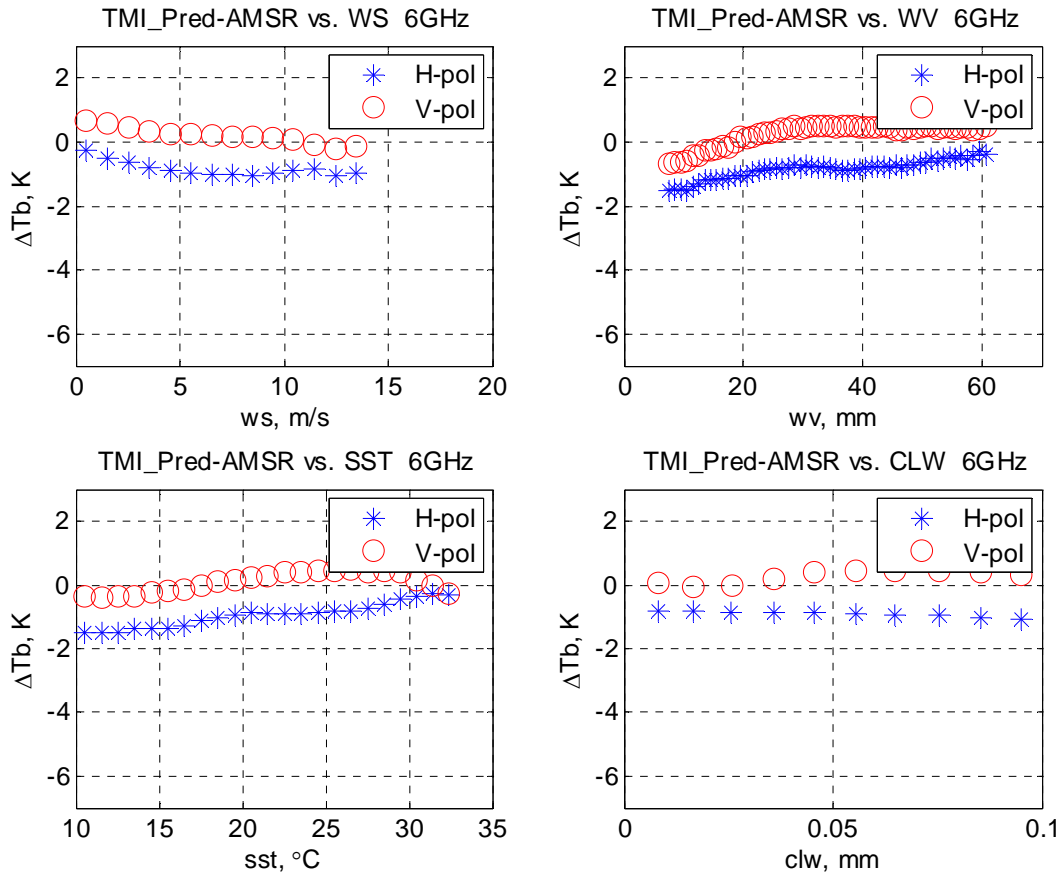
(a)   6.925 GHz
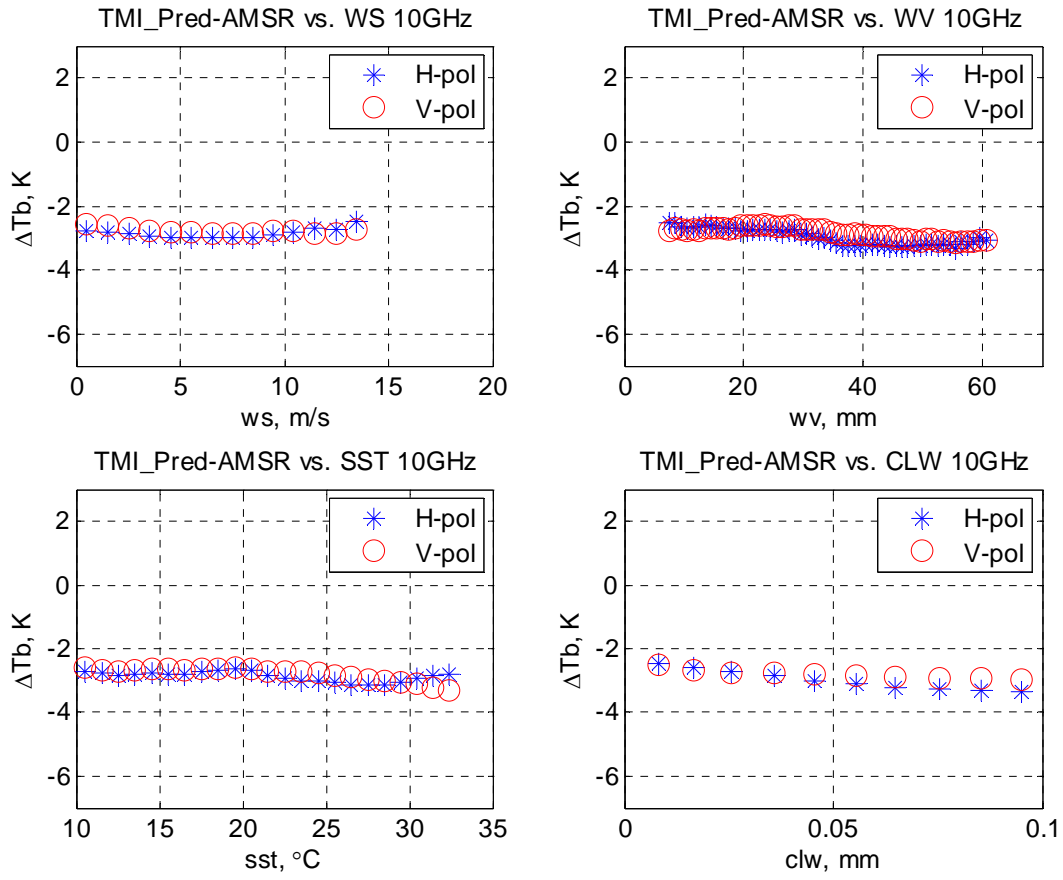
(b)   10.65 GHz
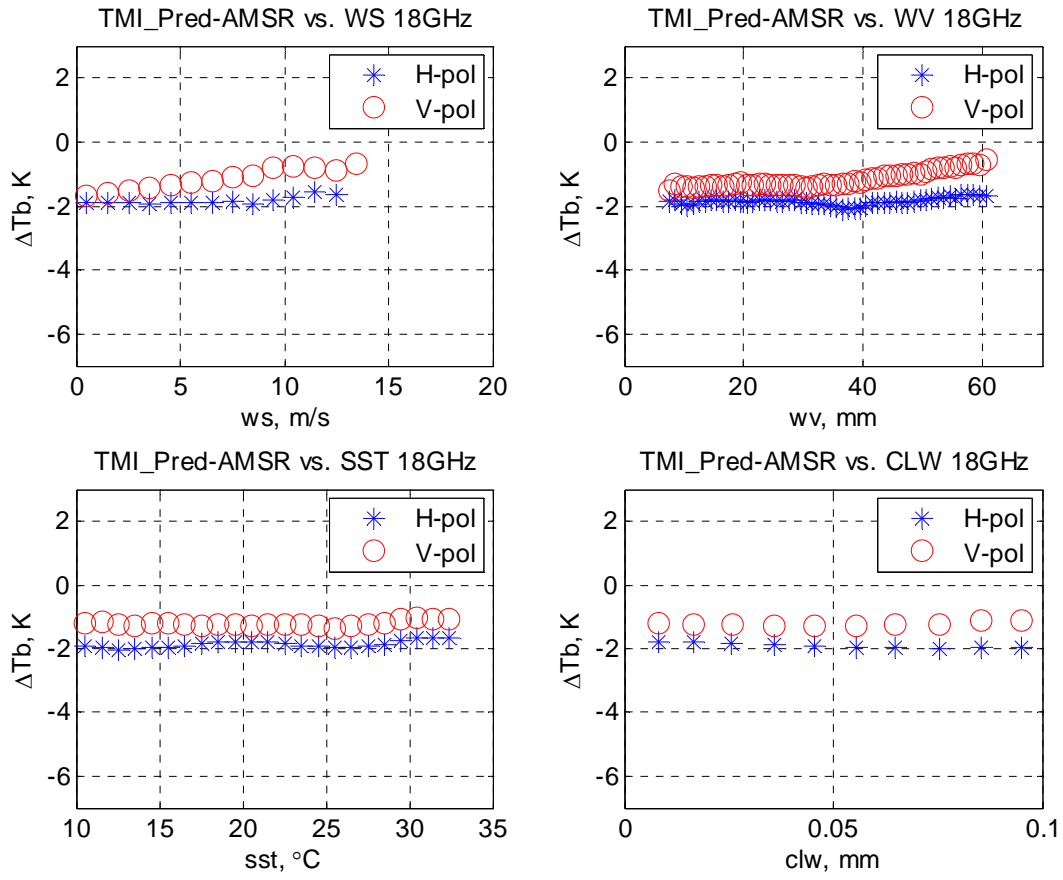
(c)   18.7 GHz
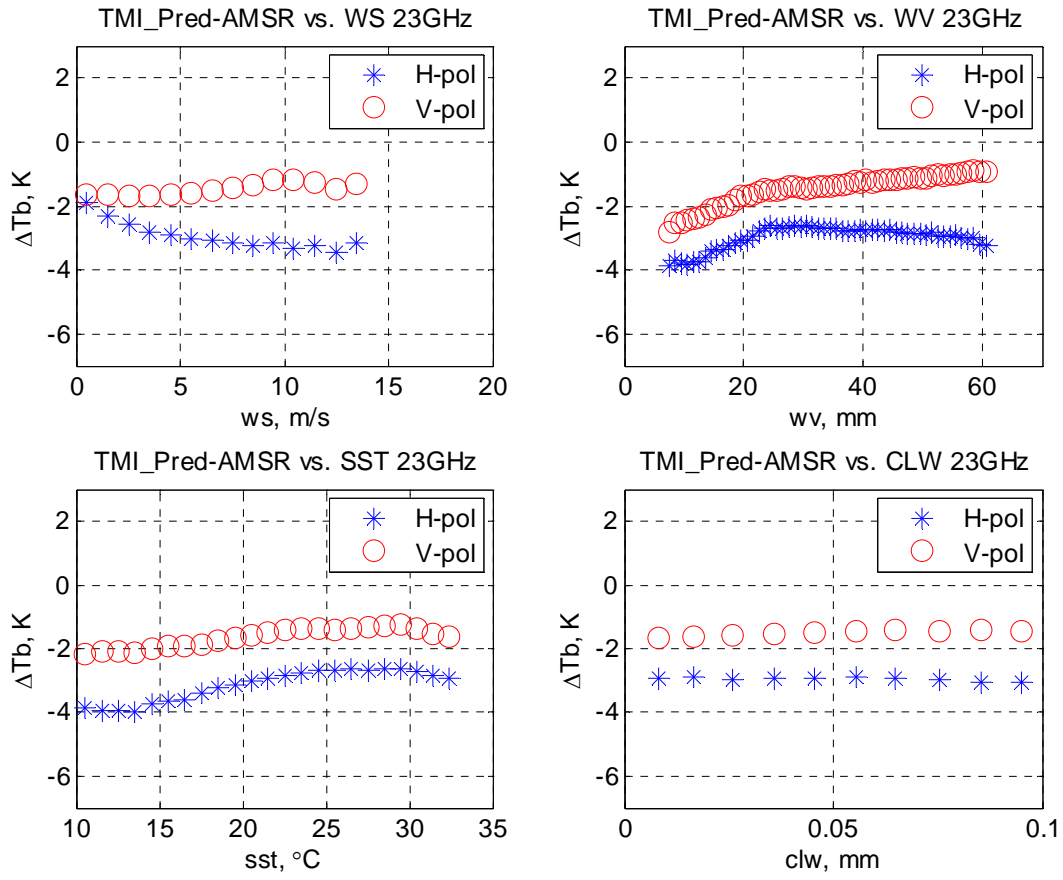
(d)   23.8 GHz
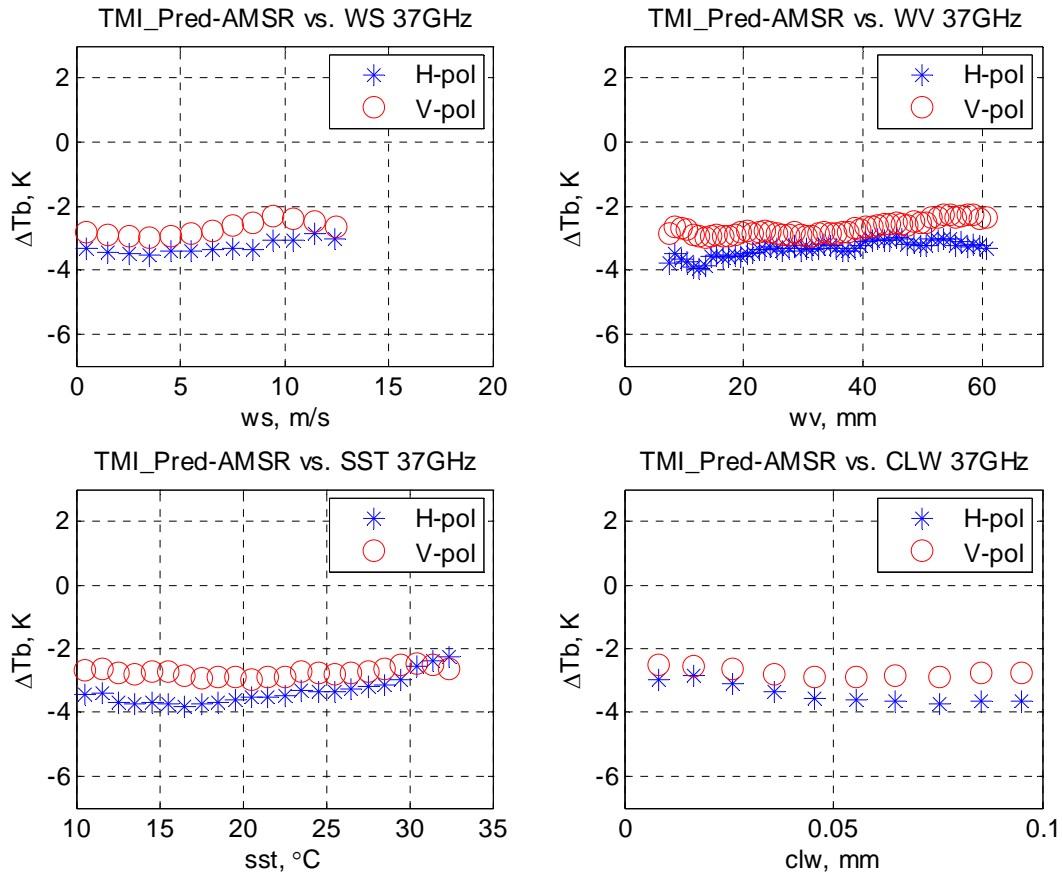
(e)   36.5 GHz

Figure 6.21: TMI to AMSR Calibration (Multi-Channel Regression) vs. Geophysical Conditions

6.2.4   Tb Bias in Two Approaches with all Collocations

By applying both approaches and using all collocations between AMSR and TMI, cross-calibrations results were derived and these results are shown in Table 6.11. A subset of the total collocations was analyzed (under limited geophysical condition where WS ≤ 8m/s, WV ≤ 40mm and CLW ≤ 0.1mm), and results are presented in Table 6.12. Differences of mean and STD values are smaller than 0.2; and these biases and standard deviations are very similar to Table

6.11. Also Figure 6.22 shows an example of a scatter plot of cross-calibration biases from both approaches. For 10 and 37 GHz channels, these scatter plots align-on or parallel with the 45-degree line. For all other channels, scatter plots are noisier but still cluster around the 45-degree line.

Table 6.11: ΔT_b in TMI to AMSR Prediction by Taylor Series Expansion for All Cases

23784 cases in total

Δ = TMI Prediction - AMSR		6H	6V	10H	10V	18H	18V	23H	23V	37H	37V
Taylor Series Expansion	Mean	-1.42	-0.40	-1.32	-0.58	-2.98	-1.28	-3.87	-5.14	-3.37	-4.25
	Std	0.73	0.78	0.59	0.50	0.73	0.61	1.37	1.84	1.55	0.74
Multi-Channel Regression	Mean	-0.93	0.14	-2.92	-2.86	-1.92	-1.31	-2.87	-1.49	-3.53	-2.82
	Std	0.71	0.87	0.65	0.53	0.64	0.59	0.89	0.75	1.56	0.76

Table 6.12: ΔT_b in TMI to AMSR Prediction by Taylor Series Expansion for Limited Cases

where WS ≤ 8m/s, WV ≤ 40mm and CLW ≤ 0.1mm, 13,285 cases in Total

Δ = TMI Prediction - AMSR		6H	6V	10H	10V	18H	18V	23H	23V	37H	37V
Taylor Series Expansion	Mean	-1.39	-0.30	-1.33	-0.61	-3.15	-1.39	-3.92	-4.49	-3.63	-4.36
	Std	0.62	0.67	0.55	0.47	0.60	0.55	1.52	1.83	1.38	0.64
Multi-Channel Regression	Mean	-0.99	0.13	-2.81	-2.78	-1.97	-1.46	-2.85	-1.68	-3.73	-3.01
	Std	0.67	0.84	0.59	0.49	0.59	0.50	0.96	0.68	1.43	0.63
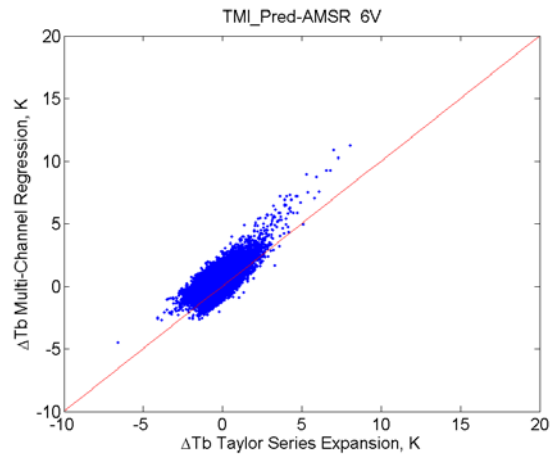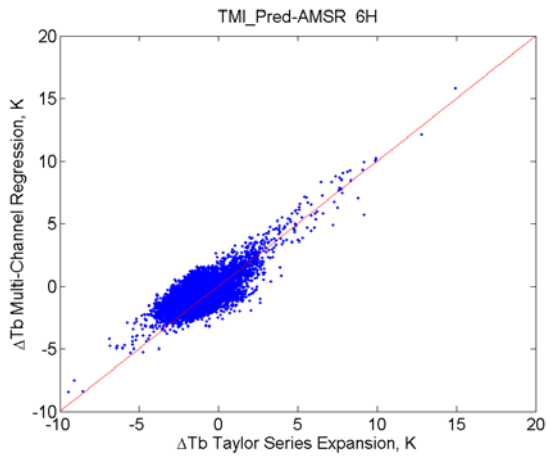
(a)   6.925 GHz

(b)   10.7 GHz

(c)   18.7 GHz

118
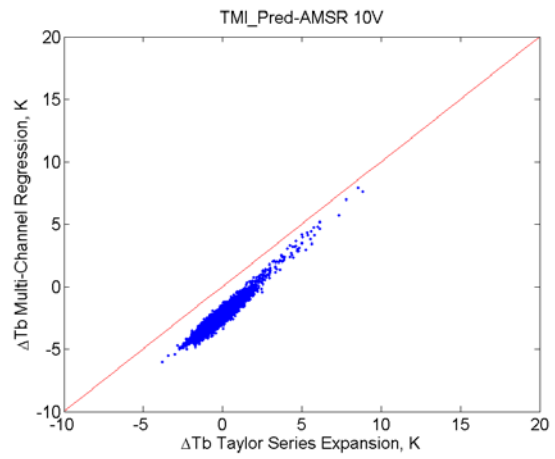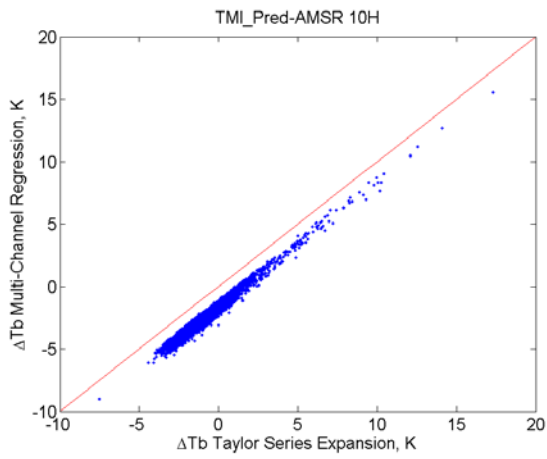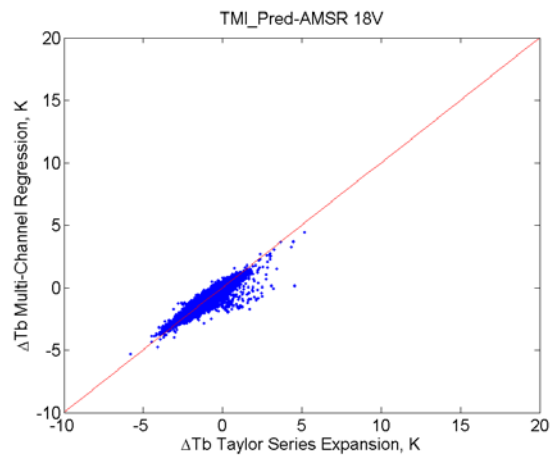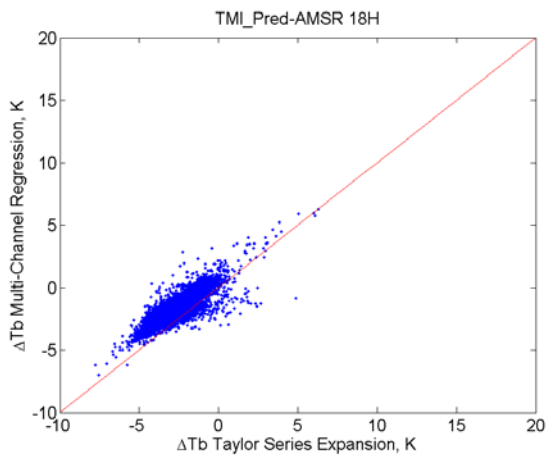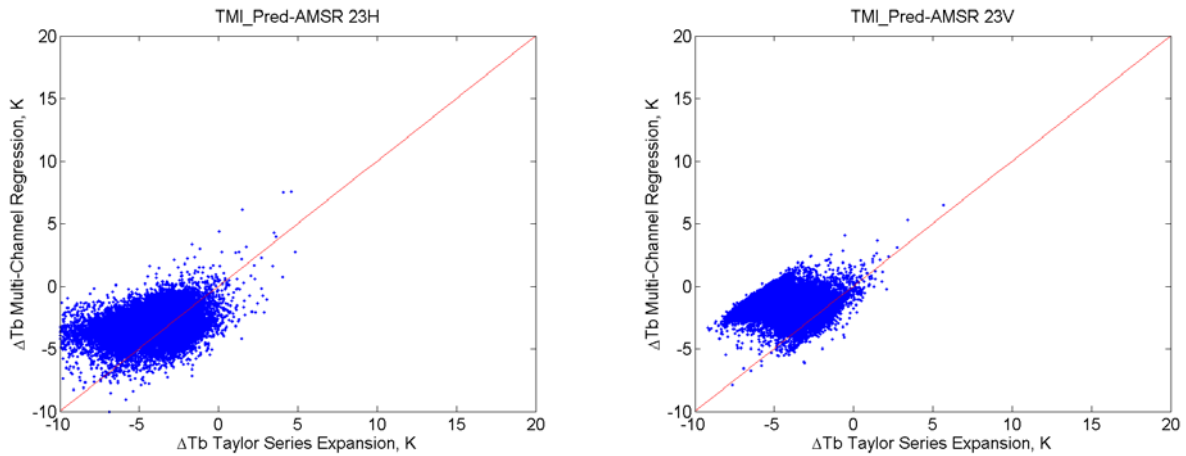
(d)　23.8 GHz
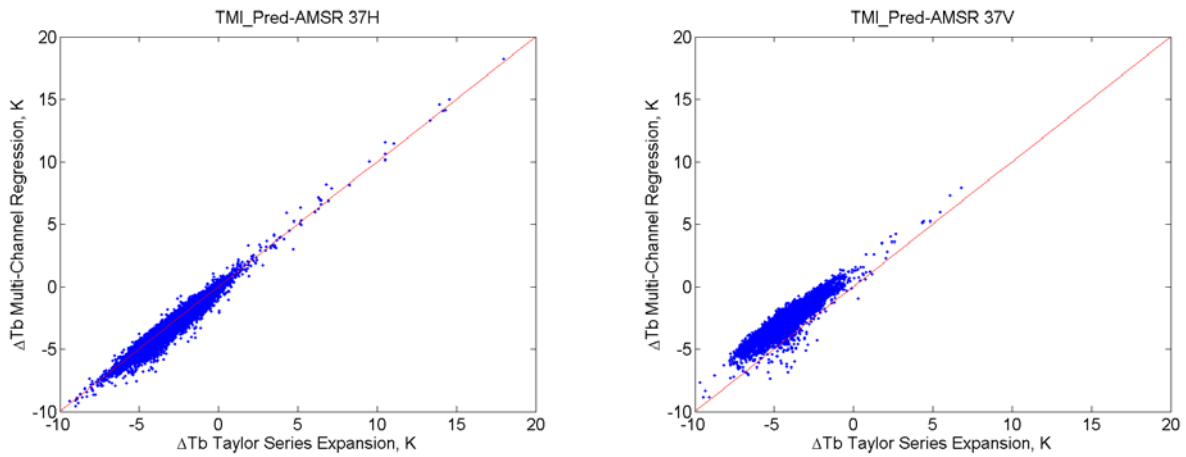
(e)　36.5 GHz

Figure 6.22:　Scatter Plot of TMI to AMSR Calibration T_b biases in Both Approaches

6.3　WindSat and AMSR

If WindSat overestimates the TMI measurement and TMI underestimates the AMSR measurement, then WindSat to AMSR prediction biases cancel to a large extent, and this is shown in Figures 6.23 and 6.24. For horizontal polarizations, the calibration results suggest 2K to 4K offsets should be added to TMI channels to match the WindSat measurements; offsets of -

1K to -4K are suggested to be added to AMSR channels in order to match the corrected TMI measurements. For vertical polarizations, calibration results suggest 0K to 5k offset should be added to the TMI channels to match WindSat measurements; offsets of 0K to -5K are suggested to be added to AMSR channels in order to match TMI measurements.

In both approaches, for horizontally polarized channels, ΔT_b's (equals to TMI prediction minus AMSR measurement) of AMSR ascending paths (in red) are more than 0.5 K larger than those of descending paths (in green). For vertically polarized channels, ΔT_b's are similar for both ascending and descending paths. Since AMSR ascending paths occur at night and descending paths are during daylight, it is suggested that the 0.5 K difference in horizontally polarized channels may possibly be caused by a solar heating effect on the instrument.
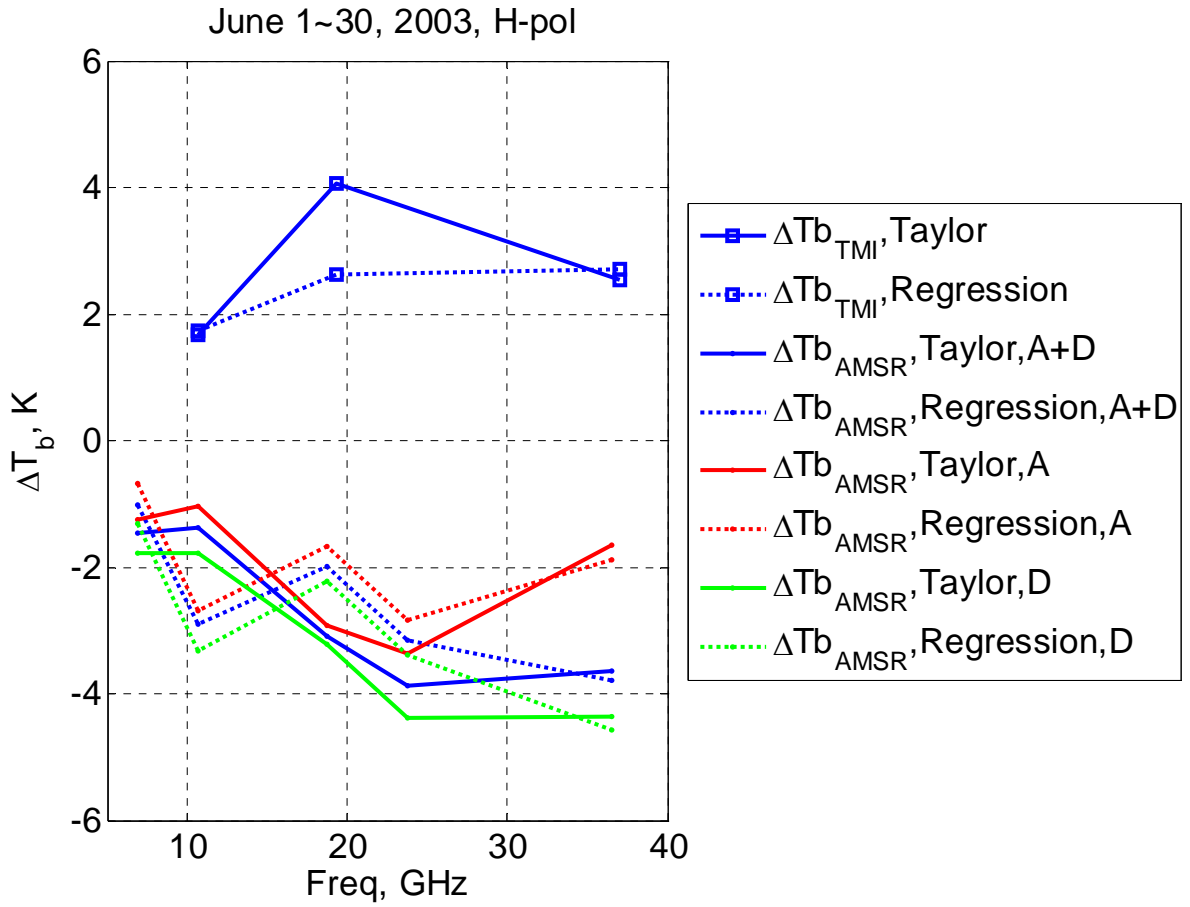
Figure 6.23: Composite of WindSat to TMI and TMI to AMSR Calibrations with H-pol

Channels
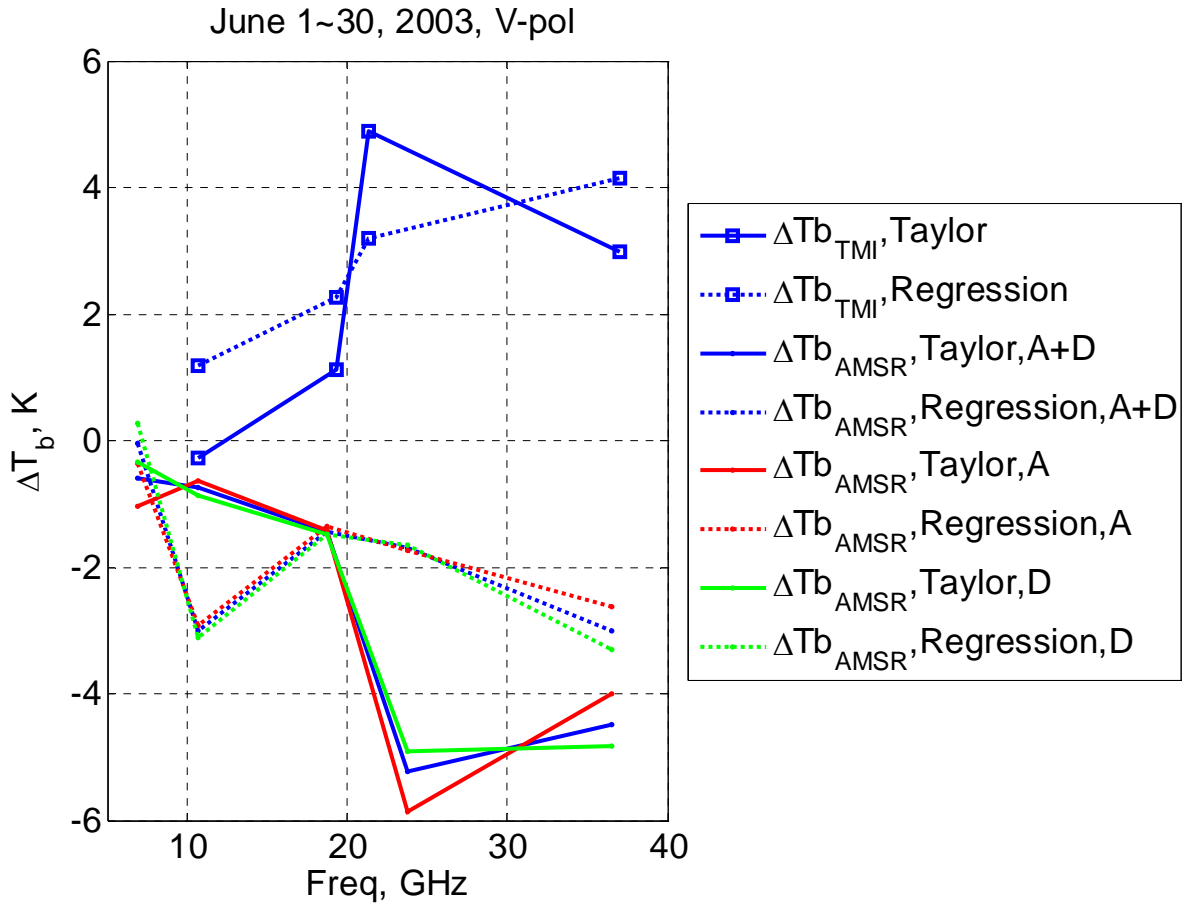
Figure 6.24: Composite of WindSat to TMI and TMI to AMSR Calibrations with V-pol

Channels

By adding suggested calibration biases in Table 6.5 to TMI measurements, and applying

the "corrected" TMI to predictions of AMSR channels, intermediate calibrations of WindSat to

AMSR was performed. Results in Table 6.13 show very good agreement on WindSat and AMSR

calibration with Taylor series expansion approach. While larger discrepancies are seen in results

of most channels in multi-channel regression approach, they are much less than those of either

WindSat to TMI calibration or TMI to AMSR calibration; and figures 6.25 and 6.26 show plot of

the above calibration results. The correlations between vertical and horizontal channels are 0.85

and 0.89 in Figure 6.25 and 6.26, respectively.

Table 6.13: Difference between AMSR and WindSat, Transferred by Calibrated TMI

Δ = Prediction - AMSR		6H	6V	10H	10V	18H	18V	23H	23V	37H	37V
Taylor Series Expansion	Mean	0.51	-0.66	0.61	-0.84	1.11	-0.17	0.22	-0.49	-0.79	-1.23
	Std	0.73	0.78	0.59	0.50	0.73	0.61	1.37	1.84	1.55	0.74
Multi-Channel Regression	Mean	0.55	1.79	-1.34	-1.36	0.44	0.49	2.02	1.62	-0.58	-0.56
	Std	0.72	0.86	0.66	0.54	0.64	0.64	0.93	0.68	1.54	0.89
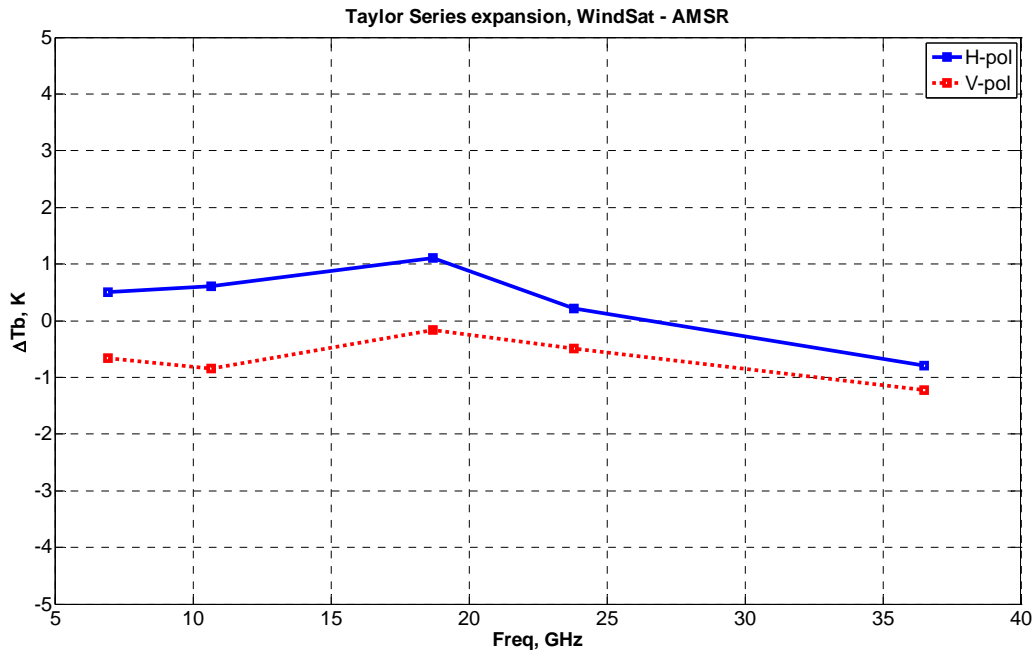
Figure 6.25: AMSR Calibration with TMI (Calibrated by WindSat) by Taylor Series Expansion
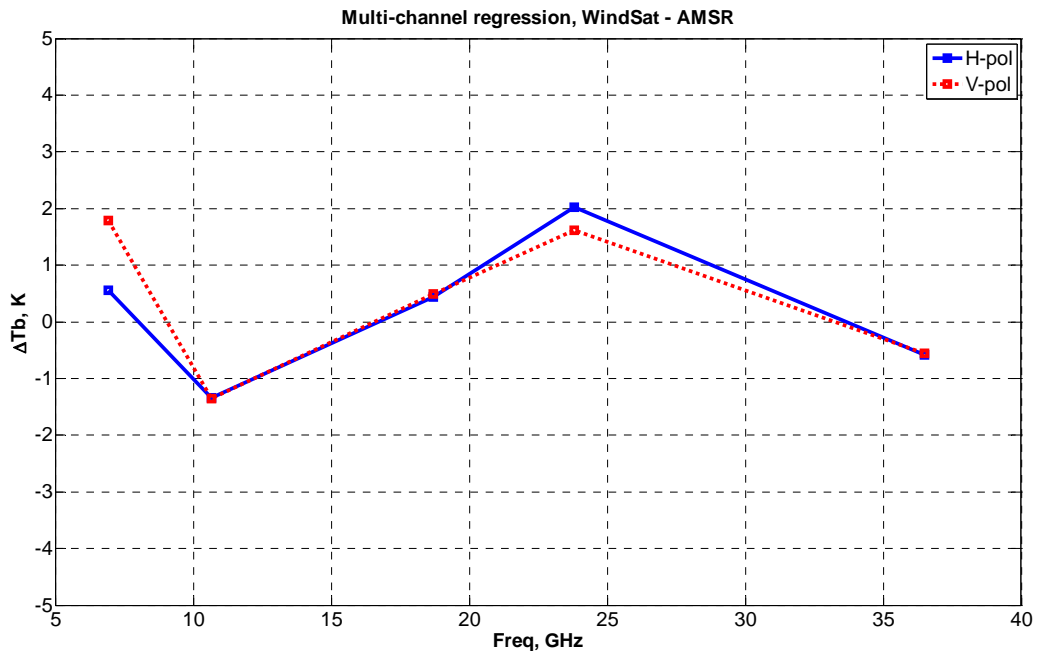
Figure 6.26: AMSR Calibration with TMI (Calibrated by WindSat) by Multi-Channel Regression

CHAPTER 7 : CONCLUSION

According to empirical investigations performed during this dissertation, the Taylor Series Prediction approach can be used to achieve the requirements of NASA's Global Precipitation Mission for inter-satellite radiometric calibration, which relies on a constellation of cooperative satellites with a variety of microwave radiometers to make global rainfall measurements.

It has been well established that the removal of systematic brightness temperature biases is necessary when producing decadal passive microwave data sets for weather and climate research. To achieve this goal, in-orbit techniques that provide a long term, group-wise solution, were investigated to reach T_b measurement agreement among a constellation of satellites as well as to maintain sustained calibration accuracy over the lifetime of each satellite sensor.

Since radiometers operate at different frequencies and viewing angles, T_b normalizations were made before making intermediate comparisons. This dissertation presents a new approach, namely, the Taylor series expansion prediction method, for the inter-satellite calibrations over oceans. These normalizations were built on a Taylor series expansion of T_b as a function of channel frequency, polarization and earth incidence angle (*EIA*) developed using a microwave radiative transfer model (RTM). The evolution of the RTM used in this research was described and the details of the tuning of the major subroutines to agree with actual on-orbit brightness temperatures were presented in Chapter 4. Tests and validation of the tuned RTM under the majority of realizable geophysical conditions were conducted and demonstrated excellent performance before application in building frequency and *EIA* normalization functions in the form of Taylor series expansions.

In addition, our approach was used to perform inter-satellite radiometric calibrations using actual satellite data as a demonstration of its potential use for NASA's future GPM program. We performed cross-calibrations between two sun-synchronous polar orbiting satellites (WindSat and AMSR on ADEOS-2) using the non-sun synchronous radiometer TMI as secondary calibration transfer standard (and proxy for the future GPM Microwave Imager). These multi-channel microwave radiometers were cross-calibrated using near-simultaneous, pair-wise comparisons of T_b measurements over rain-free tropical ocean areas by applying our Taylor Series normalization methodology before inter-comparison. Further, an independent analysis of these same satellite radiometer data (using an different multi-channel regression cross-calibrations approach presented in chapter-6) also shows consistency with our results. Such agreement gives confidence in the applicability of our Taylor Series Prediction approach to inter-satellite radiometric calibration.

The Taylor series expansion approach has the following characteristics:

- Requires a reliable radiative transfer model
  - At least in a relative sense, to predict accurate relative changes in T_b over frequency and EIA
  - Taylor series coefficients are insensitive to RTM absolute T_b accuracy as long as biases are independent over the range of channel frequency separations
  - RTM requires a reasonable estimate of collocated geophysical parameters input
    - This is usually satisfied by simultaneous microwave geophysical retrievals available from the two radiometers under evaluation
- Depends on only single near-by channel (used for Taylor expansion center freq):
  - Radiometric calibration quality is critical for this source channel frequency

- o Other channels (in the source satellite radiometer) do not affect the target channel calibration

- Applies (universally) to calibration of any radiometer channel pairs

  - o Once Taylor series coefficients (functions of frequency & EIA) are produced, RTM is not needed in calibration procedure for different calibration pairs

  - o New Taylor series expansion coefficients can be derived from saved functions

- Transfers calibration and enables cascaded linear calibrations

  - o e.g., WindSat to TMI and TMI to AMSR calibrations can be performed separately, then biases can be added in corresponding channels to perform WindSat to AMSR calibration

- Performs efficiently: thousands of cross-calibrations in minutes with very modest computer resources

7.1   Error Source

The inter-satellite calibration biases are a combination of actual sensor calibration differences and errors associated with the comparison methodology. Although a detailed error analysis was not performed, the following discussion is a subjective evaluation of the major error sources that must be considered in establishing the cross-calibration accuracy.

First is the error associated with simultaneous and collocated T_b observations. Since the antenna instantaneous fields-of-view (IFOV) will never be exactly the same, nor will the times of observation, there will always be some random error in matching the scenes of apparent brightness temperatures, which vary both temporally and spatially with the associated

geophysical parameters. The effect of these errors can be estimated by parametrically varying the spatial and temporal tolerances of the pair of radiometer measurements being collocated and by examining the means and standard deviations of the resulting biases. However, for this dissertation, we selected the binned average over relatively large 1° x 1° lat/lng boxes to mitigate these issues. Over this box size, most geophysical parameters are nearly uniform; and within these boxes, we use a spatial tolerance of 25 km, which is about the average size of the various channel IFOV's to match-up T_b measurements. Temporally, we selected a conservative ±15 min window, which still allows frequent observations while providing adequate sampling of the typical rates of change of environmental parameters over the IFOV areas (10's of km). Further, the quality control procedures used in this investigation, removed heterogeneous scenes (e.g., rain and heavy cloud cover) by limiting the acceptable standard deviation of box averages for filtered collocations. Thereby, large random outliers were remove from the data set before inter-comparisons. Finally, the large number of collocations achieved will yield Gaussian statistics, which leads to well founded statistical analysis procedures and estimates of confidence limits of the estimate of the means.

The translation to a common frequency and incidence angle basis will also result in residual error because since it uses an imperfect radiative transfer model and regression curve fitting to produce the Taylor series coefficients. Further, these normalizations depend on the actual oceanic and atmospheric environmental conditions, which are estimated from available satellite retrievals and NOAA GDAS numerical weather models to provide the necessary RTM environmental inputs. The resulting frequency and incidence angle interpolation errors can be estimated from the modeling residuals, which have a small systematic component as well as the random error.

According to RadTb model simulations, T_b linearly varies with incidence angle around 53.2 º (TMI incidence angle). In the frequency range of 5 to 40 GHz, the vertically polarized T_b's varies with incidence angle change at a slope 2 to 2.5 K/deg; while the horizontally polarized T_b's are not so sensitive to incidence angle changes, where the slope is -1 K/deg for frequency under 10 GHz, and within ± 0.5 K/deg for frequencies between 10 and 40 GHz. So, for the WindSat channels, the T_b uncertainty introduced by standard deviation of earth incidence angle (~ ±0.1 deg for any of its 22 channels) is less than ±0.25 K for vertical polarization and ±0.1 K for horizontal polarizations. TMI incidence angles fluctuate within the same range (0.1 deg). Assuming that AMSR has the 0.1 deg EIA fluctuation range, the uncertainty of WindSat to AMSR calibration is within ±1 K for vertically polarized channels and ±0.3 K for horizontally polarized channels.

Finally, the ocean surface emissivity anisotropy is determined by the relative wind direction (difference between azimuth line of sight and the wind direction); and failure to account for this will introduce some small error (of order a few Kelvin). Since the ocean emissivity anisotropy is zero mean when averaged over all directions and since the two satellites in any collocation will never have the same viewing direction, the relative wind direction will be approximately uniformly distributed and the wind direction T_b will average to zero. On the other hand, the differential between collocated measurements may not; so this is a know error of unknown magnitude. This remains a task for future analysis.

7.2   <u>**Future Work**</u>

In the future research, the focus should be on reducing prediction uncertainty by applying techniques and processes to suppress error sources in the calibration approach; therefore, there remain several areas of research desired to improve this dissertation. First, is to improve the radiative transfer modeling for atmospheric water vapor and cloud liquid. Both of the geophysical parameters affect the apparent T_b for radiometer channels greater than X-band (10.6 GHz). In this dissertation there were ad hoc corrections developed to match WindSat observed and modeled brightness temperatures at K- and Ka-bands (18 – 37 GHz). This effect should be studied to improve microwave RTM's especially near the peak of the water vapor resonance 22.225 GHz. Since water vapor is a robust geophysical retrieval for microwaves, it should be possible to improve the forward modeling using multi-channel satellite radiometers. For cloud liquid water, this is less problematic because there are sufficient collocations with low cloud contents; so data editing will mitigate the immediate problem. However, as the inter-calibrations move higher in frequency (e.g., SSMI 87 GHz channel), cloud liquid and cloud ice are significant issues for radiometric calibration. Therefore, improved radiative transfer modeling including particles scattering will be required for the GPM era radiometric systems.

A hot end (e.g. Amazon area) and a cold end (e.g. Greenland glacier) are needed for a complete inter-satellite calibration, and because of small non-linearity's between receiver power output and target brightness temperature, external natural calibration targets of wider dynamic range T_b's are preferred. Also, expanded external calibration range supports the expected wider T_b range associated with oceanic precipitation using millimeter wave radiometer systems. For future work, emphasis should be on identifying and characterizing the radiometric behavior of

130

natural land and ice surfaces at a wide range of frequencies from 1 GHz to over 200 GHz to serve as these alternate external calibration sources for inter-satellite cross-calibration. Certainly some work has been performed; but much more is needed.

APPENDIX A: TOTAL POWER RADIOMETER

A.1   Total Power Radiometer

The total power radiometer, Dicke radiometer, and noise-injection radiometer are the three most common types of microwave radiometers. Among these, the total power radiometer is of the simplest being comprised of an antenna, a microwave receiver and a power detector; and this is the design of choice for the majority of satellite radiometer imaging systems.

A.1.1   Design and Sensitivity

The simplified block diagram of a microwave total power radiometer is shown in Figure A.1. When the radiometer views a distributed target, non-coherent microwave radiation (noise) is collected by the antenna and passed to the receiver where it is amplified. The power output from the receiver is detected by a square-law (power) detector and integrated to produce a stable DC voltage, which is proportional to the receiver output power.
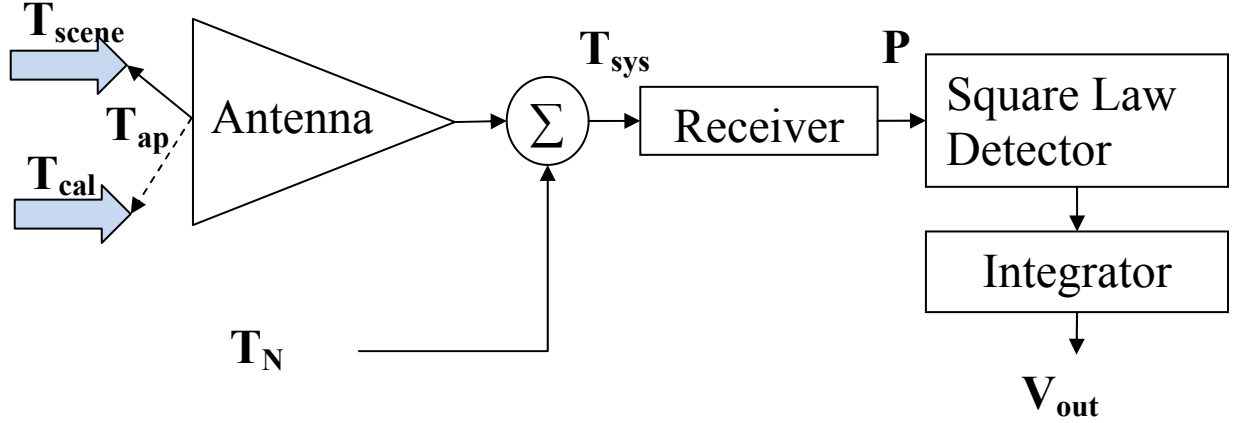
Figure A.1: Total Power Radiometer

In practical receivers, the output power is the amplified noise power collected by the antenna plus internally generated noise by the receiver electronics, which is expressed as an equivalent brightness temperature T_N, at the receiver input. Thus the total input noise to the receiver can be expressed as the system brightness temperature,

$$T_{sys} = T_{ap} + T_N \tag{A.1}$$

and the receiver power output is

$$P = kT_{sys}BG \tag{A.2}$$

where the sensitivity of the total power radiometer, or Noise Equivalent Delta T (NEΔT) [2], is

$$NE\Delta T = T_{sys}\sqrt{\frac{1}{B\tau} + \left(\frac{\Delta G_{sys}}{G_{sys}}\right)^2} \tag{A.3}$$

where, τ is the integration time in seconds. G_{sys} is the average system power gain. ΔG_{sys} is the effective value (rms) of power gain variation. To minimize the *NEΔT*, it is important to measure the dynamic receiver gain using frequent radiometric calibrations (over a period shorter than the gain changes) and thereby reduce the *ΔG/G* term in equation A.3.

Depending upon the remote sensing application, radiometers usually have multiple channels, with different center frequencies, bandwidths, integration times and T_{sys}; therefore, as a result, the NEΔT usually varies from channel to channel. The sensitivity of a modern satellite radiometer is typically less than 1 Kelvin (K).

A.1.2 Radiometric Calibration

The radiometer output noise is rectified by the square-law detector, and the resulting average value (DC output voltage) is linearly proportional to the radiometer input brightness temperature (power), which contains both the desired antenna T_{ap} and the undesired receiver noise temperature, T_N. Post-detection, this signal passed through a low-pass filter (integrator) to remove the AC noise component in the output and produce a precise estimate of the average output power. Thus, the integrator output, in digital counts or voltage, is a scaled version of the receiver system brightness temperature:

$$V_{out} = const \times \left(T_{ap} + T_N\right) = gain \times T_{ap} + offset \qquad (A.4)$$

Therefore, to measure the apparent brightness temperature of the scene, it is necessary to calibrate the radiometer in absolute power units and with high precision to determine the instantaneous radiometer gain and the offset noise level due to the receiver T_N.

The optimum radiometric calibration can be achieved by using absolute external calibration targets that calibrate the entire radiometer including the antenna. For the majority of satellite radiometers, a mechanical system is used to sequentially place two blackbody targets of known physical temperatures (hot and cold) over the antenna feeds to establish the linear calibration line. The high temperature target, or hot-load, is a blackbody microwave absorber

(very high emissivity ~ unity) with measured physical temperature. The temperature of the hot-load is controlled to be isothermal and very stable at some preset value, e.g., 350 K. Therefore, the total (absolute) radiation emitted from the hot-load can be calculated from its physical temperature and emissivity. Ideally, the cold-load should also be an isothermal blackbody whose physical temperature is less than the scene brightness temperature. For satellite radiometers, a convenient cold-load source is achieved by pointing the antenna to view deep space, whose brightness temperature is spatially homogeneous and isotropic with a value of 2.73 K.

By mechanically positioning the antenna to alternatively view the earth's surface (T_{scene}) and subsequently to view hot and cold calibration sources (T_{cal}), the linear coefficients (gain and offset) in equation A.4 can be derived.

This linear equation (illustrated in Figure A.2) is used calculate the scene apparent brightness temperature (T_{ap}) from the related receiver output voltage.

$$T_{scene} = \left(\frac{T_H - T_C}{V_H - V_C}\right)(V_A - V_C) + T_C \qquad \text{(A.5)}$$
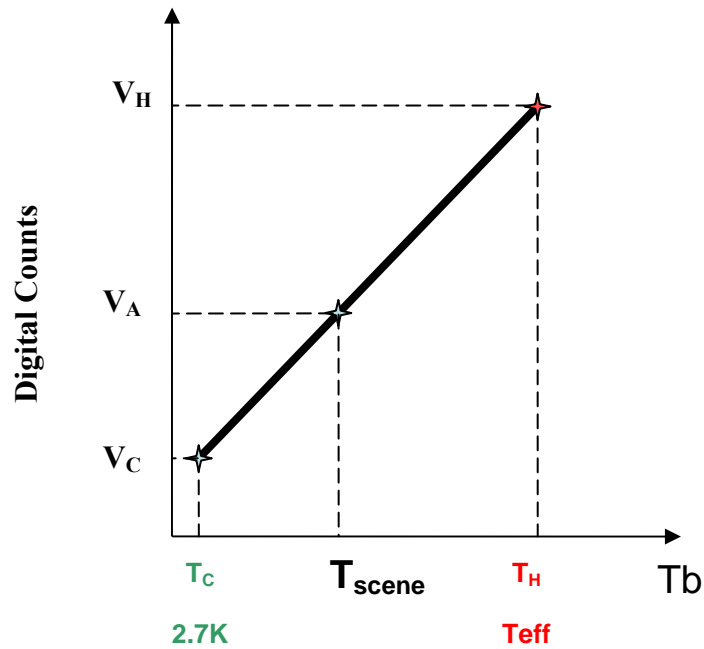
Figure A.2: On Board Calibration

where, T_H and T_C are the known (measured) brightness temperature of the hot load and cold load respectively. The integrator output voltages (digital counts) V_A, V_H and V_C correspond to the apparent (scene), hot-load and cold-load antenna brightness, respectively.

Knowledge of the absolute brightness temperature of the calibration targets is critical to the absolute radiometric calculation. By assuring isothermal conditions for the blackbody calibration targets and making accurate physical temperature measurements, as well as using a high emissivity (low reflectivity) passive microwave absorber as the calibration source, apparent brightness temperature measurements with absolute accuracies of better than 1 K can be achieved.

Unfortunately, the physical temperature of the receiver electronics, as well as the electronic power supply DC voltages and currents can affect the calibration (receiver gain and

the internal noise offset); thus, it is mandatory that the system be continuously calibrated whenever measurements are made. The mechanical configuration of conical scanning satellite radiometers easily fulfills the frequent (once/revolution) calibration requirement.

A.1.3   Conical Scanning Microwave Radiometer

Most satellite microwave radiometers, used for environmental measurements, are conical-scanning total power radiometers (as shown in Figure A.3). These instruments consists of a mechanically spinning main reflector with multiple-channel feed-horns and receivers that image the earth's brightness temperature with "spot beams" that travel across the satellite ground-track on a circular arcs that over-lap (~ 50%) on successive antenna rotations. Figure A.4 illustrates a typical conical scan pattern for several spins.

For external total power radiometer calibration, a stationary calibration system (cold sky reflector and a hot blackbody target) are located at the top of the rotating canister. When the rotating feedhorns pass beneath the hot and cold load (once every revolution), the corresponding radiometer output digital counts are recorded and telemetered to the ground for data processing. Using these calibration data and equation A.5, the linear radiometer transfer function is established.
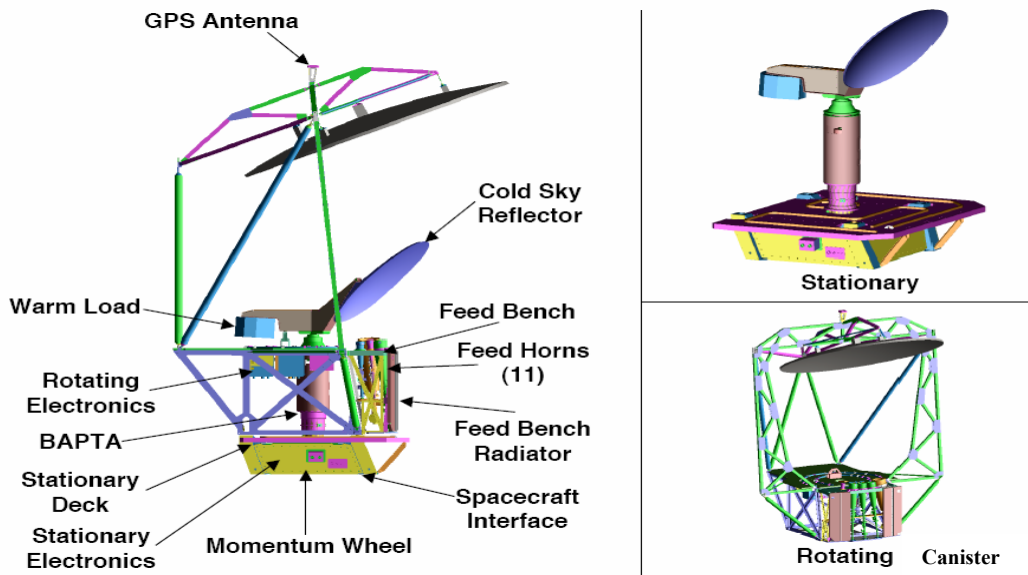
Figure A.3: Example of Conical Scanning Radiometer - WindSat [38]
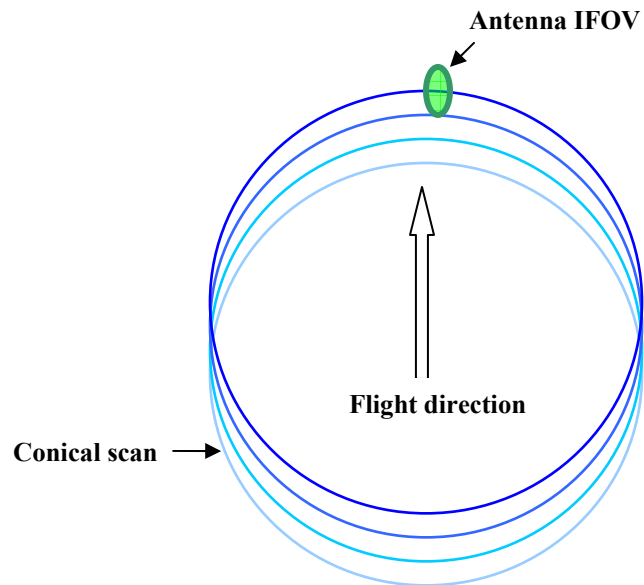
Figure A.4: Example of a typical Conical Scanning Pattern

A.1.4 Post-Launch Calibration

Although microwave radiometer instruments under-go extensive pre-launch calibration in thermal vacuum (TV) testing facilities, it is important to verify proper radiometric performance on-orbit; and (unfortunately) proper pre-launch calibration is still not a guarantee of the absolute accuracy of on-orbit brightness temperature measurements. In fact, calibration surprises (problems) have been found in post-launch analyses for almost every conical-scanning microwave radiometer launched to orbit, and these issues have resulted in absolute calibrations adjustments of several Kelvin or more. Examples include, but are not limited to: unexplained high reflector emissivity and an IFOV obstruction at the end of each scan on TMI [3], unstable hot load on AMSR [4 - 6], transient sun illumination on hot load on WindSat [7]. These problems are extremely difficult to predict or prevent before launch, and post-launch calibrations are required to solve these problems while the instruments are in orbit.

A.2   Satellite Total Power Microwave Radiometers

The first multi-channel microwave imager, Scanning Multi-frequency Microwave Radiometer (SMMR), was launched into orbit in 1978 on two NASA research satellites (SeaSat-A and Nimbus-G). Because of its antenna design, there were absolute calibration issues with SMMR, which were later corrected by the next generation of external-calibrated, total power radiometer, conical-scanning microwave imagers, Special Sensor Microwave Imager (SSM/I).

SSMI operates with seven linearly polarized microwave channels that span the 19 − 85 GHz frequency range. The SSM/I series of "operational instruments" were carried onboard the Defense Meteorological Satellite Program (DMSP) series of polar orbiting satellites numbered as: F-8 SSM/I (Jul 1987 to Dec 1991); F-10 SSM/I (Dec 1990 to Nov 1997); F-11 SSM/I (Dec 1991 to May 2000); F-13 SSM/I (May 1995 to present); F-14 SSM/I (May 1997 to present); F-15 SSM/I (Dec 1999 to present) [39].

In the study of inter-sensor calibration of SSM/I's from F-8 to F-14 [14], sensor-specific components, orbital configuration, and systematic relative errors were examined that contribute to the total system calibration. In particular, a large (1–3 K) but correctable left–right scan asymmetry of SSM/I brightness temperatures was observed in the data and traced to an antenna field-of-view (FOV) intrusion by the spacecraft and other instruments. Also, antenna pattern correction (APC) coefficients were found to be the source of large inter-sensor differences for several channels, e.g., 1–2 K for the 22-V channel.

A.2.1   TMI Radiometer

The conical-scanning total power radiometer, TRMM Microwave Imager (TMI), is based upon the SSMI design with the addition of two 10.6 GHz dual-polarized channels. This microwave imager flying was launched on November 1997 into a non-sun synchronous orbit (35° inclination @ 350 km altitude) for continuous monitoring of the tropics. Because of its low orbital altitude, TRMM was affected by atmospheric drag; and an orbit-boost maneuver in August 2001 significantly extended its mission life by increasing this operating altitude to 403 km. TMI has four dual polarization channels and one v-polarization channel and a swath width

of 878 km after the boost. Other key radiometer instrument parameters, after the boost, are shown in Table A.1 [40].

Table A.1: TMI Instrument

Measurement Channel (GHz)	Temperature Sensitivity NEΔT (K)	Pass-Band Band Width (MHz)	Beam Width (deg)	IFOV (km) Along Scan x Cross Scan	Earth Incidence Angle (deg)
10.65 H/V	0.54/0.63	100	3.75/3.68	40x67	53.2
19.35 H/V	0.47/0.50	500	1.88/1.90	21x34	53.2
21.3 V	0.71	200	1.70	19x31	53.2
37.0 H/V	0.31/0.36	2000	1.0/1.0	11x18	53.2
85.5 H/V	0.93/0.52	3000	0.43/0.42	4.7x7.7	53.2

Post-Launch Calibration of TMI by Frank J. Wentz, et al. [3] showed systematic along-scan error of ~1K and warm-bias of ~5K caused by a slightly emissive main reflector; and Version-5 of the TMI data products incorporates both the along-scan and warm bias corrections discussed in that paper.

A.2.2   AMSR Radiometer

The AMSR on board ADEOS-II was launched in 2002 to a sun-synchronous orbit with an altitude of 830 km and inclination of 98.7^o. AMSR is a large-aperture, conically-scanning total-power microwave radiometer (Fig. A.5), which operates with 7 dual-polarized channels from 6 - 89 GHz plus two vertically polarized channels at around 50 GHz. AMSR has an offset parabolic antenna with effective aperture size of 2.0 meters, which produces a swath width of 1600 km. The major contribution of the instruments is to obtain global and continuous records of

water-related geophysical parameters for understanding the mechanism of water and energy circulation [4]. A list of key radiometer parameters are shown in Table A.2 [4].

Table A.2: AMSR Instrument

Measurement Channel (GHz)	Temperature Sensitivity NEΔT (K) @150K	Pass-Band Band Width (MHz)	Beam Width (deg)	IFOV (km) Along Scan x Cross Scan	Earth Incidence Angle (deg)
6.925 H/V	0.34	350	1.8	40x70	55.0
10.65 H/V	0.7	100	1.2	27x46	55.0
18.7 H/V	0.7	200	0.65	14x25	55.0
23.8 H/V	0.6	400	0.75	17x29	55.0
36.5 H/V	0.7	1000	0.35	8x14	55.0
50.3 V	1.8	200	0.25	6x10	55.0
52.8 V	1.6	400	0.25	6x10	55.0
89.0A H/V	1.2	3000	0.15	3x6	55.0
89.0B H/V	1.2	3000	0.15	3x6	54.5
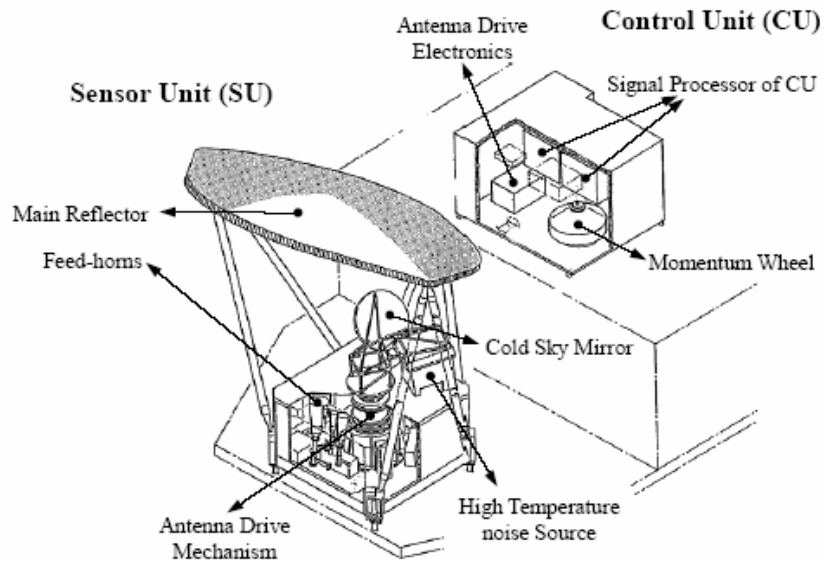
Figure A.5: Overview of AMSR on ADEOS-II Platform [4]

In 2003, studies of the AMSR on ADEOS-IIA and AMSR-E on AQUA suggest a receiver linearity problem to explain the anomalous biases between some AMSR channels and both SSM/I and the airborne AMSR instrument over continents [5, 6]. It was found that the simple two-point calibration did not work properly due to the temperature inhomogeneous characteristics of hot load [5]. Additional procedures were performed to eliminate that effect and then to derive the Tb values from raw data counts for the JAXA version-1 L1B product. In short, the procedure is the combined approach of two independent methods. One method is to represent the effective radiating temperature of the hot-load by a multiple regression model parameterized by eight Platinum Resistance Thermometers (PRT) readings. The other method is to utilize the relationship between receiver physical temperature and its gain variation.

A.2.3   WindSat Radiometer

WindSat is a large-aperture, conically scanning total power polarimetric radiometer on-board the Coriolis spacecraft, which was launched into a sun-synchronous orbit (840 km and 98.7° inclination) on January 6, 2003. The WindSat instrument is a multi-frequency fully polarimetric radiometer (vertical, horizontal, ± 45°, left- and right- circular) at 3 operating frequencies (10.7, 18.7 & 37 GHz) and dual polarimetric (vertical and horizontal) at 6.8 and 23.8 GHz. WindSat covers a 1025 km swath and provides both fore and aft views of the swath. Due to the arrangement of the feed horns, the incidence angle is different for each frequency, and varies from approximately 50° to 55° [35]. The key radiometer characteristics of WindSat instrument are shown in Table A.3 [35].

Table A.3: WindSat Instrument

Measurement Channel (GHz)	Temperature Sensitivity NEΔT (K) @250K	Pass-Band Band Width (MHz)	Beam Width (deg)	IFOV (km) Along Scan x Cross Scan	Earth Incidence Angle (deg)
6.8 V/H	0.63	125	1.78	40x60	53.53/53.53
10.7 V/H/P/M/L/R	0.44	300	1.13	25x38	49.90/49.90/ 49.93/49.93/ 49.93/49.93
18.7 V/H/P/M/L/R	0.44	750	0.65	16x27	55.35/55.35/ 55.35/55.35/ 55.33/55.33
23.8 V/H	0.60	500	0.54	12x20	53.0/53.0
37.0 V/H/P/M/L/R	0.42	2000	0.33	8x13	53.0/53.0/ 52.99/52.99/ 53.01/53.01

During the deep-space calibration of the WindSat radiometer [36], a series of satellite pitch maneuvers were performed to make the WindSat conical spinning antenna to view deep space during the forward (or aft portion) of the azimuth scan. When viewing the homogeneous and isotropic brightness of space, the resulting statistical averages were determined with great precision (typically < 0.05 K). Only a few channels had greater uncertainty and these were within a few tenths K, which totally satisfied the prelaunch T_b error budgets. The T_b differences (biases) between the main reflector and the cold-sky reflector for WindSat's channels were typically < 0.1 K (max bias < 0.16 K); and the change in absolute calibration with scan position (along-scan biases) were negligible (< 0.1 K) and quite stable over eight pitch maneuvers (four positive pitch and four negative pitch) separated by many months. For the polarimetric channels (V/H, $\pm 45^o$ and LHCP/RHCP), the biases between orthogonal channels were small (typically < 0.1 K) and very stable over the different pitch maneuvers. Only the 18-GHz $\pm 45^o$ channels had greater offsets, which are not believed to be a problem in normal WindSat Tb measurement. Also,

analyses, conducted to measure the main-reflector Tb coupling into the feeds during the cold-load calibration measurements, were determined to be negligible for all channels. Thus, the WindSat radiometric calibration campaign is believed to be an outstanding success, and these excellent results provide high confidence in the brightness temperatures from WindSat Temperature Data Records.

Absolute calibration of WindSat's third and fourth Stokes brightness temperatures (T_3 and T_4) were analyzed by applying a vicarious cold reference [37]. Results showed calibration biases of 0.2 -0.6K in 10.7 GHz T_3 and T_4 determined with a precision of 0.04K.

Finally, post-launch calibration of the WindSat radiometer indicates the presence of thermal gradients across the hot load during some periods of the year. These are caused by direct and reflected solar illuminations and earth eclipse that lead to calibration errors, since PRT's do not accurately reflect the physical temperature of the surface of the load due to the presence of large thermal gradients between the load surface and the load base. These hot load anomalies are worst when the sun beta angle is below 75° from April to August. These corrupted gains result in T_b errors greater than 1K (~9% of the time) and errors greater than 0.5K (21% of the time) with maximum amplitude up to ±2K in 18.7GHz channels [7].

A.3   Cross Calibration Analysis and Procedure

As described above, there are degradations of the pre-launch calibration experienced by satellite radiometers on-orbit. By applying inter-satellite calibration, not only will these errors be discovered, but also the consistency of measurements between sensors in the constellation can be achieved. Comparing the above three radiometers, we notice that they have several pairs of

channels operating at similar or identical frequencies. They have close incidence angles in the range of 50 to 55 deg for corresponding channels, and their ground resolutions are comparable. Interpolation, closest point selection and lat/lng box averaging will help to alleviate the problem of imperfect temporal and spatial matching from different radiometer in a collocated area. However, when two satellites simultaneously view the same point, generally they have similar, but not identical, observation parameters such as frequency, polarization and view angle. To accommodate these differences, algorithms need to be developed to predict the ocean brightness temperature observations from one satellite based on the observations of another. Comparison between observed and predicted radiances between two systems can establish cross-calibration consistency.

Among current operating space-borne radiometers, WindSat is probably the world's best calibrated microwave imaging radiometer [36]. Therefore, it is chosen to be the standard in our multi-radiometer calibration. Most of the radiometers of interest fly on polar orbiting satellites. Unfortunately, they do not have near-simultaneous pair-wise collocations over oceans except at high latitudes near the poles, which are mostly frozen ocean scenes; thus, it is necessary to find a transfer standard to build a link between any polar orbital radiometer and WindSat. The non-sun-synchronous orbital TRMM Microwave Imager (TMI) may serve as the transfer standard for collocations over tropical oceans with any other polar orbiting radiometer.

In our current research, the assessment of the TMI radiometric calibration is the first step toward the inter-calibration between WindSat and the Advanced Microwave Scanning Radiometer on the ADEOS-II satellite (AMSR). During this procedure, the brightness temperatures from collocations of orbital swaths are compared to WindSat to establish a radiometric offset and gain slope for each channel of TMI. Then AMSR is assessed with

146

calibrated TMI. Calibrations between WindSat and other polar orbital radiometers, such as Special Sensor Microwave Imager (SSMI) generally follow the same procedure.

Because the WindSat and TMI operating frequencies and incidence angles do not match, WindSat T_b's must be translated before comparison. This is accomplished using a physical basis RTM to provide equivalent WindSat T_b's on TMI channels. For this study, transfer methods are investigated to improve the T_b calibration knowledge. We examine the use of single channel Taylor series expansion models and multi-channel regression models to characterize WindSat/TMI/AMSR radiometric calibration and use simultaneous collocations within ± 15 minutes to minimize transient environmental effects on the observed brightness temperatures. An important part of this calibration process is the establishment of an error model to determine the sources of random and systematic error. Systematic errors are determined by statistical techniques and the uncertainties of the random errors are analyzed.

Details of the above approaches, including procedures of central frequency Taylor series expansion prediction and results from this approach, as well as results from multi-channel regression predictions are presented in chapters 3 through 6.

APPENDIX B: RTM MODULES

Changes were made to original RTM of CFRSL. Blocks in red are new or updated modules,

1) WV CORR is the water vapor input correction

2) CALCTTPHCBHCT calculates temperature of tropopause, heights of cloud base and top from climatology

3) ACLOUD has partial cloud corrections included

4) DIECON is the subroutine from Frank Wentz's algorithm

5) EMISSIVITY is from Frank Wentz's algorithm of calculating wind affected sea surface emissivity

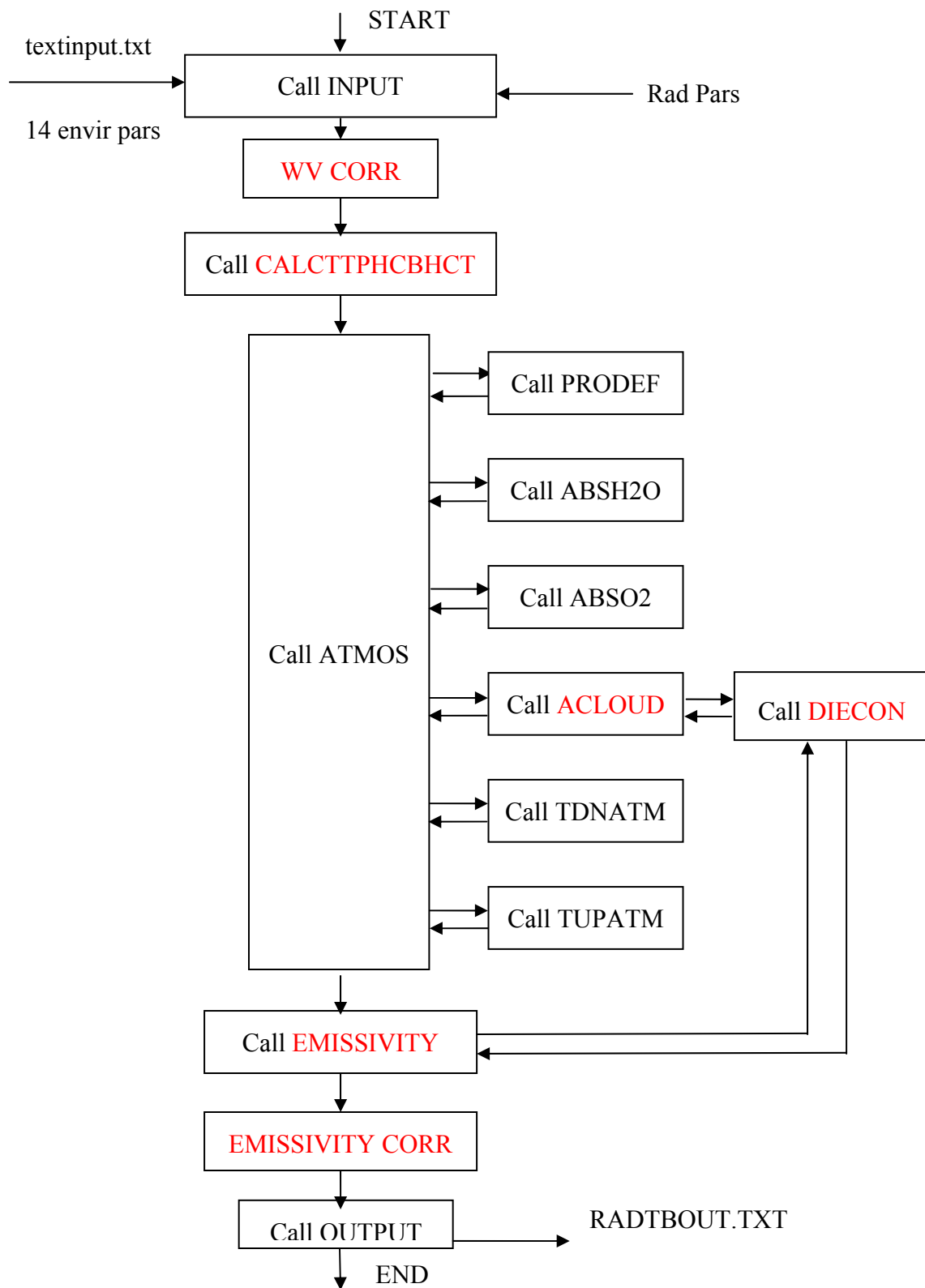6) EMISSIVITY CORR applies 2nd order SST polynomial as a correction to sea surface emissivity

Figure B.1: RTM Fortran Program Block Diagram

APPENDIX C: DELTA-Tb VERSUS SST WITHIN DIFFERENT WS AND WV CATEGORIES

Categories are defined in the order of (WS)(WV)(SST)(CLW), e.g. LLXL means low WS, low WV, arbitrary SST and low CLW
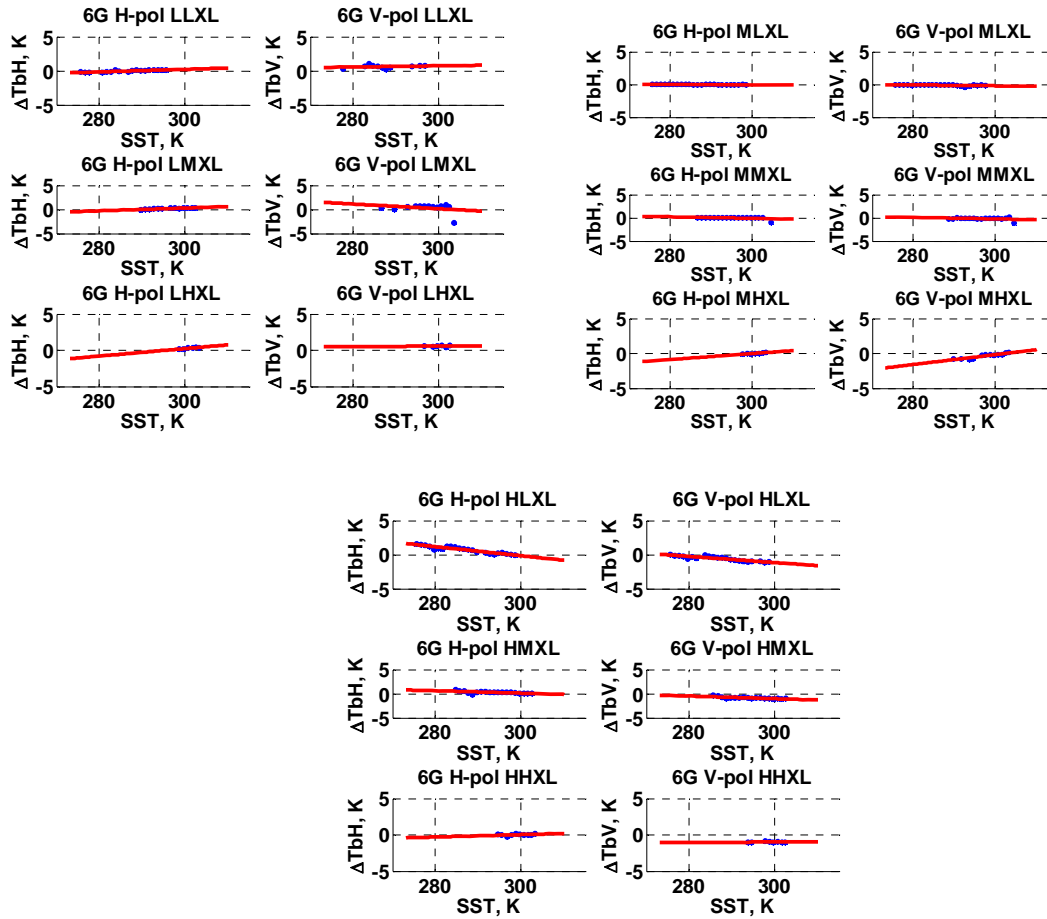

Figure C.1: 6.8 GHz T_b Bias Variations
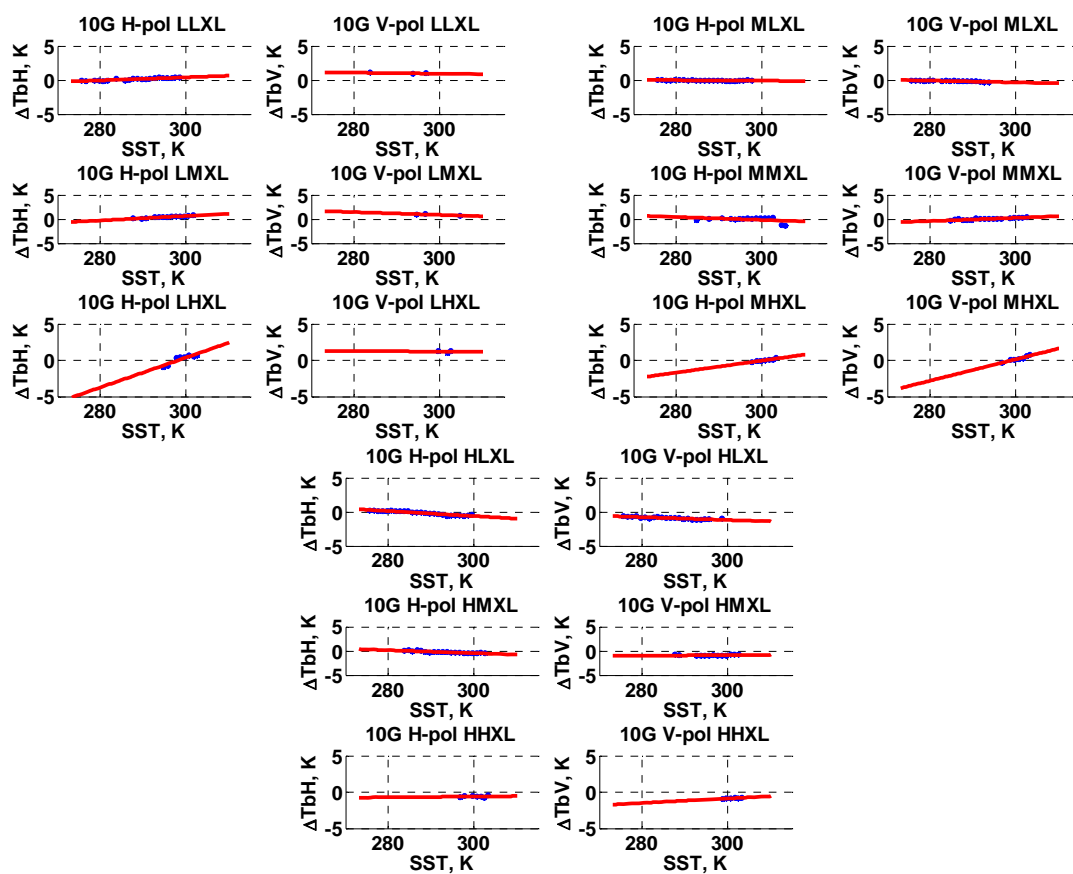
Figure C.2: 10.7 GHz T$_b$ Bias Variations
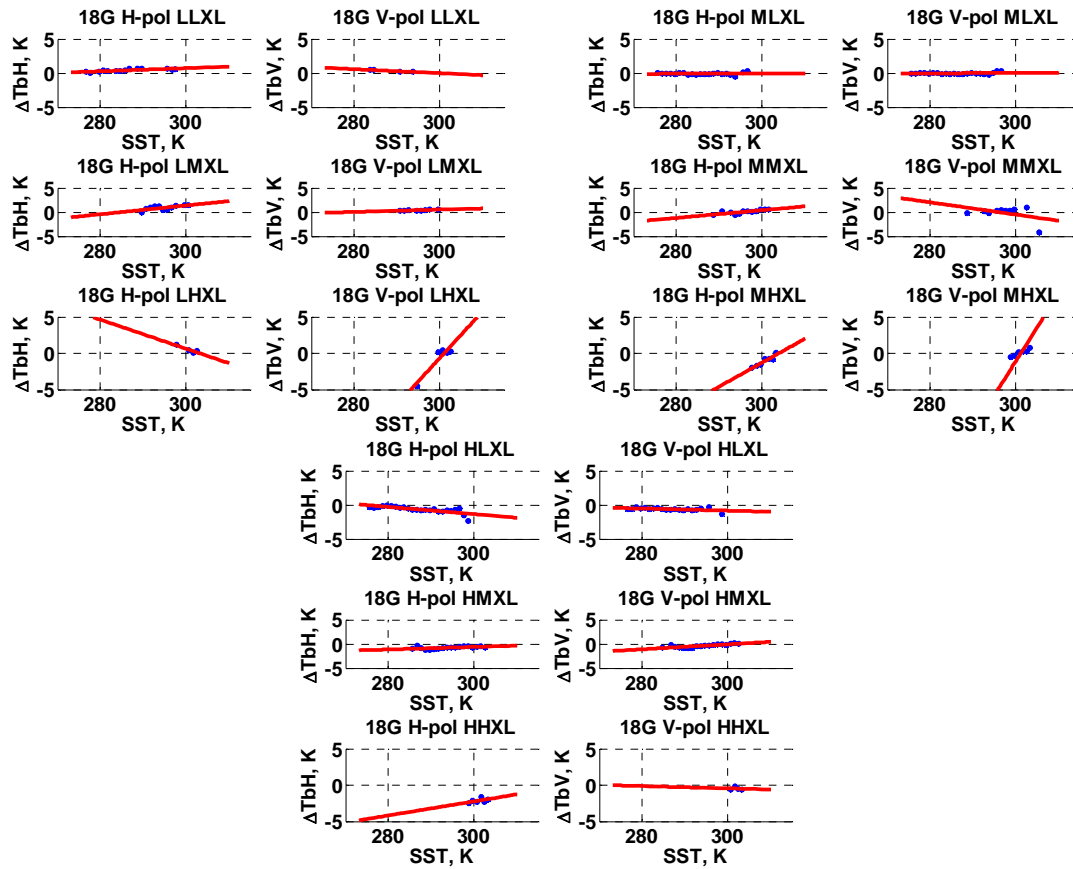
Figure C.3: 18.7 GHz T$_b$ Bias Variations
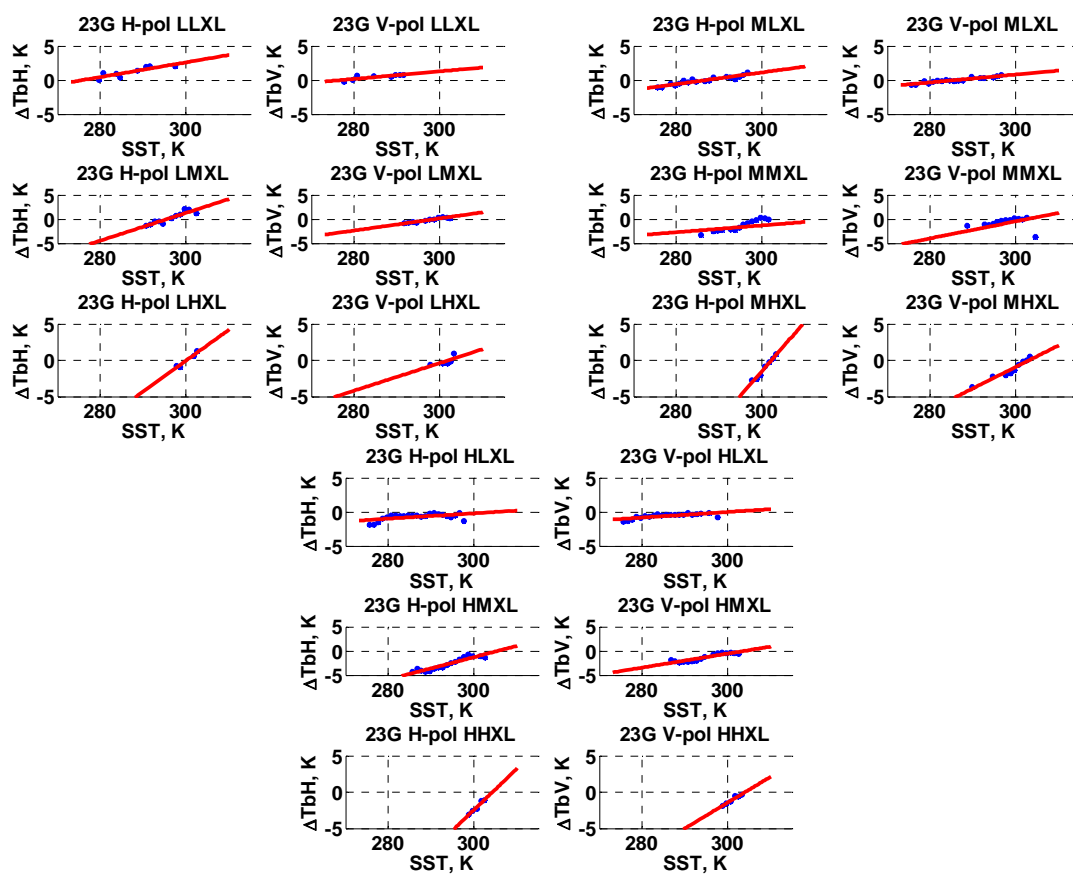
Figure C.4: 23.8 GHz T$_b$ Bias Variations
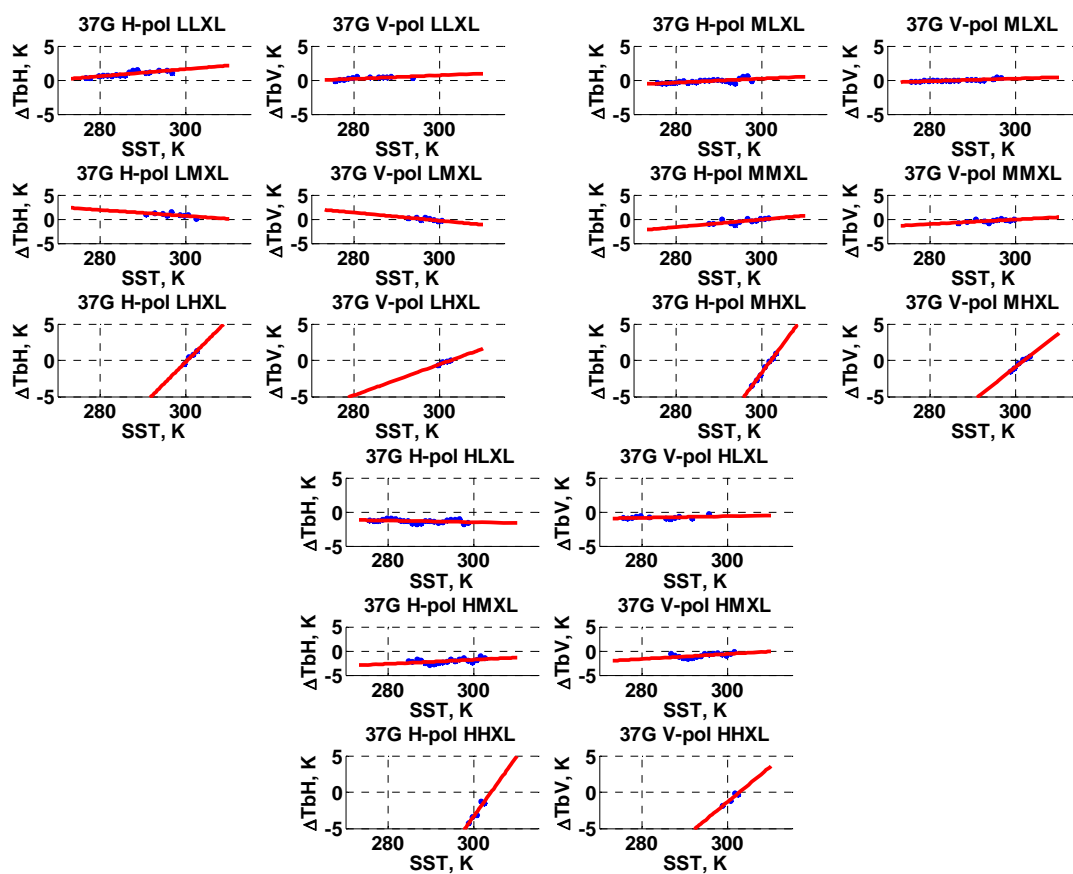
Figure C.5: 37 GHz T_b Bias Variations

APPENDIX D: DELTA-Tb VERSUS SST WITHIN DIFFERENT WV CATEGORIES

Other geophysical conditions are, WS <= 8m/s, CLW <=0.1mm. Categories are defined in the order of (WS)(WV)(SST)(CLW), e.g. LM_LXL means low and medium WS, low WV, arbitrary SST and low CLW.


Figure D.1: 6.8 GHz ΔT_b vs. SST

Figure D.2: 10.7 GHz ΔT_b vs. SST

Figure D.3: 18.7 GHz ΔT_b vs. SST

Figure D.4: 23.8 GHz ΔT_b vs. SST

Figure D.5: 37 GHz ΔT_b vs. SST

APPENDIX E: GAUSSIAN FIT

Gaussian distribution is very commonly seen in random processes. The expected value and standard deviation of a Gaussian distribution are essential in statistical analysis. Most of the random noises or errors in our research are Gaussian. So it is useful and important to find the least-square fit of the Gaussian to the data.

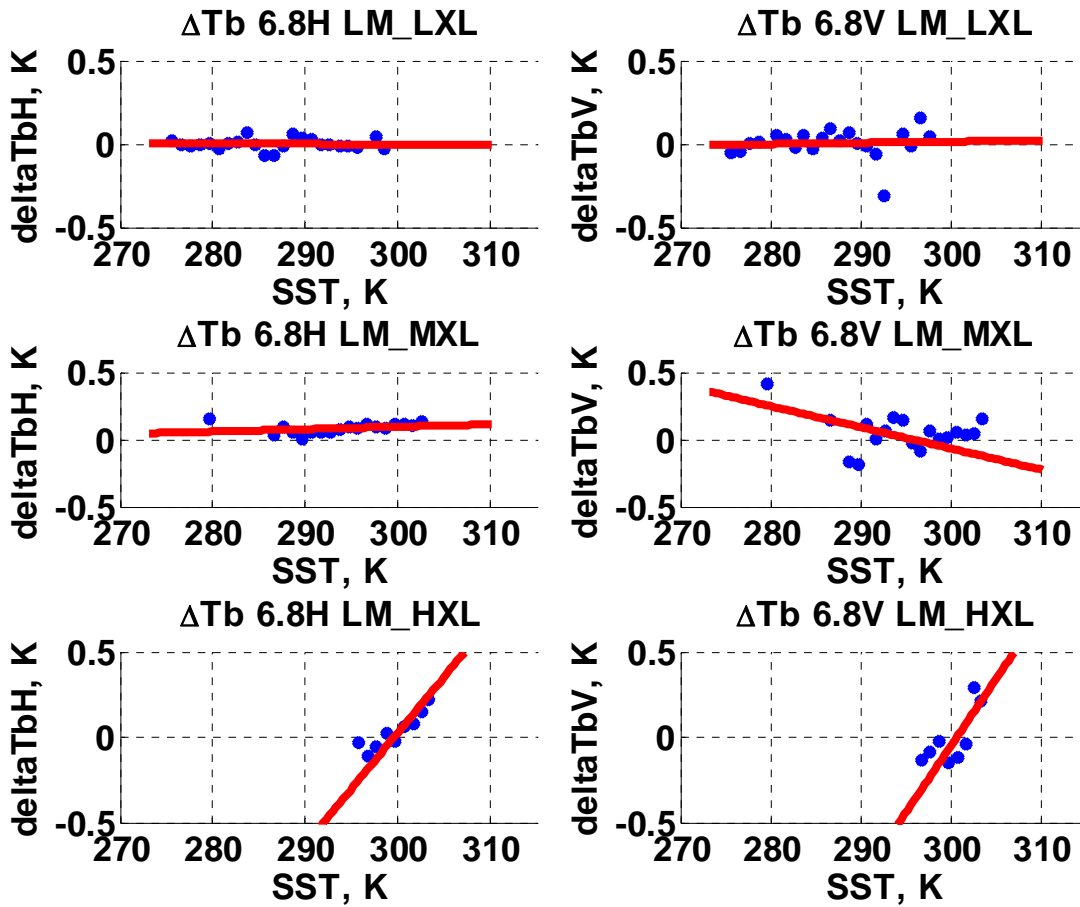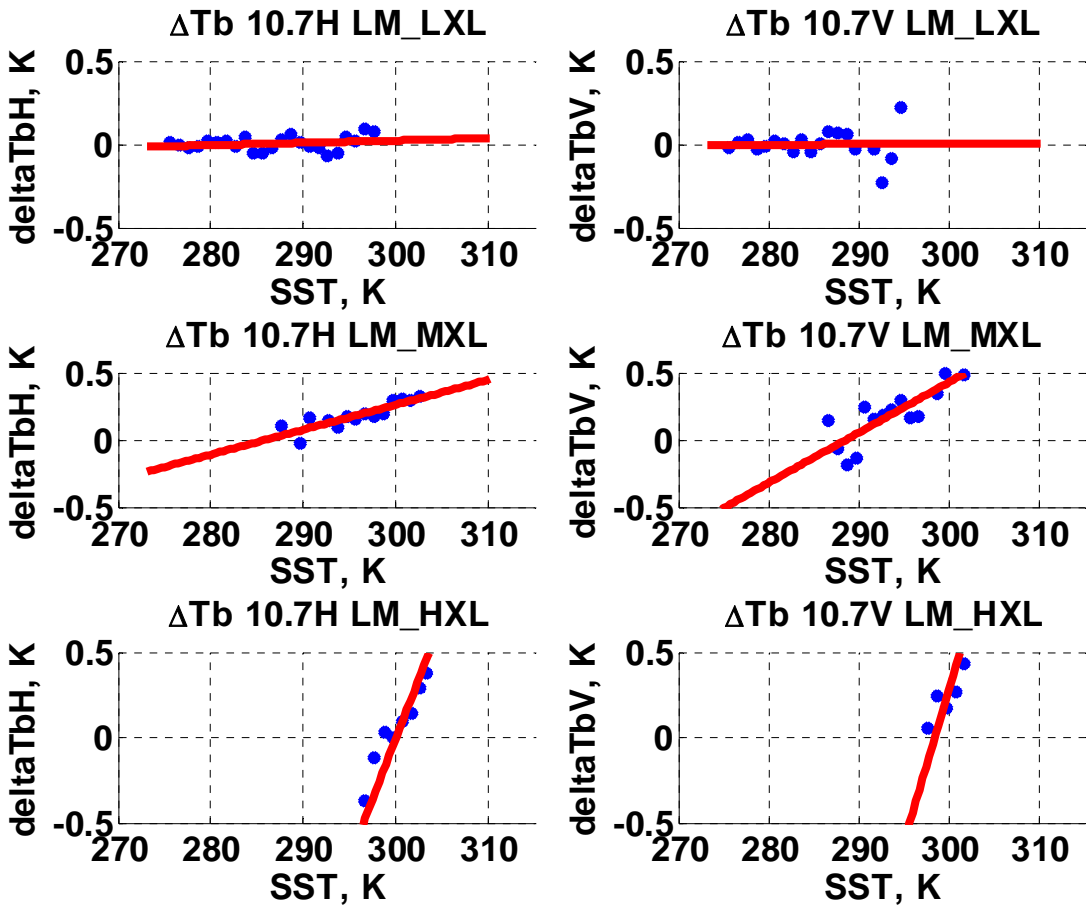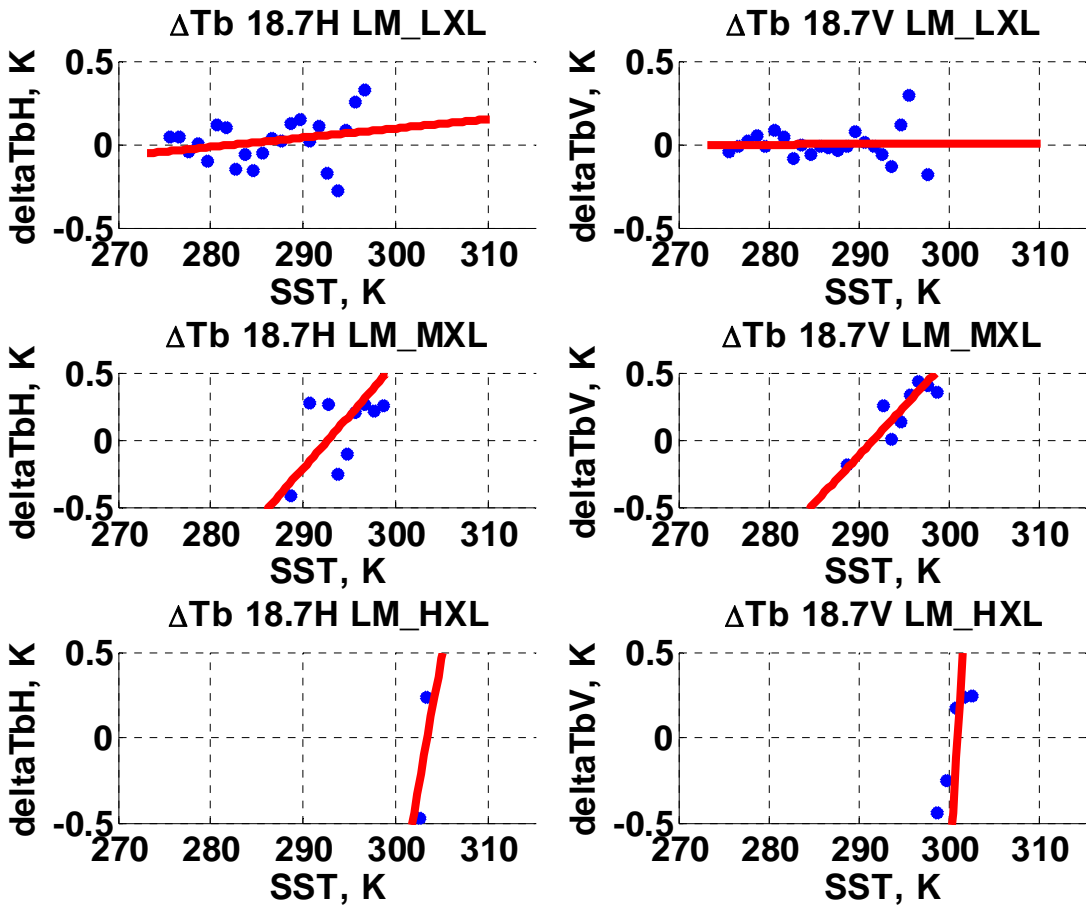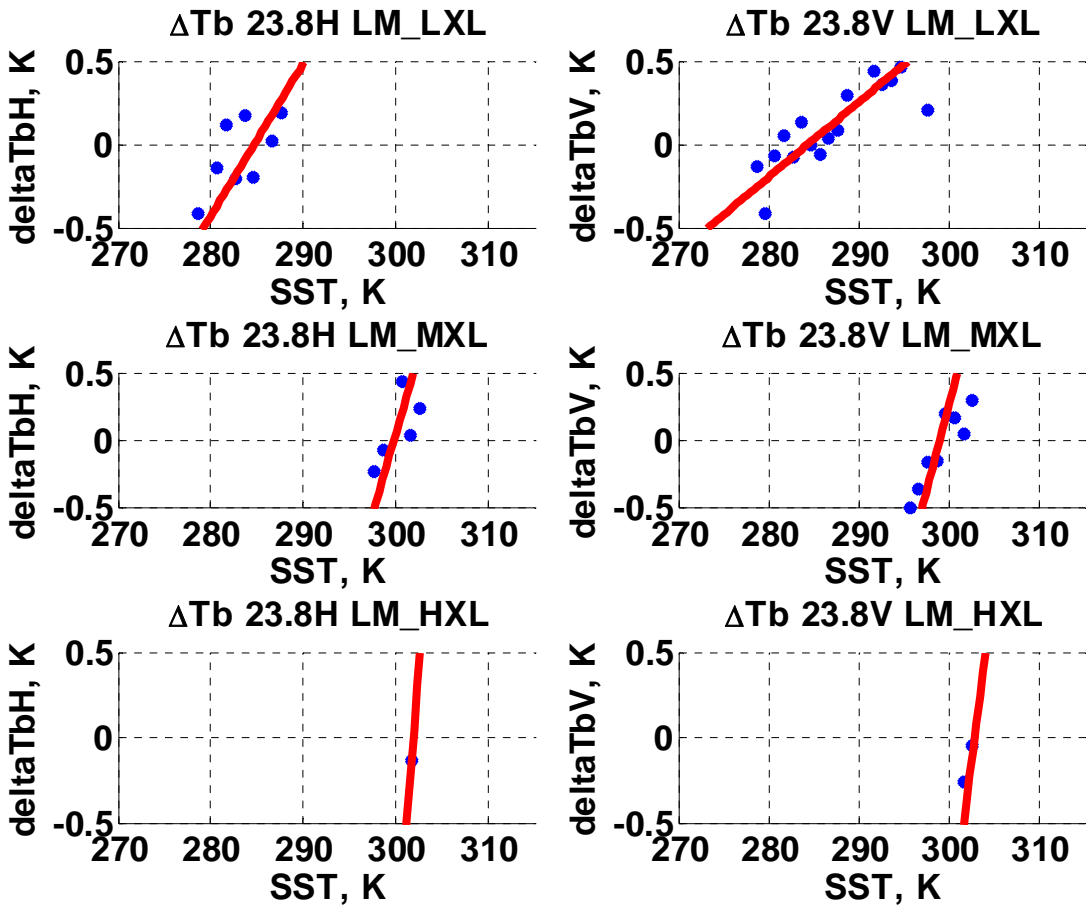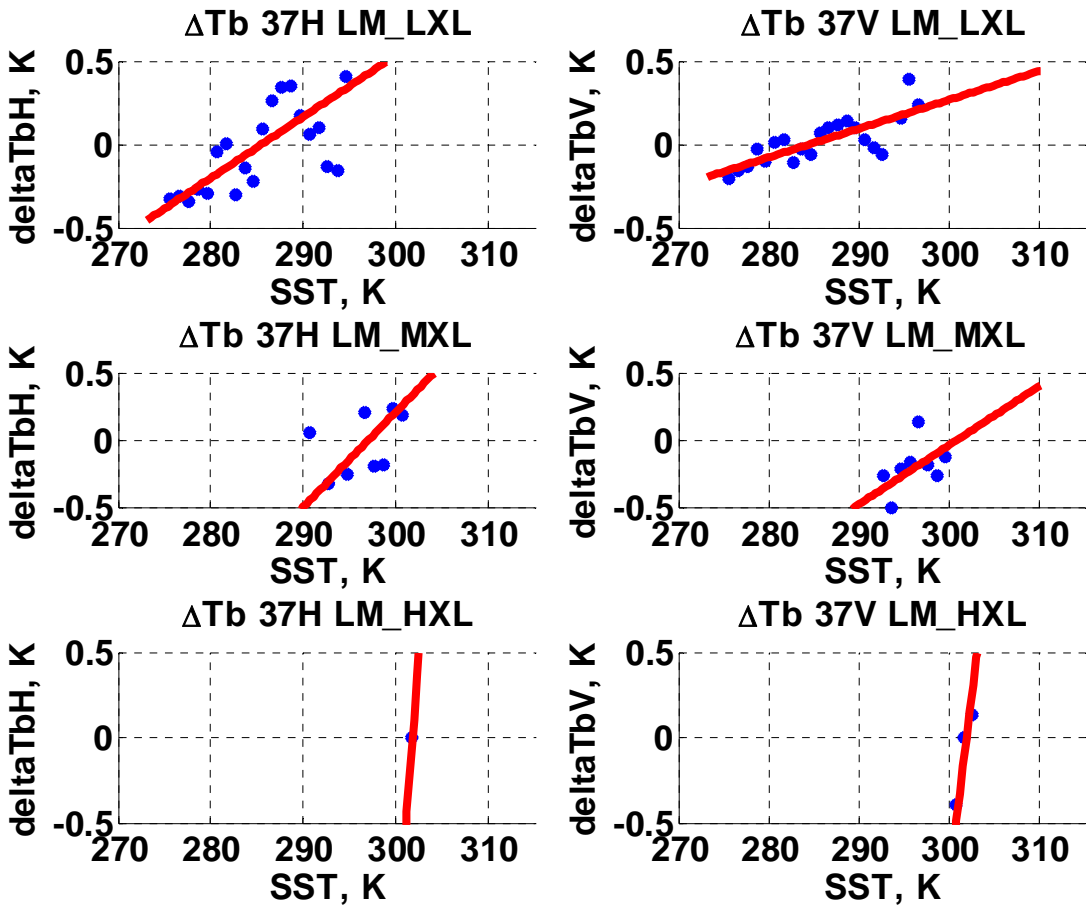The first step is to create histogram from the random data. The shape and number of sampling points in the histogram affects the final Gaussian fit to it. The histogram depends on bin size or number of bins when taking the statistics from the data. Previous researches recommend the equation below to decide the width of the histogram bin (W) [41, 42]

$$W = 2(IQR)N^{-1/3},$$
(E.1)

where W is the width of the histogram bin, is the standard deviation of the distribution and N is the number of available samples. IQR is the interquartile range (the 75th percentile minus the 25th percentile).

Figure E.1 shows fluctuations of Gaussian fit expectations with number of bins in creating data histogram. If the number of bins is too small, the histogram is too coarse to represent details of real distribution of the random data. If the number of bins is too large, there will be gaps in histogram bins which make Gaussian fit unstable. The objective of setting proper number of bins is to let retrieve Gaussian expectation fall in the flat range as shown in Figure E.1.

Number of bins generated by applying equation E.1 to the random data doesn't always guarantee stable expectation from the Gaussian fit. So, an adjustment coefficient C is applied in a new form to calculate the width of the histogram bin

$$W = C \times 2(IQR)N^{-1/3}$$
(E.2)

C is set to be 1/30 for fitting data with a size of larger than a thousand cases. This equation works well with finding Gaussian fits for large data sets. When the size of random

dataset is smaller than one thousand, C is chosen to be a value of 1/10 to 1. It depends on how the gaps in histograms are eliminated by changing the value of C.

By applying proper bin size to the histogram of the random data to analyze, least square error Gaussian fit can be applied to retrieve expectation and standard deviation of the data without being biased by outliers.
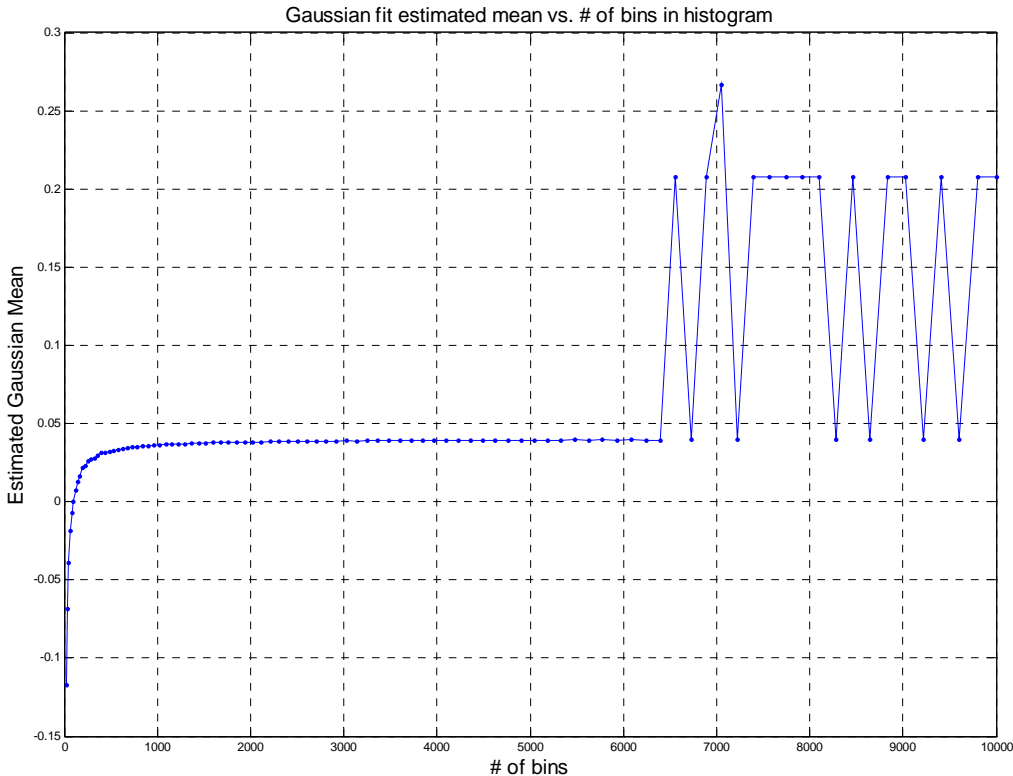

Figure E.1: Fluctuations of Gaussian Fit Expectations with Histogram Bin #

LIST OF REFERENCES

[1] Goody, R., J. Anderson, T. Karl, R.B. Miller, G. North, J. Simpson, G.Stephens and W. Washington, "Why monitor the climate?", *Bulletin Amer. Meteorological Society*, 83, pp. 873-878, 2002

[2] Fawwaz T. Ulaby, Richard K. Moore and Adrian K. Fung, "Microwave Remote Sensing: Active and Passive, Vol 1", Artech House Inc, 1981

[3] Wentz, F.J.; Ashcroft, P.; Gentemann, C, "Post-launch calibration of the TRMM microwave imager", *Geoscience and Remote Sensing, IEEE Transactions on*, Volume 39, Issue 2 , Page(s): 415 - 422, Feb 2001

[4] Imaoka, K.; Sezai, T.; Takeshima, T.; Kawanishi, T.; Shibata, A., "Instrument characteristics and calibration of AMSR and AMSR-E", *Proceedings, IEEE International Geoscience and Remote Sensing Symposium (IGARSS 2002)*, Toronto, Canada, June 24-28, 2002

[5] K. Imaoka, Y. Fujimoto, M. Kachi, T. Takeshima, T. Igarashi, T. Kawanishi, and A. Shibata, "Status of calibration and data evaluation of AMSR on board ADEOS-II", *Proceedings of the SPIE Int. Symp. Remote Sensing Europe*, Barcelona, Spain, Sep. 8, 2003

[6] Y. Fujimoto, "Calibration status of the AMSR and AMSR-E", presented at the *Joint AMSR/AMSR-E Science Team Meeting*, Monterey, CA, Oct. 21–21, 2003

[7] Elizabeth M. Twarog, Willian E. Purdy, Peter W. Gaiser, Kwok H. Cheung and Bernard E Kelm, "WindSat On-orbit Warm Load Calibration", *IEEE Trans. GeoSci. Remote Sensing*, vol. 44, N0. 3, Page(s): 476-495, Mar 2006

[8] Liang Hong, Linwood Jones, and Thomas Wilheit, "Inter-Satellite Microwave Radiometer Calibration Between AMSR and TMI", *Proc IEEE Internat. GeoSci Remote Sensing Sympos. (IGARSS 2006)*, Denver, CO, Jul. 3 – Aug. 4, 2006

[9] Liang Hong, W. Linwood Jones, Thomas T. Wilheit, "Inter-Satellite Radiometer Calibration Between WindSat, TMI and AMSR", *Proc IEEE Internat. GeoSci Remote Sensing Sympos. (IGARSS 2007)*, Barcelona, Spain, July 23-27, 2007

[10] C. Ruf, S. Keihm, B. Subramanya, and M. Janssen, "TOPEX/PSEIDON microwave radiometer performance and in-flight calibration", *Journal of Geophysical Research*, Volume 99, No. 24, Page(s) 915-24–926, 1994.

[11]   Nieke, J.; Aoki, T.; Tanikawa, T.; Motoyoshi, H.; Hori, M., "A satellite cross-calibration experiment", *IEEE GeoSci Remote Sensing Letters,* vol. 1, Issue 3, pp. 215 - 219, Jul 2004

[12]   Ruf, C.S., "Detection of Calibration Drifts in Spaceborne Microwave Radiometers Using a Vicarious Cold Reference", *Geoscience and Remote Sensing, IEEE Transactions on*, Volume 38, Issue 1, Page(s):44 - 52, Jan 2000

[13]   Pui-King Chan; Bo-Cai Gao, "A comparison of MODIS, NCEP, and TMI sea surface temperature datasets", *IEEE GeoSci Remote Sensing Letters,* vol. 2, Issue 3, pp. 270-274, Jul. 2005

[14]   Colton, M. C., and G. A. Poe, "Intersensor calibration of DMSP SSM/I's: F8 to F-14, 1987-1997", *IEEE Trans. GeoSci. Remote Sensing*, vol. 37, pp. 418-439, 1999

[15]   T. T. Wilheit, Jr., J.R. Greaves, J.A. Gatlin, D. Han, B.M. Krupp,A.S. Milman and E.S. Chang, "Retrieval of ocean surface parameters from the scanning multifrequency microwave radiometer (SMMR) on the Nimbus-7 satellite", Geoscience and Remote Sensing, IEEE Transactions on, Volume GE-22, No. 2, Page(s): 133-143, 1984

[16]   WindSat release notes, windsat_release_notes_1_9_0.pdf, 2006

[17]   Thomas T. Wilheit, IPO contract rpt#4, 2005

[18]   Wisler, M. M. and J. P. Hollinger, "Estimation of Marine Environmental Parameters using Microwave Radiometric Remote Sensing Systems", NRL Memo Rpt 3661, Nov., Naval Research Laboratory, Wash DC, 1977

[19]   Debye, P., *Polar Molecules.* Dover, New York, 1929

[20]   Klein, L. A., & Swift C. T., "An Improved Model for the Dielectric Constant of Sea Water at Microwave Frequencies", *IEEE Trans. Antennas Propag.*, AP-25, pp.104-111, 1977

[21]   Salem Fawwaz El-Nimri, "An improved microwave radiative transfer model for ocean emissivity at hurricane force surface wind speed", Master's Thesis, University of Central Florida, 2006

[22]   L. Eymard, S. English, P. Sobieski, D. Lemaire, and E. Obligis, "Ocean surface emissivity modeling", C. Mätzler—UE COST and Univ. Bern, Brussels, Belgium, COST Action 712, 2000

[23]   W. J. Ellison, S. J. English, L. Lamkaouchi, A. Balana, E. Obligis, G. Deblonde, T. J. Hewison, P. Bauer, G. Kelly, and L. Eymard, "A comparison of ocean emissivity models using the advanced microwave sounding unit, the special sensor microwave imager, the

TRMM microwave imager, and airborne radiometer observations", *Journal of Geophysical Research*, Volume 108, No. D21, Page(s): 4663–4663, Nov. 2003

[24]   F. Wentz, and, and T. Meissner, "AMSER Ocean Algorithm", Remote Sensing Systems, Santa Rosa, CA, November 2, 2000

[25]   P. W. Rosenkranz, "Shape of the 5mm oxygen band in the atmosphere", *IEEE Trans. AP*, vol. AP-23, no. 4, pp. 498–506, July 1975.

[26]   P. W. Rosenkranz, "Absorption of microwaves by atmospheric gases", Chapter 2 in *Remote Sensing by Microwave Radiometry*, M.A. Janssen, ed. John Wiley & Sons, New York. (1993)

[27]   Gross, E. P., "Shape of Collision-Broadened Spectral Lines", *Phys. Rev.*, Vol. 97, pp. 395-403, 1955

[28]   Yan Sun, "Evaluation of a microwave radiative transfer model using satellite radiometer observations", Master's Thesis, University of Central Florida, 2003

[29]   Simonetta D Thompson, "Evaluation of a microwave radiative transfer model for calculating satellite brightness temperature", Master's Thesis, University of Central Florida, 2002

[30]   NCEP Reanalysis data, available on website,
        http://www.cdc.noaa.gov/cdc/data.ncep.reanalysis.html

[31]   Reynolds Sea Surface Temperature, Climate Diagnostics Center data, available on website, http://www.cdc.noaa.gov/cdc/data.reynolds_sst.html

[32]   Connor, L.N.; Chang, P.S.; Jelenak, Z.; Wang, N.-Y.; Mavor, T.P., "WindSat validation datasets: an overview", *Proceedings, IEEE International Geoscience and Remote Sensing Symposium (IGARSS 2004)*, Anchorage, Alaska, USA, September 20-24, 2004

[33]   Laurence N. Connor, "The NOAA/NESDIS/ORA WindSat Calibration/Validation Collocation Database", a NOAA Technical Report, November 29, 2005

[34]   L. Garand, D. S. Turner,M. Larocque, J. Bates, S. Boukabara, P. Brunel, F. Chevalier, G. Deblonde, R. Engelen, M. Hollingshead, D. Jackson, G. Jedlovec, J. Joiner, T. Kleespies, D. S. McKague, L. McMillin, J.-L. Moncet, J. R. Pardo, P. J. Rayer, E. Salathe, R. Saunders, N. A. Scott, P. V. Delst, and H. Woolf, "Radiance and Jacobian intercomparison of radiative transfer models applied to HIRS and AMSU channels", *Journal of Geophysical Research*, Volume 106, Page(s) 24 017–24 031, 2001

[35]   P. W. Gaiser, K. M. St. Germain, E. M. Twarog, G. A. Poe, W. Purdy, D. Richardson, W. Grossman, W. L. Jones, D. Spencer, G. Golba, J. Cleveland, L. Choy, R. M. Bevilacqua, and P. S. Chang, "The WindSat spaceborne polarimetric microwave radiometer: sensor description and early orbit performance", *Geoscience and Remote Sensing, IEEE Transactions on*, Volume 42, No. 11, Page(s): 2347 – 2361, Nov. 2004

[36]   Jones, W. L. Park, J. D. Soisuvarn, S. Hong, L. Gaiser, P. W. StGermain, K. M., "Deep-Space Calibration of the WindSat Radiometer", *Geoscience and Remote Sensing, IEEE Transactions on*, Volume 44, No. 3, Page(s) 476 - 495, Mar. 2006

[37]   Ruf, C.S.，Ying Hu and Brown, S.T., "Calibration of WindSat Polarimetric Channels with a Vicarious Cold Reference", *Geoscience and Remote Sensing, IEEE Transactions on*, Volume 44, Issue 3, Page(s): 470 - 475, March 2006

[38]   Gaiser, P.W.; Twarog, E.M.; Li Li; St Germain, K.M.; Poe, G.A; Purdy, W.; Jelenak, Z.; Chang P.S.; Connor L. , "The WindSat space borne polarimetric microwave radiometer: sensor description and mission overview", *Proc IEEE Internat. GeoSci Remote Sensing Sympos. (IGARSS2004)*, Anchorage, Alaska, Sept. 20 - 24, 2004

[39]   Description of SSM/I, Available on website,
        http://www.ssmi.com/ssmi/ssmi_description.html

[40]   Kummerow, C., Barnes, W., T. Kozu, J. Shiue, and J. Simpson, "The tropical rainfall measuring mission (TRMM) sensor package", *Journal of Atmospheric and Oceanic Technology*, Volume 15, Issue 3, Page(s): 809 - 817, June 1998

[41]   Scott, D. "On optimal and data-based histograms", *Biometrika*, Volume 66, No. 3, Page(s) 605 - 610, Dec., 1979

[42]   Izenman, A. J., "Recent developments in nonparametric density estimation", *Journal of the American Statistical Association*, Volume 86, No. 413, Page(s) 205 - 224, Mar., 1991